

https://dspace.org/

A carbon fibre wheel for a lightweight production sports car

Czypionka, Stefan Nikolaus

2019

https://hdl.handle.net/10539/30387

Czypionka, Stefan Nikolaus (2019) A carbon fibre wheel for a lightweight production sports, University of the Witwatersrand, Johannesburg, <http://hdl.handle.net/10539/30387>

Downloaded from a DSpace repository. https://dspace.org/

A CARBON FIBRE WHEEL FOR A LIGHTWEIGHT PRODUCTION SPORTS CAR

Stefan Nikolaus Czypionka

A dissertation submitted to the Faculty of Engineering and the Built Environment, of the University of the Witwatersrand, in fulfilment of the requirements for the degree of Master of Science in Engineering.

Johannesburg 2019

DECLARATION

I declare that this dissertation is my own unaided work. It is being submitted to the Degree of Master of Science to the University of the Witwatersrand, Johannesburg. It has not been submitted before for any degree or examination to any other University.

……

(Signature of Candidate)

…….. day of ……., ……

(day) (month) (year)

ABSTRACT

The wheel of a passenger vehicle must be designed to be safe and light. Despite the potential of carbon fibre as an automotive material due to high strength and low weight, the prevalence of carbon fibre reinforced plastics (CFRPs) in vehicle wheels is limited. This study develops a method to design a CFRP wheel for a high-performance roadster. The designed CFRP wheel used as a case study to illustrate the method is offered by an automotive manufacturer as a high-performance option instead of aluminium wheels. Finite element (FE) simulations were performed on the geometry of the wheel. These helped remove problematic geometric profiles prior to the manufacture of a mould. FE simulations were conducted to reduce the mass of the aluminium hubs required for mounting the CFRP wheel to a vehicle. The CFRP wheel mass is 6.4 kg as compared to the original aluminium wheel which weighs 8.1 kg. This initial design passed the dynamic cornering fatigue test (the most stringent strength test for wheels). Thereafter a prototype wheel was instrumented with strain gauges and a bending moment was applied to the hub using a custom-built test rig. The test rig produced a static load equivalent to the dynamic cornering fatigue test (in which the applied bending moment varies sinusoidally). The test rig allowed for the deflection of the load arm to be measured. The comparison of the experimentally measured strains and an FE model which includes the CFRP laminate properties showed good agreement. This study shows that an aluminium wheel for a high-performance roadster can be redesigned using CFRP to be 21 % lighter. A bending stiffness test was conducted on another similar CFRP wheel at elevated temperatures. An 18 % reduction in bending stiffness was calculated when the wheel was heated to 140 ^{o}C, this reduction reduced to 13 % once the wheel cooled to ambient temperature. Further study of the effect of temperature on CFRP wheels is required. This study has illustrated a successful method to design CFRP wheels for passenger vehicles to affect a reduction in mass.

ACKNOWLEDGEMENTS

I would like to acknowledge and thank the following people and institutions:

Professor Frank Kienhöfer, who provided me with key guidance on many aspects of my work over the last two years. I am continually grateful for the drive he has given me to better myself and my work. I am thankful for the funding provided over the last two years by merSETA, which Prof. Kienhöfer was able to arrange.

I would like to thank Blackstone Tek, without whom it would have not been possible to conduct this research. I want to thank all the members of the engineering and factory staff for assisting me in every way they could. It was an amazing opportunity to work with the premier manufacturer of carbon fibre wheels and carbon fibre automotive parts. I would like to especially thank Gary Turner and Terry Annecke for providing me with space to conduct my work and materials for experimentation.

I would like to thank my family for their love and support during the time of my research. I would especially like to thank my girlfriend Irma Helena Burger for believing in me throughout this time, even when I did not believe in myself.

CONTENTS

DECLARATION ii

ABSTRACT iii

ACKNOWLEDGEMENTS iv

CONTENTS v

LIST OF FIGURES viii

LIST OF TABLES x

LIST OF SYMBOLS xi

LIST OF ACRONYMS xiii

1. INTRODUCTION 1

1.1. Background 1

1.2. Literature Review 3

1.2.1. The benefits of lightweight wheels 3

1.2.2. CFRP car wheels 3

1.2.3. Wheel testing 4

1.2.4. Thermal effects 5

1.3. Objectives 9

1.4. Published work 9

2. ISOTROPIC MODELLING OF THE WHEEL 11

2.1. Isotropic Finite Element Model 11

2.1.1. Modelling geometry 11

2.1.2. Idealisation 13

2.1.3. Meshing 14

2.1.4. Test setup 16

2.1.5. Solution and mesh independence 16

2.1.6. Improvements made to the wheel 17

2.2. Aluminium Hub Simulation 19

2.2.1. Modelling geometry idealisation 21

2.2.2. Contacts and meshing 23
2.2.3. Test setup 24
2.2.4. Result of the isotropic hub analysis 24
2.3. Summary 29
3. EXPERIMENTAL TESTING OF THE CFRP WHEEL 31
3.1. Bending Moment Test Rig 31
3.2. Instrumentation 32
3.3. Methodology 34
3.3.1. Experimental procedure 34
3.3.2. Data processing 35
3.4. Results of the Bending Stiffness Test 36
3.4.1. Bending stiffness of the wheel 37
3.5. Cornering Fatigue Test 40
3.6. Material Properties of the Carbon Fibre Fabrics 41
3.6.1. Material samples 42
3.6.2. Apparatus and methodology 43
3.6.3. Data processing 45
3.6.4. Fibre volume fractions 45
3.6.5. Result of the material testing 46
3.7. Summary 50
4. NUMERICAL MODEL OF THE CARBON LAMINATE 52
4.1. Development of the Laminate 52
4.2. Composite Finite Element Model 53
4.2.1. Modelling process 53
4.2.2. Surface meshing and surface naming 55
4.2.3. Laminate generation 56
4.2.4. Test setup 59
4.3. Comparison to the Physical Wheel 60

4.4. Stress Analysis of the Wheel 63
4.5. Summary 66
5. THERMAL TESTING OF THE CFRP WHEEL 68
5.1. Wheel Specimen 68
5.2. Test Equipment 69
5.3. Test Procedure 69
5.4. Results and Discussion of the Thermal Testing 71
5.4.1. Heat transfer to the wheel and temperatures 71
5.4.2. Bending stiffness versus load 73
5.4.3. Bending stiffness versus temperature 74
5.5. Summary 76
6. CONCLUSIONS AND RECOMMENDATIONS 78
7. REFERENCES 83
APPENDIX A: FE VALIDATION USING FIRST PRINCIPLES 87
Geometry and Free Body Diagram 87
Isotropic Validation 87
Classic Laminate Theory Validation 88

LIST OF FIGURES

Figure 1-1 (a) Koenigsegg CFRP wheel (L) (b) Carbon Revolution CFRP wheel (R) 1
Figure 1-2 The VUHL 05RR with CFRP racing wheels [18] 2
Figure 1-3 Donkervoort D8 GTO-40 with BST carbon fibre wheels [19] 2
Figure 1-4 Cross section of a dynamic cornering fatigue test rig 5
Figure 1-5 FE model of the dynamic cornering fatigue test [7] 5
Figure 1-6 Temperature development on the surface of the rotor during braking from v_0 = 100 km/h [27] 6
Figure 1-7 Brake rotor bulk temperature under a 200km/h brake fade test [29] 7
Figure 1-8 Temperature at 3 radial locations of a brake rotor on a vehicle travelling at a constant speed of 80 km/h [29].....7
Figure 2-1 Representative geometry of a wheel profile 12
Figure 2-2 CAD geometry of the tested wheel.....13
Figure 2-3 Wheel geometry used for the isotropic simulation of the CFRP wheel. Original body (left), Virtual Topology (right).....13
Figure 2-4 Mesh used in ANSYS mechanical for the isotropic approximation.....15
Figure 2-5 Equivalent stress on the initial isotropic FE model 17
Figure 2-6 Equivalent stress in the modified isotropic model.....18
Figure 2-7 Inner hub used on the first prototype wheel 20
Figure 2-8 Cross-section of the initial hub assembly 21
Figure 2-9 Initial prototype wheel with 3-part aluminium hubs.....21
Figure 2-10 Geometry used for validation of new hub geometry 22
Figure 2-11 Mesh used to develop the improved hubs.....23
Figure 2-12 Stress distribution on the prototype inner hub.....25
Figure 2-13 Front view of the inner hub. Prototype (Left) Production (Right).....26
Figure 2-14 Cross-section of the production hub assembly.....26
Figure 2-15 Stress distribution on the inner hub of the production wheel 27
Figure 2-16 Fatigue curve of the improved wheel hub design 28
Figure 2-17 Production wheel with 2-part aluminium hubs.....29
Figure 2-18 Illustration of the development of the improved methodology 30
Figure 3-1 Cross-sectional schematic of the test apparatus used 32
Figure 3-2 Placement of strain gauges on the experimental prototype.....33
Figure 3-3 Photograph of the applied strain gauges.....34

Figure 3-4 Deflection of the load arm for test 1 and test 2 38
Figure 3-5 Measured strains on the surface of the wheel 39
Figure 3-6 Measured strains of experiment 1 and 2.....40
Figure 3-7 Shimadzu tensile testing machine used at the University of the Witwatersrand ...44
Figure 3-8 Laser extensometer used for material testing.....44
Figure 3-9 Tensile testing results of the woven material.....47
Figure 3-10 Tensile Testing results of the UD material at 0 degrees.....48
Figure 3-11 Tensile testing results of the UD material at 90 degrees 49
Figure 3-12 Cross-sectional illustration of UD fibres subject to external pressure during the manufacturing process 50
Figure 4-1 Surface model of the experimental prototype wheel 54
Figure 4-2 ANSYS workbench environment for composite modelling 55
Figure 4-3 Mesh used in the composite model.....55
Figure 4-4 Example of a ply area to define the layup of a spoke ply.....56
Figure 4-5 Rosette used for definition of fibre reference direction 58
Figure 4-6 (a) Fibre reference direction of a ply before draping; (b) fibre reference direction after draping.....58
Figure 4-7 Angled gauge used for the strain probe in the composite FE model.....60
Figure 4-8 Measured strains on the spokes compared to the FE results 61
Figure 4-9 Comparison of the simulated deflection to the deflection of the edge of the rim ..62
Figure 4-10 Locations probed for maximum stresses during post processing.....64
Figure 4-11 Cross-section of a spoke of the prototype wheel 64
Figure 5-1 CAD model of the wheel used for thermal testing 68
Figure 5-2 Thermocouple placement on the wheel 70
Figure 5-3 Illustration of a bending stiffness test 71
Figure 5-4 Heat transfer methods from a brake assembly to the wheel: (A) conduction, (B) convection and (C) radiation 72
Figure 5-5 Bending stiffness of the wheel at ambient temperature and 140°C 74
Figure 5-6 Average bending stiffness of the experimental prototype with increasing temperature.....75
Figure 6-1 Donkervoort D8 GTO-40 with CFRP wheels developed in this study [19].....78
Figure A-0-1 Free body diagram of the plate used for validation 87

LIST OF TABLES

Table 2-1 Dimensions of the modelled wheel....12
Table 2-2 Simulation values of the initial isotropic simulation....15
Table 2-3 Maximum stress on each face between spokes at discrete load directions....19
Table 2-4 Material properties of Aluminium 6082 and 7075....22
Table 3-1 Technical specifications of the strain gauges....33
Table 3-2 Instrumentation used on the experimental prototype....33
Table 3-3 Measured displacement of the edge of the wheel rim....38
Table 3-4 Dimensions of the test specimens....43
Table 3-5 Fibre Volume Fractions of the specimens....46
Table 4-1 Post-processed stresses on the wheel (as percentage of static stress limit)....63
Table 5-1 List of equipment used for thermal testing....69
Table 5-2 Surface temperatures recorded during testing....72
Table 5-3 Load arm displacement (mm)....73
Table 5-4 Bending stiffness of the wheel during experimentation in terms of the maximum calculated value (% of maximum)....74
Table A-0-1 Response of the plate under axial loading....88
Table A-0-2 Response of the plate under the lateral load....88
Table A-0-3 Material properties obtained from the ANSYS material database....88
Table A-0-4 Comparison of forces required for solid and surface models....90

LIST OF SYMBOLS

d	dial gauge deflection [mm]
D_B	effective bolt diameter [m]
e	offset [m]
E_X	Young's Modulus along the x-axis [GPa]
E_Y	Young's Modulus along the y-axis [GPa]
E_Z	Young's Modulus along the z-axis [GPa]
F_a	axial force [N]
F_b	bending force [N]
F_F	fibre volume fraction
F_p	pre-load force [N]
F_R	maximum static wheel load [N]
F_R	resin volume fraction
GF	gauge factor
G_{XY}	shear modulus on the xy plane [GPa]
G_{xz}	shear modulus on the xz plane [GPa]
G_{YZ}	shear modulus on the yz plane [GPa]
I	second moment of area [m^4]
I_R	rotational inertia [$kg.m^2$]
K	material constant
k_b	bending stiffness [N.m/ ^{o}]
L	length [mm]
m	mass [kg]
M_B	bending load [N.m]
M_{Bmax}	reference bending load [N.m]
m_e	effective mass [kg]
m_e	equivalent mass [kg]
Q_{ij}	reduced stiffness matrix
R	gauge resistance [Ω]
r_{dyn}	dynamic tyre radius [m]
S_e	endurance strength [MPa]
t	thickness [mm]
T_G	glass transition temperature [^{o}C]

T_w lug nut torque [N.m]

v_0 initial velocity [km/h]

v_b beam deflection [mm]

v_{tot} total volume [m^3]

v_{xy} Poisson's ratio on the xy plane

v_{xz} Poisson's ratio on the xz plane

v_{yz} Poisson's ratio on the yz plane

w width [mm]

$\underline{\Delta}$GF uncertainty of the gauge factor

ΔL change in length [mm]

ΔR change in resistance [Ω]

$\underline{\Delta}$R uncertainty of the change in resistance [Ω]

Δε uncertainty of the measured strain

ε measured strain [mm/mm]

θ angular deflection [deg]

μ coefficient of friction

ρ_F fibre density [kg/m^3]

ρ_R resin density [kg/m^3]

σ_a alternating stress [MPa]

σ_A axial stress [MPa]

σ_E endurance strength [MPa]

σ_m mean stress [MPa]

σ_{min} minimum stress [MPa]

σ_R range of stress [MPa]

σ_{UT} ultimate tensile strength [MPa]

σ_{YC} compressive yield strength [MPa]

σ_{YT} tensile yield strength [MPa]

LIST OF ACRONYMS

ACP	ANSYS Composite PrePost
BST	Blackstone Tek
CFRP	Carbon fibre reinforced polymer
CLT	Classic laminate theory
CT	Computed Tomography
DCF	Dynamic cornering fatigue
ETRTO	European Tyre and Rim Technical Organisation
FE	Finite element
GVM	*Gross vehicle mass*
OE	Original equipment
OSS	Oriented selection set
UD	Unidirectional material

1. INTRODUCTION

1.1. Background

The wheel is arguably one of the most fundamental components of a road going-vehicle. It is responsible for the transmission of power from the drive components of the vehicle to the road, while also enabling the vehicle to make directional changes. Both the wheel mass and rotational inertia affect the vehicle's performance and efficiency. This has led to substantial development efforts to reduce the wheel weight and rotational inertia while simultaneously maintaining or increasing the material strength [1]. The need for newly produced vehicles to meet stricter emissions standards is driving the development of lightweight wheels [2–6].

Numerous research studies have been published on the development of steel [7–9] and aluminium [10–15] wheels. Despite the tremendous potential of carbon fibre as an automotive material due to high strength, low weight and superior fatigue properties, the prevalence of carbon fibre reinforced polymers (CFRP) on road vehicles is limited. There is a lack of published research on the use of CFRP in automotive wheels. Giger and Ermanni [16] demonstrated the development process of a CFRP motorcycle rim. This wheel was, however, not tested to certified standards. Rondina et al. [17] investigated a high volume production method for carbon fibre wheels. The paper simulated the production process; however, no certified wheel appears to have been produced.

Figure 1-1 shows two of the currently commercially available CFRP wheels available on the road. Figure 1-1(a) shows a CFRP wheel made by Koenigsegg, while Figure 1-1(b) shows the wheel made by an Australian company Carbon Revolution, which is provided as an aftermarket component and original equipment (OE) for the Ford Shelby GT350R. While these CFRP wheels are available on the market, there is no published research on these, primarily due to the proprietary techniques employed.



Figure 1-1 (a) Koenigsegg CFRP wheel (L) (b) Carbon Revolution CFRP wheel (R)

This work was conducted in collaboration with Blackstone Tek (BST). Blackstone Tek is a South African company based in Johannesburg, South Africa [18]. BST primarily manufactures wheels for motorcycles and exports worldwide. In recent years, BST has developed a CFRP road and racing wheel for a lightweight Mexican supercar, the VUHL 05RR (See Figure 1-2). This wheel was the first CFRP car wheel produced by BST. Challenges exist in producing a wheel tested to certified standards on a larger scale. Of primary concern for the development of a composite wheel for automotive applications is the generation and dissipation of heat from brake discs. In vehicles with tight component spacing and only partial aeration of the wheel wells, the concentration of heat and possible detrimental effects on the composite must be investigated.



Figure 1-2 The VUHL 05RR with CFRP racing wheels [18]

For this study, a method of developing a CFRP wheel was determined using the design of a wheel to fit a Donkervoort D8 GTO (40th anniversary edition) [19] as shown in Figure 1-3. The wheel detailed in this study was delivered as OE to the vehicle manufacturer. This study serves as proof of concept for the implementation of CFRP wheels for high performance production cars and provides a guide for the development of future CFRP wheels.



Figure 1-3 Donkervoort D8 GTO-40 with BST carbon fibre wheels [19]

1.2. Literature Review

This section will discuss the importance of reducing weight in rotational components and the physical aspects thereof, the mechanical testing that is conducted on wheels and thermal effects of vehicle components on composite wheels.

1.2.1. The benefits of lightweight wheels

There are two inertial components to a rotating element, such as a wheel: its mass (m) and its rotational inertia (I). Forward vehicle motion requires fuel to be expended to give the wheel translational as well as rotational energy. The wheel thus has an increased effective mass (m_e), where the effective mass is described by the mass of the wheel (m), its rotational inertia (I_R) and the ratio between its rotational speed and linear velocity (n) [20]:

$$m_e = m + I_R n^2$$

The fuel saving benefit of reducing wheel weight is thus amplified when compared to the weight saving of non-rotational components.

In addition to the fuel saving benefit of wheel weight reduction, reducing wheel weight improves vehicle ride comfort. Hrovat [20] determined that minor performance improvements were possible on passive suspensions, while major improvements were seen on vehicles with adaptive suspension systems. The Donkervoort D8 GTO is factory equipped with adaptive suspension, and thus both vehicle handling and ride quality improvements are realised.

1.2.2. CFRP car wheels

Ressa [21] and Walther [22] developed a CFRP wheel for a Formula SAE vehicle. Both studies used a first principles approach to determining the load conditions and did not test to certified standards.

Giger and Ermanni [16] developed a CFRP motorcycle rim using computer simulation. The work highlighted that the number of variables involved with the optimisation of CFRP components is high. An evolutionary algorithm was developed to determine the optimal parameters for the manufacture of the wheel. The variations of prepreg materials with different fibre layouts, the number of fibre plies and the orientation of each ply were optimised [16]. The simulated tests were developed from first principles and considered the forces acting during maximum braking and lateral loading of the wheel. While the work

showed the method that was employed, the optimal parameter set determined was not published.

1.2.3. Wheel testing

To certify the structural integrity of wheels before they are introduced to the market, a number of fatigue tests to simulate strenuous road conditions are carried out [23]. Tests are carried out to simulate three basic driving conditions, radial fatigue for straight driving, cornering fatigue for repeated bending moments and impact testing to simulate curb strikes and potholes. While testing standards have evolved over time to certify new materials such as lightweight steels and aluminium [23], no certified test existed for CFRP wheels. At the start of this study, a testing standard to certify composite wheels existed in draft form. This standard was in development at TÜV in conjunction with major manufacturers of composite wheels. The standard has since been published [24].

To reduce the number of physical prototypes required for testing, finite element (FE) methods are used. Physical testing without the use of FE methods will not provide optimal results [10]. In addition, the complex shapes that are common in styled wheels all but exclude the use of analytical methods [12]. FE simulations have been conducted on wheels under radial loads [12–14], [25], bending loads [7–9], [11], [15] and impact conditions [26].

FE analysis conducted to simulate radial fatigue identified that the load applied to the wheel can be approximated by a cosine function having a central angle of 40^{o} in either direction of the contact point with the road [13]. Models for radial fatigue were completed by modelling the wheel as a single component and were tested according to the procedure outlined in SAE J267. Impact test simulations were conducted [26] in accordance with SAE J175 (13^{o} impact test) and SAE J1981 (radial impact test). The FE model used in the study consisted of separate meshes for the striker mass, the wheel-tyre assembly and the wheel hub fixture.

Several studies have stated that the most strenuous test wheels are subjected to while being certified is the dynamic cornering fatigue (DCF) test [7], [9], [11]. If a wheel passes this fatigue test it has a high likelihood of passing all other strength tests. DCF tests are generally conducted in accordance with the method described in ISO 3006. Figure 1-4 illustrates the rig used by BST to conduct the DCF test. The test is conducted by clamping a wheel to a static rig and subjecting it to a bending moment by means of a rotating eccentric mass mounted at the

end of a loading arm. Figure 1-5 illustrates the FE model of the DCF test used by Wang [7]. The test is simulated by applying a rotating force to the end of the moment arm while the wheel is fixed.

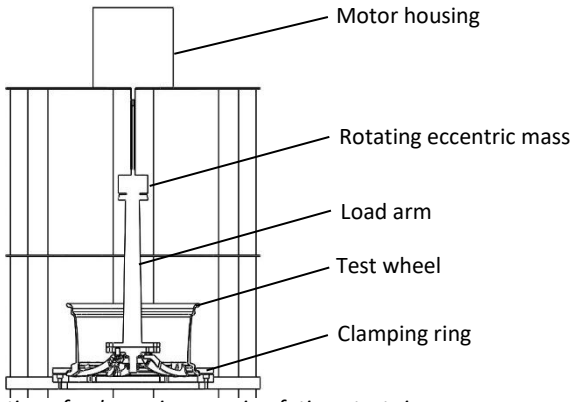


Figure 1-4 Cross section of a dynamic cornering fatigue test rig

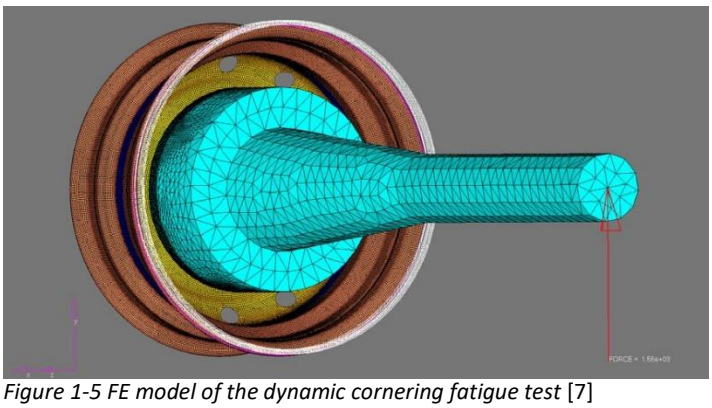


Figure 1-5 FE model of the dynamic cornering fatigue test [7]

1.2.4. Thermal effects

The effect of heat generated during braking is of primary concern for composite wheel development for automotive applications. Heat is generated by friction at the brake pad/disc interface, which resists the rotation of the wheel to slow the vehicle down or bring it to a stop [27]. The thermal behaviour of brake discs has been investigated under various braking modes [27–29]; single emergency braking, alpine braking and high energy driving are the most critical.

Adamowicz and Grzes [27] analysed a single braking event using a transient model of a vehicle braking from a set of initial velocities to a standstill to determine the heat distribution on the rotor of a brake assembly. Figure 1-6 shows the temperature on the surface of the rotor at various radial positions of the brake disc for a vehicle decelerated from an initial velocity of

100 km/h. Simulated emergency braking of the given brake resulted in a maximum temperature on the surface of the rotor in the range of 240–260 °C.

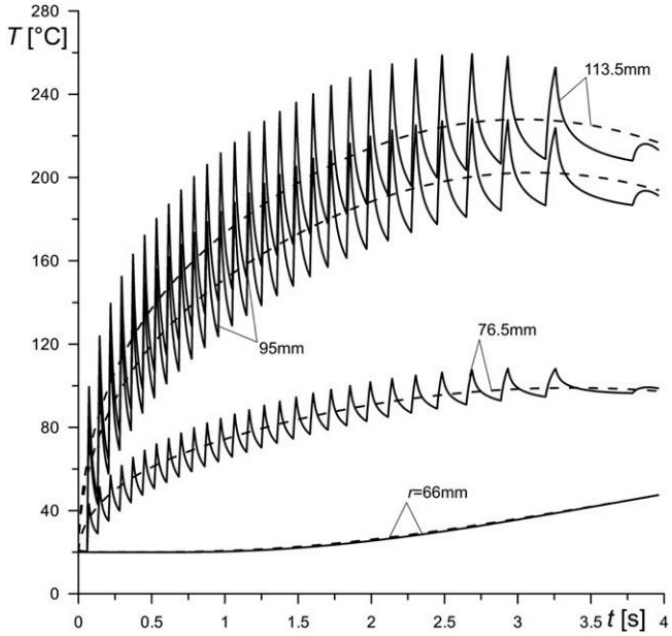


Figure 1-6 Temperature development on the surface of the rotor during braking from v_0 = 100 km/h [27]

Alpine braking is the braking which occurs on a mountain descent, in which a vehicle is either maintained at a constant velocity using continual application of the brakes or repeatedly accelerated and braked by applying and releasing the brakes. Kim et al. [28] investigated both alpine scenarios. This braking mode generated a maximum temperature of approximately 520 °C in the brake disc. The temperature of the brake disc during the descent is shown in Figure 1-7. The temperature of the brake disc progressively rises with each deceleration and remains at elevated temperatures.

The effect of high energy driving on brake systems was characterised by Nisonger et al. [29]. This test simulated a brake disc subjected to racing conditions. The cooling performance was evaluated in a 200 km/h brake fade test, in which a vehicle was accelerated to 200 km/h before being repeatedly decelerated to 50 km/h 25 times. Maximum bulk rotor temperatures in the range of 700 ^{o}C were reported. Figure 1-7 shows the bulk temperature of the rotor recorded in the study. In addition to modelling the build-up of heat in the brake rotor, the study evaluated the cooling effect on a brake rotor of a vehicle traveling at constant speed. Figure 1-8 shows the measured temperatures of the rotor subjected to cooling from an initial temperature of 620 ^{o}C while the vehicle travelled at 80 km/h.

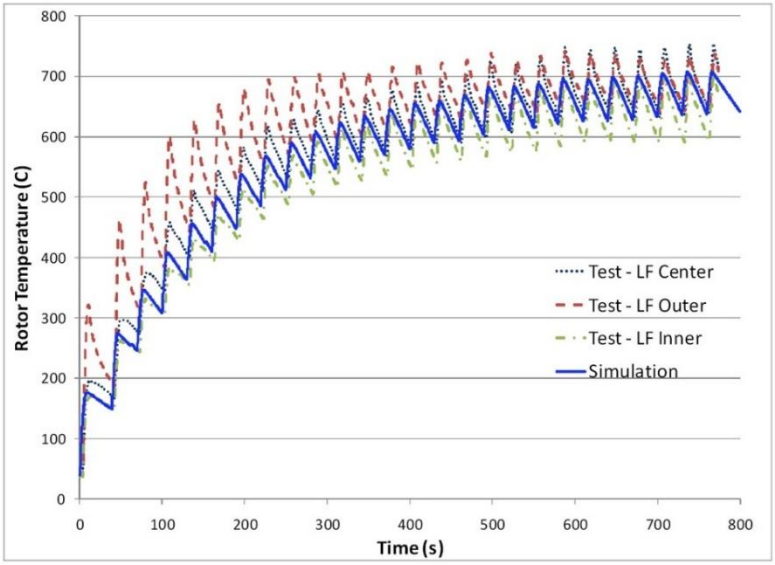


Figure 1-7 Brake rotor bulk temperature under a 200km/h brake fade test [29]

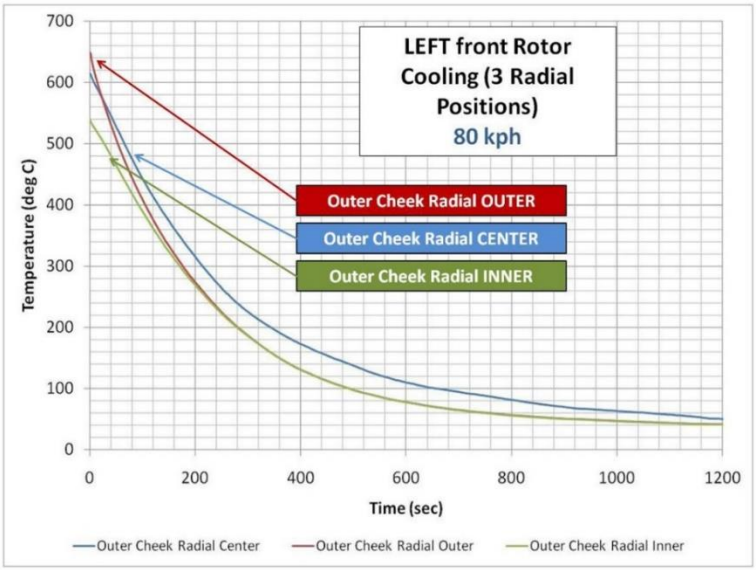


Figure 1-8 Temperature at 3 radial locations of a brake rotor on a vehicle travelling at a constant speed of 80 km/h [29]

Heat exposure is of importance to the structural integrity of carbon fibre composites. Carbon fibres exposed to excessive heat can lead to strength degradation due to oxidation [30,31]. Repeated heating and cooling of a composite leads to residual stresses, which could further degrade the mechanical properties of the composite [32]. Reductions in mechanical properties are caused by delamination and cracks when heated to 340–450 ^{o}C [33].

CFRP has a glass transition temperature (T_G). This is the temperature below which an amorphous polymer has a rigid structure [34]. Above this temperature the polymer is viscous, which is detrimental to the stiffness of the material. There is a lack of research on the detrimental effects of heat in CFRP wheels, as this is a phenomenon that does not adversely affect alloy wheels.

The critical thermal scenario for a carbon composite wheel is the build-up of heat in a brake rotor until a bulk temperature of more than 700 ^{o}C is reached, followed by a rapid deceleration to a standstill to avoid the effects of cooling on the brake rotor. The wheel would then soak up the heat from the brake rotor. Research is required to determine the resulting temperature distribution of a carbon composite wheel in these conditions.

1.3. Objectives

The main objectives of this work were to:

1. Develop a method for the design of a carbon fibre reinforced polymer wheel to withstand dynamic cornering fatigue loads as specified by TÜV following the methodology outlined in ISO 3006 – 2015 for a passenger vehicle.
2. Reduce the mass of a passenger vehicle wheel using a finite element model of a CFRP wheel validated with experimental testing and compare the mass of this wheel to the current aluminium state-of-the-art wheels.
3. Understand the mechanical strength degradation of carbon fibre reinforced plastic wheels with respect to elevated temperatures such as those experienced during alpine descent, emergency stop and high energy driving conditions. Determine the feasibility of the proposed carbon fibre reinforced plastic wheel with respect to the challenge of strength degradation due to heating from the brakes.

This dissertation is structured into two parts. The first part details the development of the design process of a CFRP wheel from initial prototype to series production, the setup of the numerical models for analysis of the wheel, the experimental setup and procedure and the analysis of the laminate of the wheel. The second part details the investigation into the effect of temperature on the bending stiffness of the CFRP wheel, the experimental setup and the results of the thermal experiments. Proprietary details, such as the exact layup and material properties, are not published.

The design and development process of a carbon fibre wheel that is tested to certified standards and is commercially available on a production vehicle has not been published before this study. This study presents a novel approach for the analysis and possible weight reduction of a CFRP wheel automotive wheel. The determination of the effect of heat on the bending stiffness of a carbon fibre wheel at temperature had not been conducted before this study.

1.4. Published work

Parts of this dissertation have been published or accepted for publication in the works listed below:

1. Conference Paper – A conference paper was published in the proceedings of the 11th South African Conference on Computational and Applied Mechanics (SACAM 2018). The study presented the progress of the work presented in this dissertation. A poster

was presented at the conference and was awarded 3rd place in the poster presentation category.

2. Journal paper – An ISI journal paper was published in the Science and Engineering of Composite Materials. The paper presented a summary of the experiment conducted to validate the composite finite element model presented in this work. Published Online: 2019-08-07 | DOI: https://doi.org/10.1515/secm-2019-0018.

2. ISOTROPIC MODELLING OF THE WHEEL

This chapter details the development of the modelling and design process for a CFRP wheel. The first sub-section contains the initial development phase of the wheel and methodology used. The geometry of the wheel that forms the basis of this study was created in the CAD software package Solidworks. A simulated DCF test was modelled in ANSYS 17 approximating the wheel as an isotropic body. This was done to enable the identification and elimination of stress concentrations caused by geometrical features. The isotropic simulation of the wheel is detailed in sub-section 2.1. A mould was created and machined to define the geometry of the final isotropic configuration tested. An initial prototype laminate was created in the mould, which was manufactured to generate prototype specimens. The prototype laminate was replicated in a composite FE model using ANSYS Composite PrePost (ACP), detailed in sub-section 4.2. The first prototype specimen was tested by BST in a DCF test rig to the required ISO loads based on the vehicle specifications. A prototype wheel subsequently passed the required loads of the DCF test as specified in the TÜV [24] and ISO standards.

The first prototype wheel was fitted with aluminium hubs that had a mass of 1.2 kg. The geometry was chosen using a conservative approach to ensure that the wheel and hubs passed DCF testing and that the wheel could be delivered to the client on time. After the initial prototype was approved for fitment by the client after testing, a process was developed to redesign the aluminium hubs. The development of the process is detailed in subsection 2.2. A reduction in mass of the hubs was achieved and the established process was used to redesign the hubs on other automotive wheels manufactured by BST.

2.1. Isotropic Finite Element Model

2.1.1. Modelling geometry

A model was developed for the rear wheel as it had a higher test load requirement than the front wheel. The test loads are discussed later in this section. The wheel design was based on a generic 10-spoke configuration conceived by BST. A 3-dimensional CAD model of the wheel was created in Solidworks. The required dimensions of the wheel are shown in Table 2-1[1].

[1] It is standard industry practice to specify wheel diameter and width in inches, while the offset, bolt-pattern and centre bore are specified in millimeters.

Table 2-1 Dimensions of the modelled wheel

Vehicle	Diameter	Width	Offset	Bolt pattern	Centre bore
Rear wheel	18 inches	9 inches	0 mm	5x120 mm	72.6 mm

The brake assembly geometry was provided by the client to ensure enough clearance between the inside face of the wheel and the brake callipers. Figure 2-1 shows a representative cross-section of the wheel. The geometry of the pressurised side (tyre side) of the rim contour is strictly regulated. The profile conforms to the European Tyre and Rim Technical Organisation (ETRTO) standard. The wheel used in this work has a 9Jx18 profile with an offset of 0 mm. The offset determines the distance of the vehicle mounting face from the centreline of the wheel. When manufacturing carbon wheels, provision is made for aluminium hubs. Using the information provided by the client and the standards manual, an initial wheel geometry was created. A provision was made for a hub at 20 mm from the wheel centreline.

This geometry was saved as a Parasolid file to be used for linear static structural analysis. ANSYS Mechanical was used for the simulation. A simulated test was performed on the geometry assuming an isotropic material. This was done to identify possible stress concentrations on the surface of the geometry. Figure 2-2 shows the final CAD geometry of the wheel after stress concentrations were eliminated.

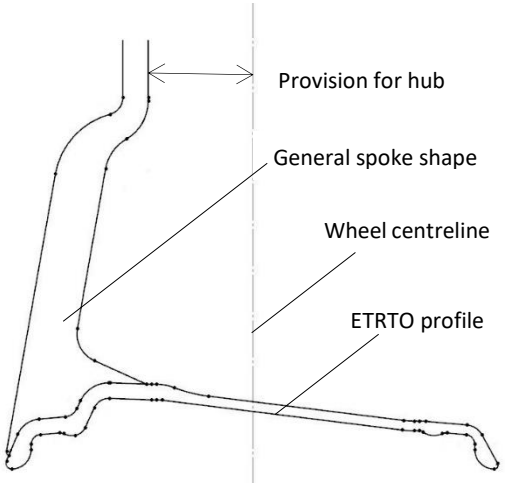


Figure 2-1 Representative geometry of a wheel profile



Figure 2-2 CAD geometry of the tested wheel

2.1.2. Idealisation

The first step of the finite element process is the idealisation of the geometry to simplify the simulation process. Simplifying assumptions were made to reduce the complexity of the geometry, as well as the overall surface of the body. Figure 2-3 shows the geometry of the wheel used in the first isotropic simulation. The wheel geometry was simulated without hubs, because at this stage of the development process no geometry existed for the hubs. In addition to this, it is seen as a more conservative case to simulate the wheel without hubs, as the load is applied directly to the wheel, resulting in higher loads.

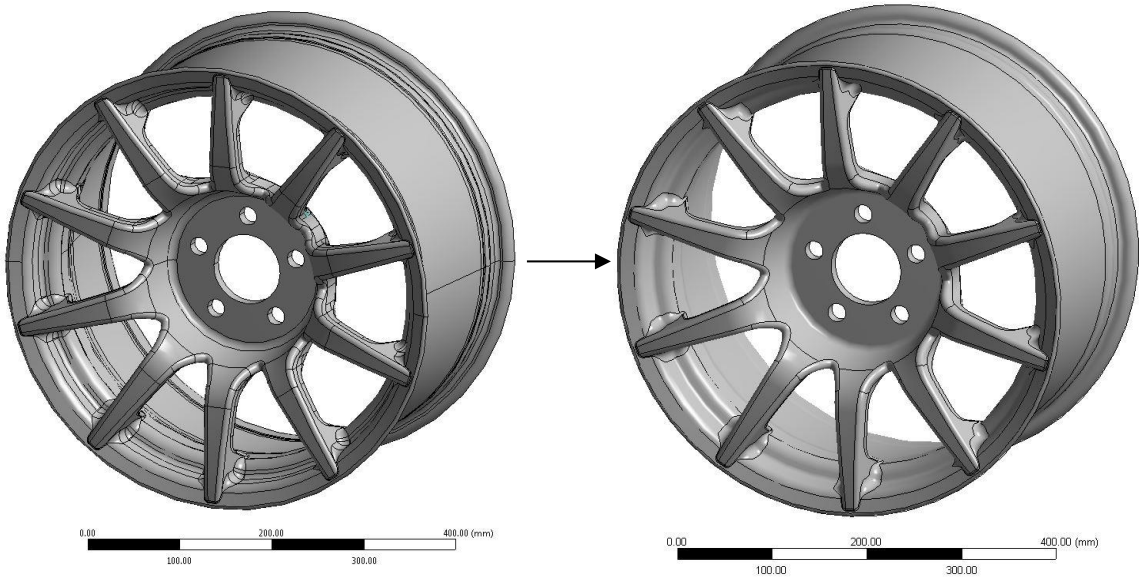


Figure 2-3 Wheel geometry used for the isotropic simulation of the CFRP wheel. Original body (left), Virtual Topology (right)

Before the DCF test can be modelled in FE software the geometry must be further simplified. A smoothed geometry, to assist with meshing, is created within the CAD software. Small (non-structural) features such as chamfers are removed. Geometrical symmetry, if applicable, can be used to further reduce the size of the body. In the case of the CFRP wheel, however, symmetry cannot be applied. The simulated load of the DCF test was applied in the direction of the spoke but offset at angles ranging from 0^o to 72^o.

Before the mesh can be created for the model, the surface of the geometry must be simplified. Lines on the surface of the geometry are a product of the output of the CAD software. These surface divisions are useful when sections of the wheel are required to be divided. These lines, however, automatically define the edges of elements during the discretisation of the geometry. The implication of this is that small surfaces on the body can lead to elements with poor aspect ratios or distorted sizes in relation to neighbouring elements. In addition, sharp edges created by adjoining features can causes a local bunching of elements as the meshing tools attempt to resolve a mesh around the body. FE software packages usually allow for surfaces to be combined to overcome this issue. Figure 2-3 shows the initial geometry used, as well as the simplified surface of the geometry. The geometry on the right has a lower number of surfaces, while retaining small surfaces between the spokes. This allows the mesh to be locally refined in the same manner between all the spokes.

2.1.3. Meshing

The geometry of the wheel was discretised into a mesh as shown in Figure 2-4. Due to the complex geometry of the wheel, a mesh with a large range of element sizes was utilised. The standard element size selected for the wheel was 10 mm. The entire wheel geometry was modelled to allow for the load direction to be varied as described in sub-section 2.1.40.

The initial mesh was generated with tetrahedral elements. During the meshing process it was discovered that the shape of the surface of the wheel was sufficiently complex, such that the FE software was unable to resolve a hexahedral (quad) element mesh on all surfaces. When using tetrahedral elements, precautions must be taken. When using tetrahedral elements, they must be used in combination with mid-side nodes (quadratic elements). It has been found in literature, that linear tetrahedral elements are excessively stiff [35]. This can induce significant errors and unrealistic results.

To investigate the validity of the solution, three simulations were run using slight variations in the mesh. Table 2-2 shows the properties of the meshes used for the simulations, the total deformation of the wheel, as well as the determined maximum stress. Each mesh was generated using a ten-node tetrahedral element (TET10). The average quality was included to indicate whether high stresses could be attributed to poorly refined mesh. The quality of an element is defined as the ratio of the volume to the edge length on a scale of 1 (perfect) to 0 (poor).

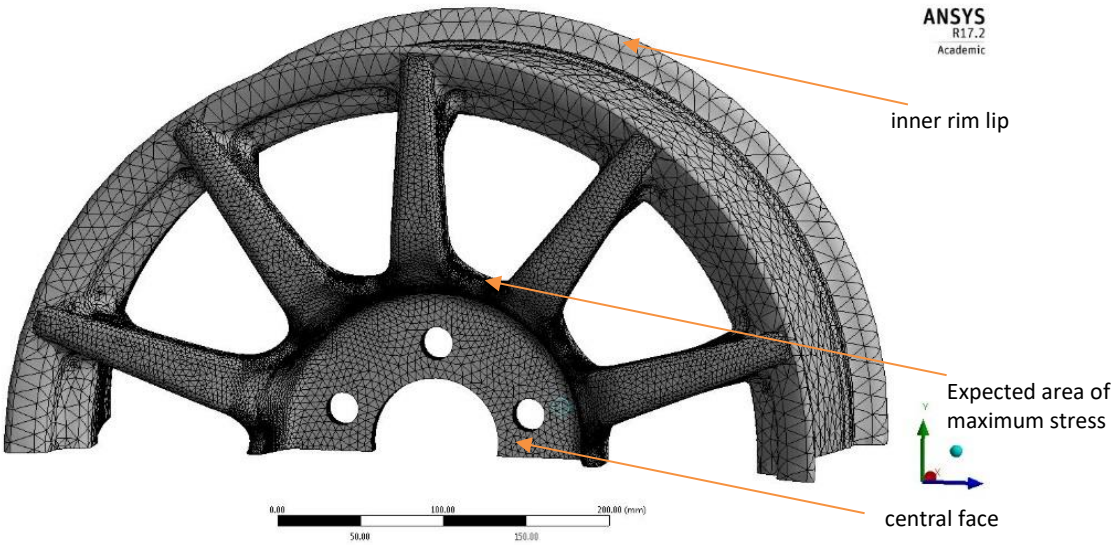


Figure 2-4 Mesh used in ANSYS mechanical for the isotropic approximation

Table 2-2 Simulation values of the initial isotropic simulation

Mesh	Element Type	Nodes	Elements	Average Quality	Max Stress	Total deformation
1	Ten-node Tetrahedral (TET10)	1 259 282	850 611	0.786	237 MPa	0.305 mm
2	Ten-node Tetrahedral (TET10)	1 423 795	966 432	0.790	264 MPa	0.305 mm
3	Ten-node Tetrahedral (TET10)	1 716 275	1 172 033	0.790	317 MPa	0.305 mm

The area with the highest expected stress, and thus the highest risk of failure was expected to be found on the surface between individual spokes as indicated in Figure 2-4. This decision was based on previous testing conducted by BST on a previous wheel design. The maximum stress shown in Table 2-2 did not converge. The exact converged value is not important but rather that a local stress concentration exists (which makes convergence challenging). The wheel geometry was redesigned to eliminate the stress concentration as detailed in Section 2.1.6, and the mesh independence is detailed in Section 2.1.5.

2.1.4. Test setup

To determine the stress in the wheel during an instant of the DCF test, a bending stiffness test was simulated. This represents an instantaneous snapshot of the DCF test. A fixed support was applied on the inner rim lip. This is the location on the physical wheel that is clamped during a DCF test as per the TÜV and ISO standards. The bending load (M_B) was applied to the central face using a remote force applied at 1 m from the hub. This allows the applied force (in newtons) to be equal to the required bending moment in magnitude. A remote force takes a more conservative approach, as it approximates a rigid load arm. The maximum reference moment was calculated using Equation 1 [24]. This load corresponds to the required test load as specified in ISO 3006:2015.

$$\boldsymbol{M_{Bmax} = f \times F_R(\mu \times r_{dyn} + e)} \quad (1)$$

where M_{Bmax} = reference moment [N.m],

f = wheel load increase factor,

F_R = maximum static wheel load [N],

μ = coefficient of friction between tyre and road,

r_{dyn} = dynamic tyre radius of the largest intended tyre [m], and

e = wheel offset [m].

The Y and Z-axes of the applied load were parametrised in the FE software. The load was applied in 20 discrete directions that varied at an angle of 0° to 72° to the spoke in the Y-Z Plane. 72° corresponds to the angle between holes.

2.1.5. Solution and mesh independence

To evaluate each iteration of the geometry, project solutions were analysed. A measurement of the total equivalent stress on the wheel showed a maximum of 237 MPa. Figure 2-5 shows the distribution of stress on the wheel during loading. In the figure shown, the load was applied along the Y axis (in line with a spoke). There was a noticeable stress concentration between the spokes. Further mesh iterations were modelled with the same loads and constraints. The further iterations were intended to show mesh independence and to better resolve the area of high stress.

It was noted that the stress between the spokes increased in each simulation, without changes to the stress distribution on the spokes or stresses further on other parts of the surface between the spokes. The stress concentration led to the redesign of the geometry of the wheel.

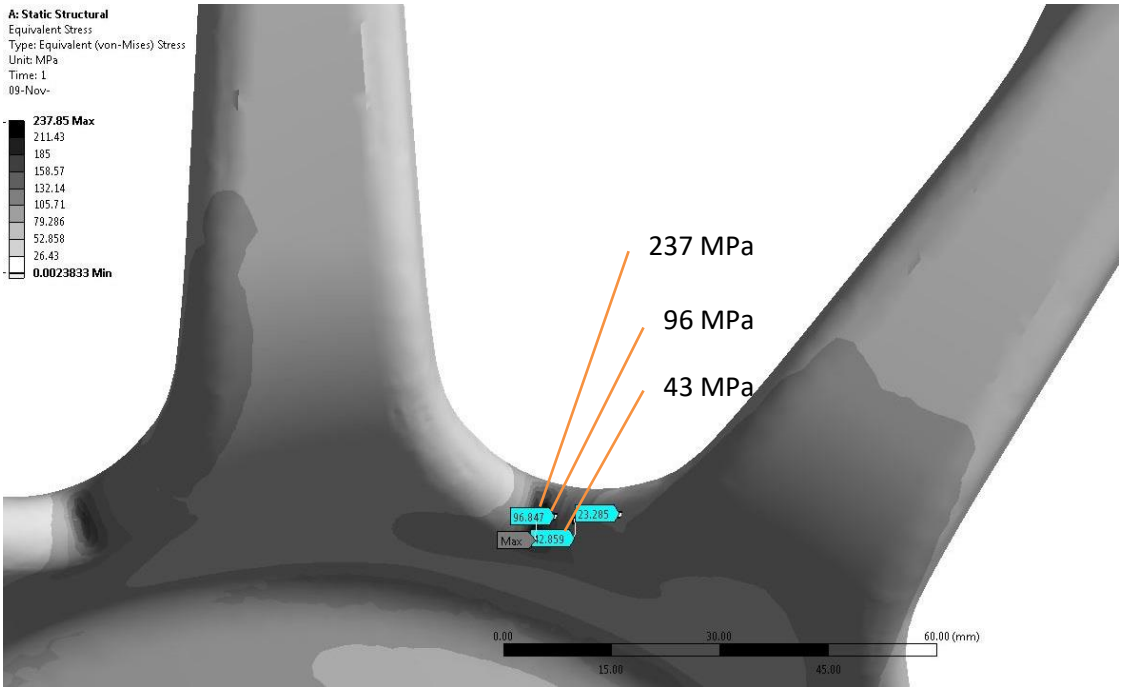


Figure 2-5 Equivalent stress on the initial isotropic FE model

2.1.6. Improvements made to the wheel

Using the results of the initial isotropic simulations, the geometry of the wheel was updated. Figure 2-2 shows the improved geometry of the wheel. The spoke length was reduced to allow for a more gradual change of curvature between the individual spokes. These changes were made to eliminate the stress concentration between the spokes.

The simulation was rebuilt with the updated geometry using the same methodology. The load was applied at angles ranging from 0^o to 72^o and the maximum stress on the face between the spokes was recorded for each applied load. The recorded stresses were available for post processing and are shown in Table 2-3. The maximum stress measured on the faces between the spokes was determined from the table and this load case is presented. The design point with the highest load and the stress distribution on the spoke is shown in Figure 2-6. From the figure one can see that the stress is more uniformly distributed along the spoke towards the

centre of curvature. Of importance when analysing an isotropic model of a wheel is the rate of change of stress on the surface of the body, rather than the value of stress. It is known that the stress values shown are not equal to the stresses in an equivalent orthotropic material. Areas of high stress in an isotropic model can be used to identify locations where more emphasis should be placed on the laminate to strengthen the wheel. Due to the nature of the manufacturing process of composite wheels, emphasis should be placed on the connecting face between spokes.

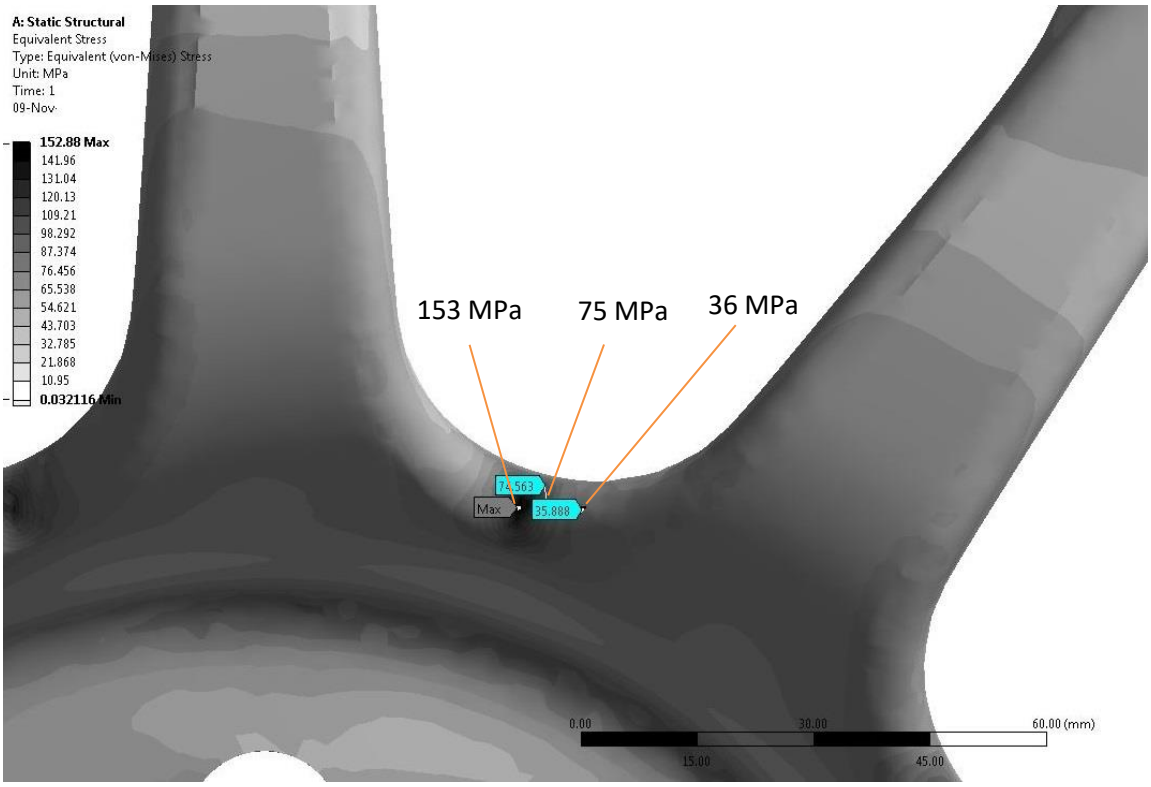


Figure 2-6 Equivalent stress in the modified isotropic model

Table 2-3 Maximum stress on each face between spokes at discrete load directions

Angle	Face 1 (MPa)	Face 2 (MPa)	Face 3 (MPa)	Face 4 (MPa)	Face 5 (MPa)	Face 6 (MPa)	Face 7 (MPa)	Face 8 (MPa)	Face 9 (MPa)	Face 10 (MPa)
0	147.05	95.24	46.44	95.63	150.56	139.77	96.35	47.06	95.57	142.44
3.6	149.31	101.66	47.60	88.92	146.97	142.47	102.58	47.44	89.45	140.19
7.2	151.03	107.80	50.62	82.44	142.84	144.63	108.52	49.60	83.16	137.43
10.8	152.20	113.61	54.64	76.79	138.21	146.25	114.12	53.47	76.77	134.20
14.4	152.82	119.05	59.40	71.05	133.10	147.32	119.35	58.04	70.36	130.49
18	**152.88**	124.11	65.21	65.30	127.52	147.83	124.19	64.19	64.06	126.35
21.6	152.39	128.73	71.15	59.64	121.52	147.78	128.59	70.74	58.00	121.78
25.2	151.34	132.91	78.47	54.19	115.13	147.17	132.55	77.49	53.39	116.81
28.8	149.74	136.62	85.85	50.38	108.39	146.01	136.03	84.31	49.33	111.49
32.4	147.60	139.84	93.09	48.27	101.95	144.29	139.02	91.08	46.00	105.83
36	144.93	142.55	100.10	47.07	96.12	142.03	141.51	97.72	46.22	99.89
39.6	141.74	144.75	106.83	46.86	90.03	139.24	143.49	104.16	47.86	93.71
43.2	138.05	146.41	113.24	48.72	83.75	135.93	144.94	110.34	50.49	87.34
46.8	133.88	147.53	119.29	52.50	77.33	132.12	145.85	116.21	54.05	80.87
50.4	129.25	148.12	124.93	56.72	70.85	127.81	146.23	121.73	59.45	74.37
54	124.18	148.15	130.13	61.84	64.41	123.04	146.07	126.87	65.29	67.95
57.6	118.72	147.64	134.88	67.35	58.14	117.83	145.37	131.59	71.37	61.77
61.2	112.88	146.59	139.14	72.87	52.22	112.20	144.14	135.87	77.57	56.00
64.8	107.81	145.00	142.90	78.41	49.22	106.18	142.38	139.67	83.76	50.89
68.4	102.41	142.87	146.13	85.32	47.32	99.81	140.10	142.99	89.86	47.78
72	96.69	140.23	148.83	92.12	46.32	93.12	137.93	145.81	95.80	46.80

2.2. Aluminium Hub Simulation

The first prototype wheel was fitted with aluminium hubs that had a weight of approximately 1200 g. The geometry was chosen using a conservative approach to ensure that the wheel and hubs passed DCF testing and that the wheel could be delivered to the client on time. The first prototype wheel was tested in a BST facility on a DCF test rig. The test was conducted to the required load as specified by ISO 3006:2015. The test load was determined using Equation 1, shown in Section 2.1.3. The number of cycles tested was in accordance with the draft of the composite testing standard developed by TÜV. After the wheel was delivered to the client, an optimised design was required, to further save weight.

Figure 2-7 shows the geometry of the initial hub (inner) that was used on the prototype wheel. This geometry represents the first phase of the development of hubs for a CFRP wheel. While this was not the final version that was delivered to the client, the development steps of the

hubs proved useful in determining an optimal approach for development of future projects. The geometric constraints of the intended vehicle must be taken into consideration during this phase. The process for the development of the prototype hubs considered the following:

- The depth (thickness) of the hub was chosen to be equal to the space allocated during the design of the shape of the wheel (Section 2.1.1).
- A cylindrical section in the centre of the hub was included to allow the final wheel to be mounted on the centre bore of the vehicle.
- The number of holes and the placement thereof was defined by the PCD of the intended vehicle.
- An effort was made to save weight without compromising the structural integrity of the hub.

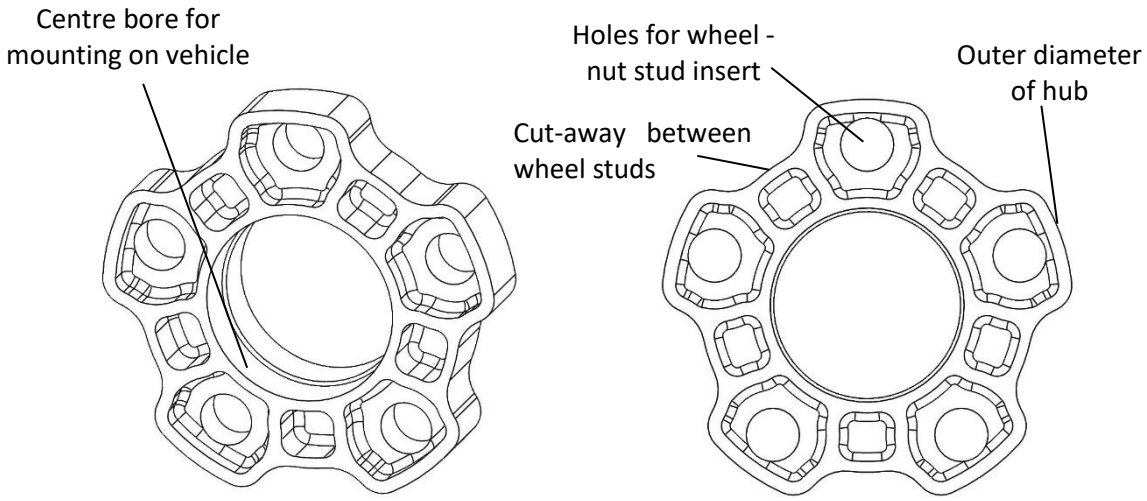


Figure 2-7 Inner hub used on the first prototype wheel

Figure 2-8 shows the cross section of the completed hub assembly used on the first prototype. The hub assembly was intended to make use of an outer hub and aluminium sleeves, through which the wheel lug nuts/bolts would connect the wheel to the vehicle. The outer hub was designed to distribute the load that was applied by the wheel nut torque (pre-load force), as well as the dynamic loads of the vehicle. The aluminium sleeves were connected to the inner hub by means of an interference fit.

Figure 2-9 shows the CFRP wheel with the three-part aluminium hubs fitted. The design requirement presented at this stage was to reduce the weight of the aluminium hubs, while removing the outer hub completely for aesthetic reasons. To address this challenge, and to

determine the methodology for future wheel developments, a static structural model of the hub assembly was created.

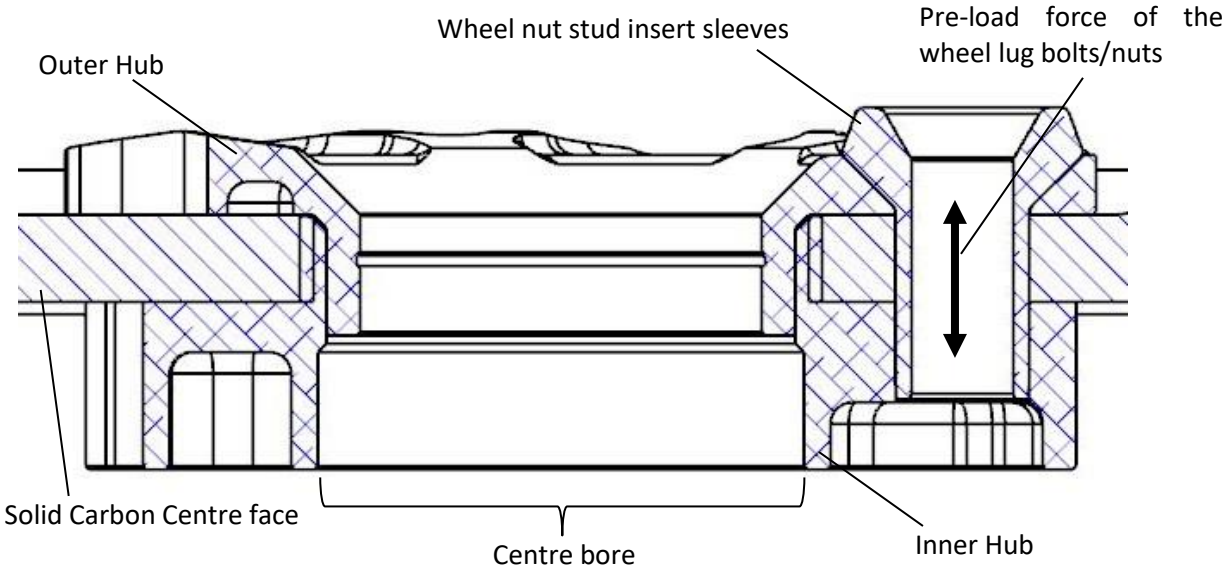


Figure 2-8 Cross-section of the initial hub assembly

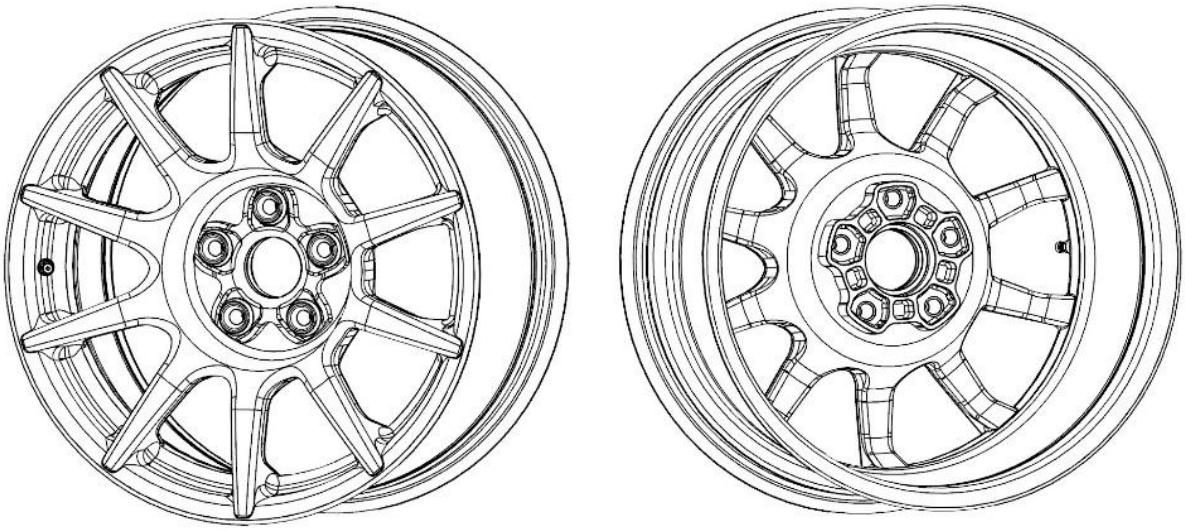


Figure 2-9 Initial prototype wheel with 3-part aluminium hubs

2.2.1. Modelling geometry idealisation

The initial aluminium hub assembly was made up of an inner hub, outer hub and 5 sleeves, through which the bolts connected the wheel to the vehicle. The replacement geometry to be investigated consisted of an inner hub and 5 sleeves, without a front hub. The newly designed sleeves were required to distribute the load directly to the wheel in place of an outer hub. The initial assembly chosen for analysis consisted of the original inner hub with newly shaped stud inserts.

Figure 2-10 shows a schematic of the geometry imported into a linear static structural FE simulation. The hub components were assembled along with a load arm and simple studs to replicate the behaviour of bolts. A disc modelled as aluminium was used in place of a full wheel geometry to reduce computing time and provide a conservative standard platform for the simulation, as well as future simulations. The diameter of the disc was chosen to be larger than the face of the wheel. The bolts and the load arm were modelled in steel, while the inner hub and the circular disc were modelled in aluminium (6082-T6). The aluminium sleeves were modelled using a high tensile grade aluminium (7075-T6). The material properties of the aluminium used are tabulated in Table 2-4 [36,37].

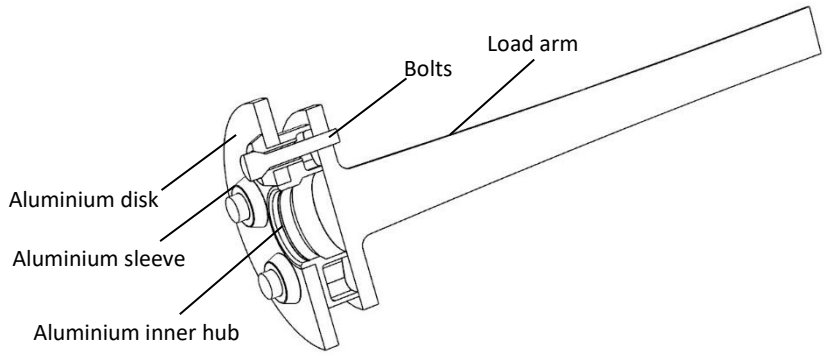


Figure 2-10 Geometry used for validation of new hub geometry

Table 2-4 Material properties of Aluminium 6082 and 7075

Property	6082-T6	7075-T6
Ultimate tensile strength (σ_{UT})	290 MPa	572 MPa
Tensile yield strength (σ_{YT})	250 MPa	503 MPa
Endurance strength[2] (σ_E)	95 MPa	159 MPa
Compressive yield strength (σ_{YC})	250 MPa	500 MPa

Before the assembled geometry could be modelled in a FE software suite, the geometry had to be further idealised in the CAD software:

- Non-structural features such as chamfers were removed from the inner hub.
- The diameter of the shank of the aluminium sleeve was set equal to that of the hole in the inner hub. The true interference fit was modelled as a bonded connection.

[2] Endurance strength taken at 500,000,000 cycles completely reversed stress

2.2.2. Contacts and meshing

As this simulation was performed on an assembly, it was necessary to define contacts between the bodies. Contacts were defined for any surfaces that had a separation of less than 0.25 mm. The surfaces between the bolt and the load arm were defined as bonded[3]. The surfaces between the stud insert and inner hub were set to bonded. All other surface connections were defined as frictionless. A frictionless connection allows for separation of the surfaces, as well as frictionless sliding between the surfaces.

Figure 2-11 shows the mesh used to investigate the hub geometry. A global mesh was generated with an initial element size of 3 mm. The mesh was generated with a mixture of tetrahedral and hexahedral elements that were quadratic (including mid-side nodes). A body-specific element size of 8 mm was applied to the load arm. A body-specific element size of 4 mm was applied to the bolts. An element size of 1 mm was applied to the wall thickness of the inner hub. The mesh consisted of 1 574 122 nodes and 992 233 elements with an average quality of 0.83.

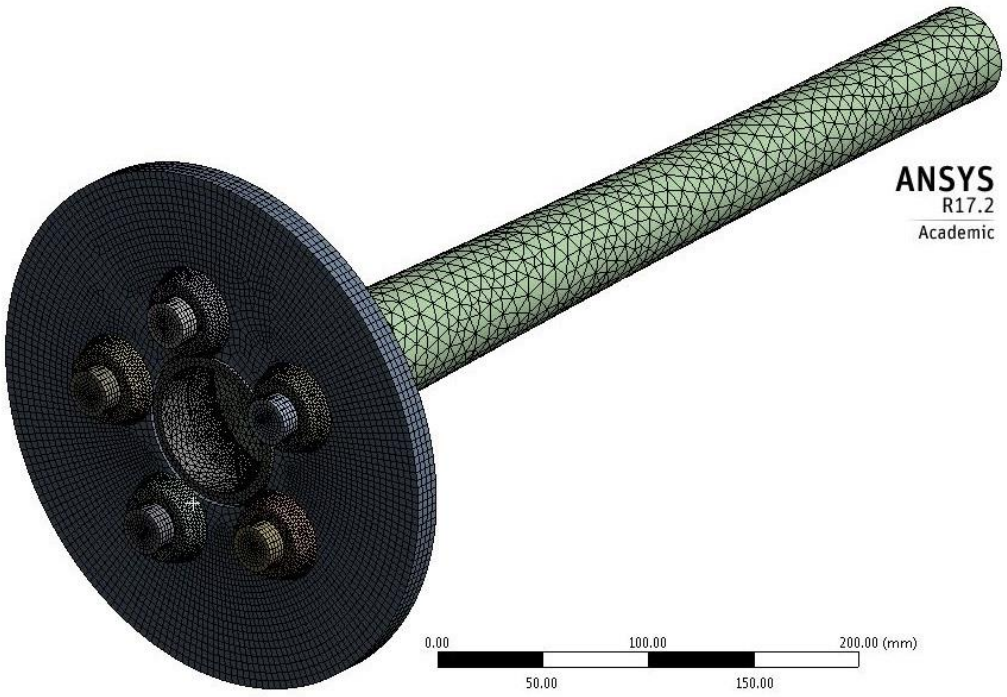


Figure 2-11 Mesh used to develop the improved hubs

[3] A bonded connection is defined as a connection that does not allow sliding or separation.

2.2.3. Test setup

As with the isotropic model detailed in Section 2.1, the load case chosen to evaluate the hub assemblies was a static DCF test. Initial iterations were also tested using a torsional fatigue load case, which was found to have significantly lower stresses. The DCF test was simulated on the hub assembly using a fixed support on the outer face of the circular disc. A bolt pre-tensioning force was applied to the bolts. Equation 2 was used to determine an approximate pre-load force.

$$\boldsymbol{F_p = \frac{T_w}{K D_B}} \quad (\mathbf{2})$$

where $F_p = \text{bolt pre-load force [N]}$,

$T_w = \text{required wheel nut torque [N.m]}$,

$K = \text{increase factor } (0.2), \text{ and}$

$D_B = \text{effective bolt diameter [m]}$.

With a required torque of 110 N.m (as specified by the client), a pre-load force of 48 kN was calculated. The first simulation run on the geometry to be tested were the initial conditions. The result of the initial conditions was compared to a second load case. The second load case included a force that was applied on the face of the end of the load arm. The applied force was calculated to cause a bending moment equivalent to the required ISO bending moment of the DCF test. The load was applied in 20 discrete directions between 0° and 72° relative to the first bolt hole.

The maximum stress of the combined load case, as well as the stresses during the initial conditions were recorded and retained for detailed analysis.

2.2.4. Result of the isotropic hub analysis

The first configuration that was chosen for analysis consisted of the original inner hub that was fitted with newly designed stud inserts. Figure 2-12 shows the stress distribution of the original inner hub. The combined load caused a stress of 198 MPa. While this falls below the yield stress allowance of the material, the distribution of the stress on the outside wall thickness was deemed unsuitable for further consideration.

The original intention of the outer profile and the use of pockets was to reduce the weight of the hubs, while giving the wheel a unique aesthetic look. Further iterations of the inner hub

using the same shape resulted in an increase of the weight of the inner hub, with little impact on the stress distribution.

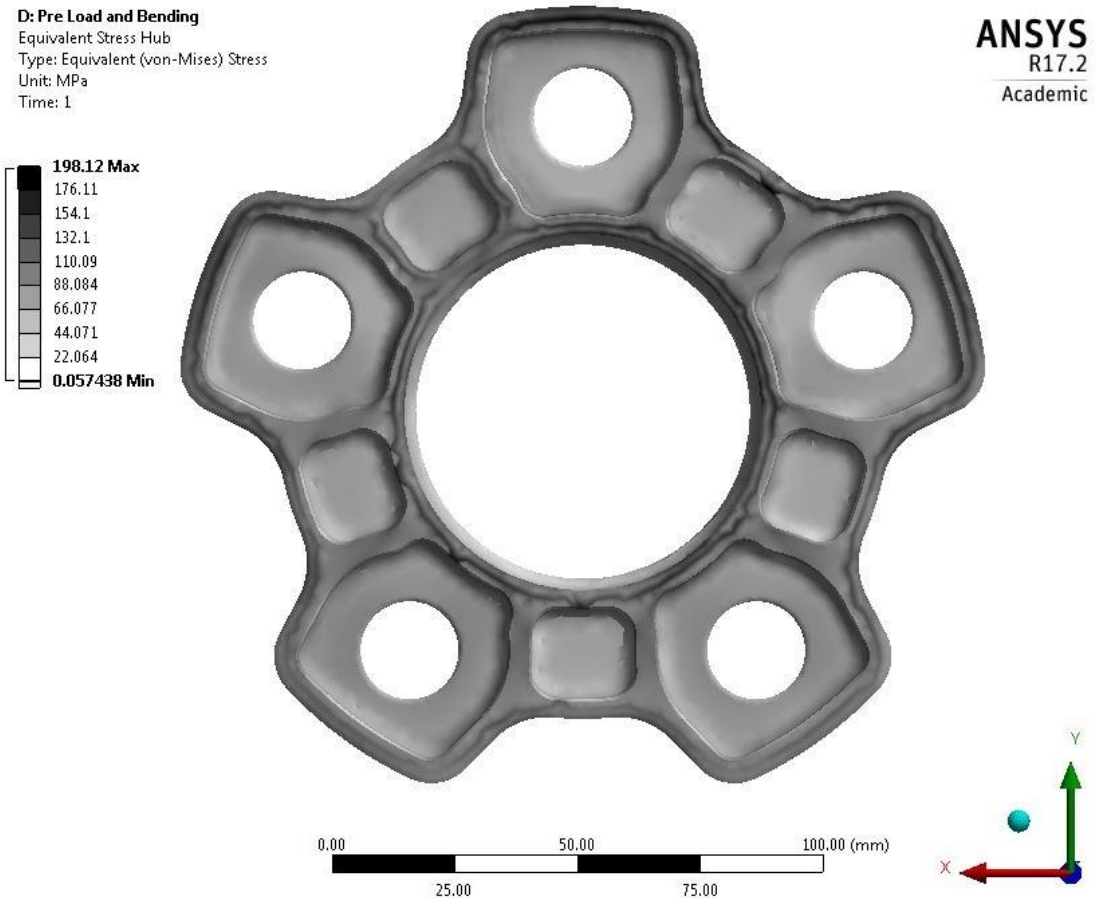


Figure 2-12 Stress distribution on the prototype inner hub

To reduce the stress the indentation of the outer profile of the hub was reduced. Reducing the indentation of the outer profile resulted in a reduction in mass of the inner hub. This step was contradictory to the original assumptions that were made when designing the prototype hub assembly. The outer shape of the hub was therefore changed to be fully circular. This resulted in a reduction in the calculated mass of the inner hub. The inner hub used in the initial prototype wheel (floral shape) had a mass of 700 g. The inner hub that was analysed with a circular profile had a calculated mass of 600 g. Figure 2-13 shows the original inner hub used on the prototype wheel and the inner hub that was used on the production wheel. The effect of the circular outer profile allowed more material to be removed between the wheel nuts than had been removed from the initial prototype hub.

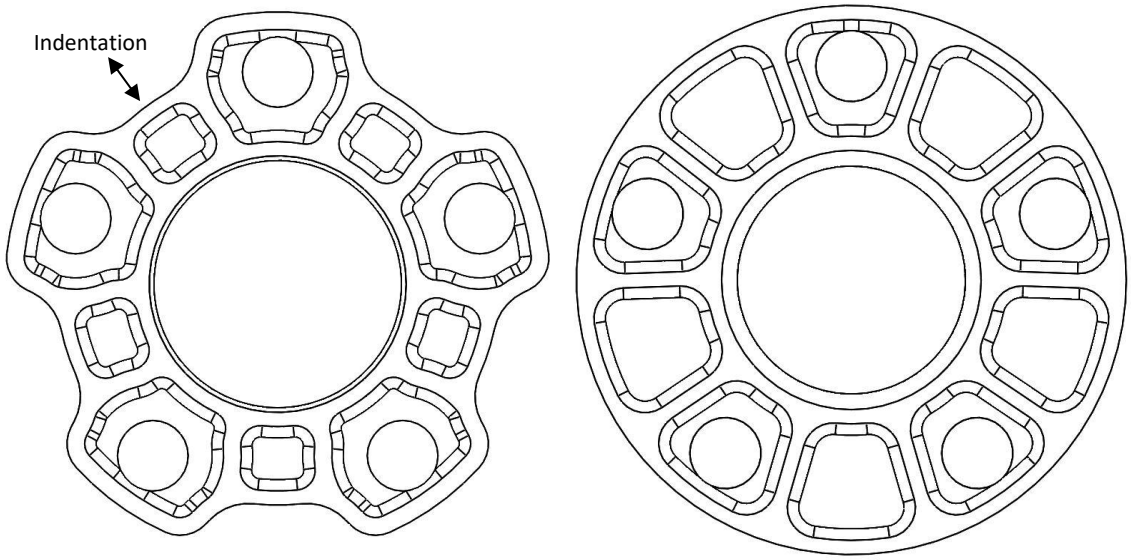


Figure 2-13 Front view of the inner hub. Prototype (Left) Production (Right)

The newly shaped circular inner hub was assembled with the stud insert sleeves and analysed in a static structural simulation using the same methodology as defined for the first prototype hub. Figure 2-14 shows the cross-section of the hub assembly used on the production wheel. The new profile of the stud insert sleeve uses a circular face that is located directly on the carbon wheel to distribute and transfer the load through the hub assembly.

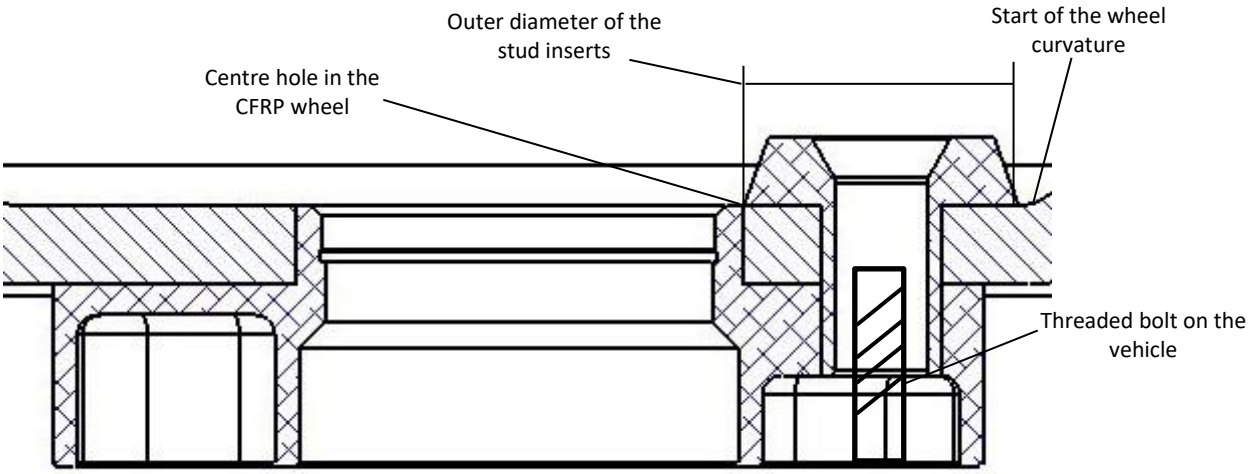


Figure 2-14 Cross-section of the production hub assembly

The design constraints of the stud insert sleeve became apparent while developing this new methodology. The existing vehicle specifications must be considered when determining the shape and dimensions of the hubs on a CFRP wheel. It is important that the wheel nuts (lug nuts) have enough thread engagement when the wheel is mounted to the vehicle. During simulations it was determined that the primary method of reducing stress in the stud insert

was to increase the outer diameter of the stud insert. The larger surface area available for the transfer of the load was determined to be more beneficial than increasing the wall thickness or raising the conical face.

The shape of the wheel that was used for the development of this method was not allowed to be changed. A note was made for future wheel developments to consider the size of the outer hub before the manufacture of the wheel. The development of the hubs for the wheel in this study were done within the existing constraints. Figure 2-15 shows the stress distribution during bending throughout the inner hub that was used on the production wheel. The maximum stress value calculated was sharply reduced from that of the original design. In addition to the reduction of the maximum stress value, the stress distribution was greatly improved.

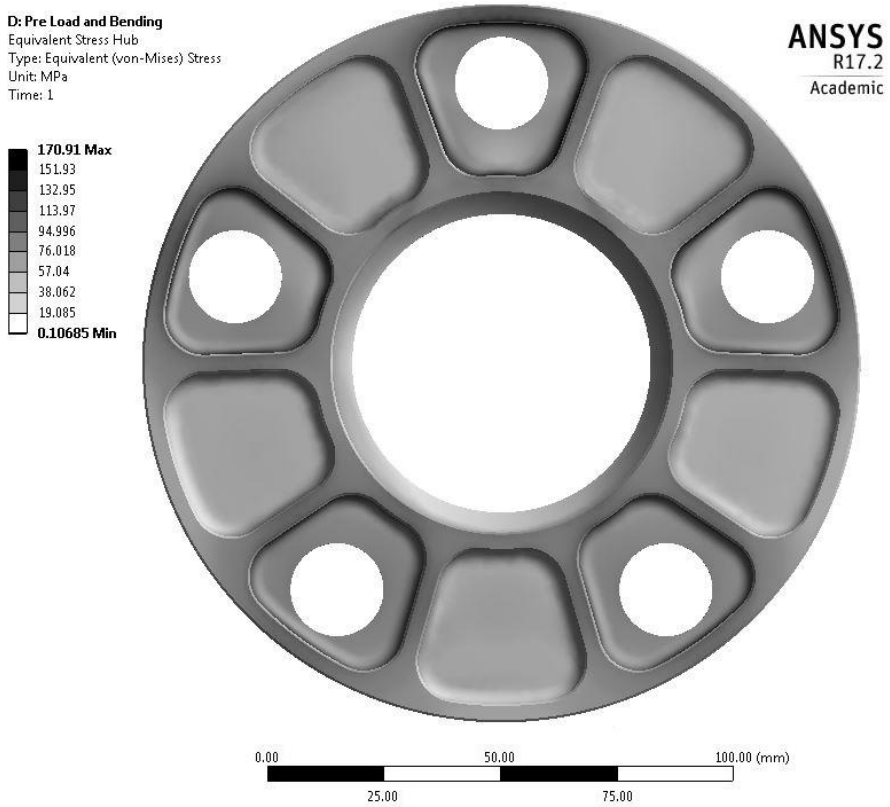


Figure 2-15 Stress distribution on the inner hub of the production wheel

To determine the feasibility of the design to withstand the load, the pre-load and the combined load cases were compared. In the combined load case, the area of maximum stress was identified. The initial conditions were inspected to determine the stress at the location of the maximum stress in the combined load case. In addition, locations throughout the hub

were probed to determine the location with the largest change in stress. The initial conditions were assumed to represent the minimum stress (σ_{min}) experienced by the part. The combined load case was assumed to represent the range of stress (σ_R) on the part. The mean (σ_m) and alternating (σ_a) stresses were calculated. Using an approximate value of the endurance strength (S_e) of 95 MPa [38] the fatigue life of the hub was estimated. Figure 2-16 shows the fatigue curve of the improved rear wheel hub. The design point is shown. Soderberg, Modified Goodman and Langer criteria were used to evaluate the factor of safety of the component.

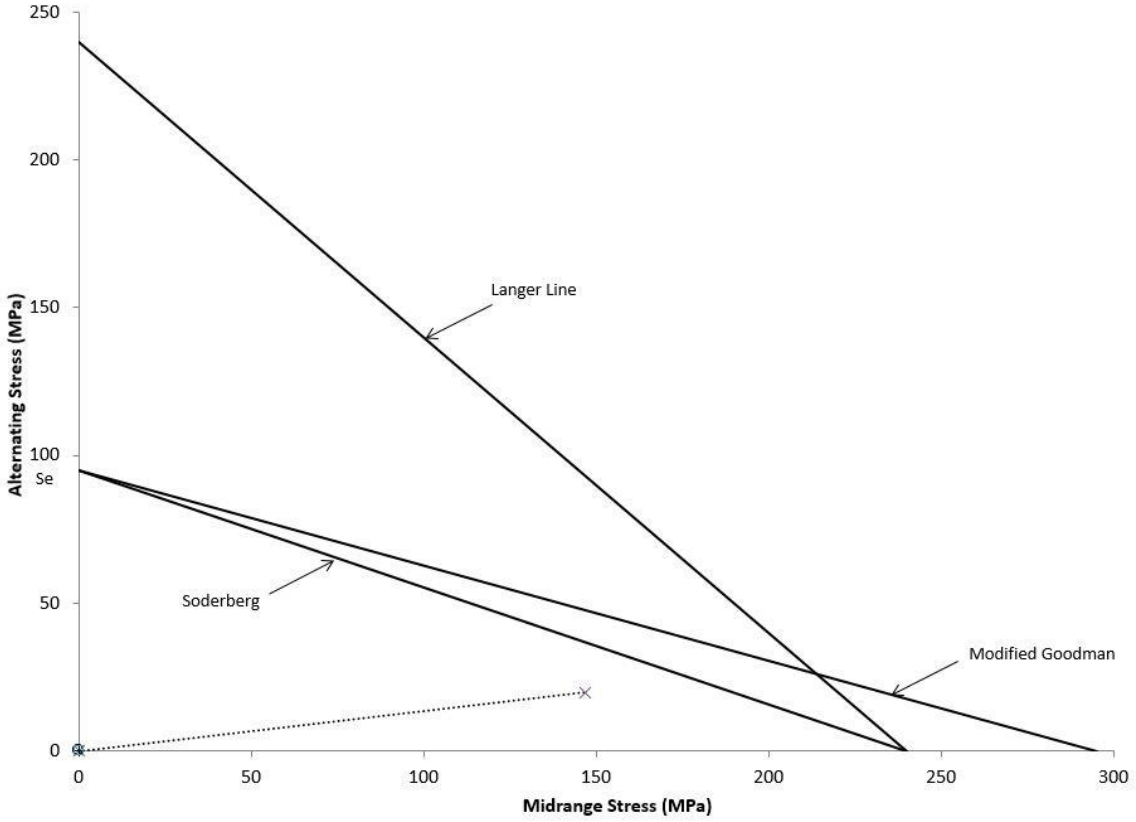


Figure 2-16 Fatigue curve of the improved wheel hub design

In addition to the FE simulation run on the hub, a further CFRP prototype wheel was tested on the DCF rig. The improved hubs were fitted to the wheel. The wheel assembly passed the DCF test to the required loads. The improved assembly had a combined mass of 897 g, resulting in a saving of 229 g from the initial design. The DCF test conducted on the prototype wheel and hubs served to validate the design method and provided a foundation to understand future developments. Figure 2-17 shows the final hub design used on the wheel. The wheel shown has since been delivered to the client, where it is available as OE on a road vehicle.

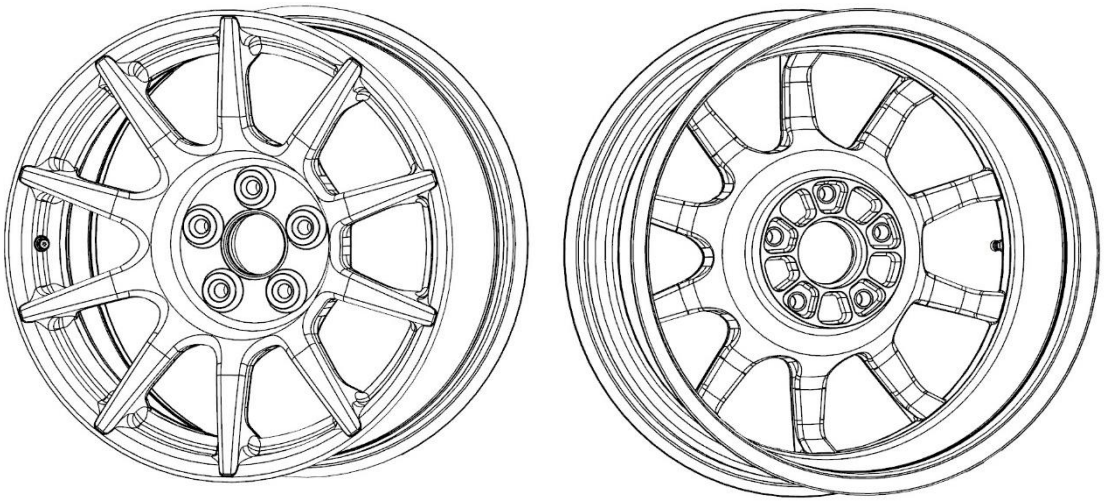


Figure 2-17 Production wheel with 2-part aluminium hubs

2.3. Summary

This chapter detailed the development work to determine an appropriate methodology to begin the design of a CFRP wheel for a road going vehicle. The development process of the rear wheel intended for a Donkervoort D8-GTO was used to develop this methodology.

A wheel was designed in CAD software to the vehicle specifications of a Donkervoort D8-GTO. An isotropic FE model was created to determine geometrical feasibility before the production of composite tooling could begin. The isotropic FE model of the wheel was found to be useful in identifying surface imperfections that could negatively affect the performance of the composite laminate. Unlike isotropic materials, carbon fibres must be placed in long lengths, with low values of curvature.

A further isotropic FE study was conducted to optimise the aluminium components of the wheel assembly before the wheel entered production. The development of the improved aluminium hubs was conducted after the first CFRP prototype wheel had been tested on a DCF rig. The development of the aluminium hubs was used to improve the methodology for future development of wheels. The new process that was implemented at BST after this study made a provision in the development of the wheel for alterations in the shape and use of the aluminium hubs. A weight reduction of 229 g was achieved on the aluminium components through the work conducted for this study. Additional weight savings could have been achieved if the development of the hubs had been conducted in parallel with the development of the wheel shape.

Figure 2-18 illustrates the development timeline of the carbon wheel in this study. The development process of the methodology was divided into prototyping and optimisation phases. The wheel entered production before the completion of this study. The FE models developed in this study were intended to determine an improved process of developing CFRP wheels in future. This chapter describes part of the work conducted to achieve objective 1 (see Section 1.3). A carbon fibre reinforced polymer wheel was manufactured to withstand dynamic cornering fatigue loads as specified by TÜV following the methodology outlined in ISO 3006 – 2015 for a passenger vehicle.

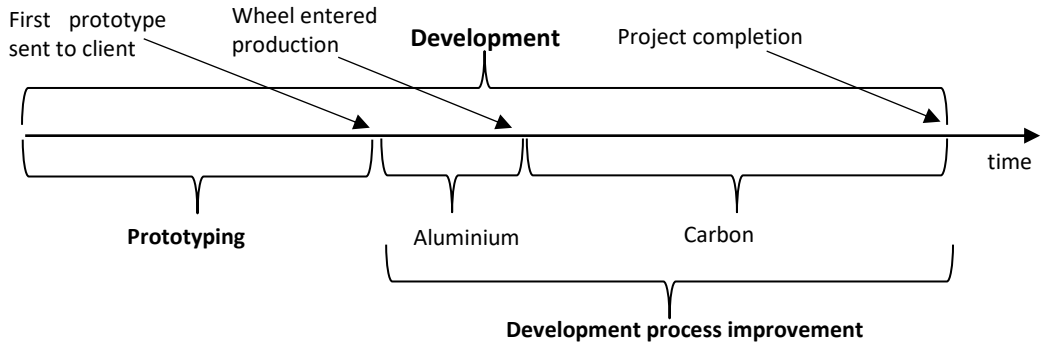


Figure 2-18 Illustration of the development of the improved methodology

3. EXPERIMENTAL TESTING OF THE CFRP WHEEL

This chapter details the experimental work conducted on the prototype CFRP wheel. An experiment was performed on a prototype CFRP wheel after the wheel had entered production. The apparatus used to test the wheel is described. The instrumentation used is listed and explained. The experimental procedure is described. The apparatus used was made up of existing equipment in the BST testing facility. The experimental data was later used for comparison to numerical data obtained from a composite FE model. The experimental work was conducted to gain an understanding of the performance of the laminate and to highlight areas of improvement for future development processes.

3.1. Bending Moment Test Rig

Part of the development process of a CFRP wheel includes the determination of the bending stiffness of the wheel. This is performed while qualifying the mechanical properties of the part and can sometimes be conducted to determine whether the requirements set out by the client have been met.

Figure 3-1 shows the setup of the experimental apparatus used to test the wheel. The test rig is used to determine the bending stiffness of a wheel. The bending stiffness of the wheel was measured before the DCF test was conducted. A force was applied at the end of a set of fixtures that comprise a load arm. The load arm transferred a bending moment to the mounting face of the wheel. The deflection of the load arm was measured with a dial gauge at a measured distance. The dial gauge was mounted to the steel frame by means of a magnetic foot. The dial gauge has a resolution of ±0.005 mm. A second dial gauge was positioned to measure the deflection of the edge of the rim. The applied force from the hydraulic actuator was measured in kgf using a load cell. The testing equipment used pre-existing load arms and spacers, and thus the direction of the applied force was limited. The direction of the load application was between two instrumented spokes, detailed in Section 3.2.

This testing method was selected as it was possible to replicate the applied load in the composite FE model. In addition to replicating the loads in the composite FE model, this testing method approximates an equivalent static load case of the DCF test. The applied load approximates the equivalent response of the wheel for the moment that the DCF test rig loads the wheel in the same direction.

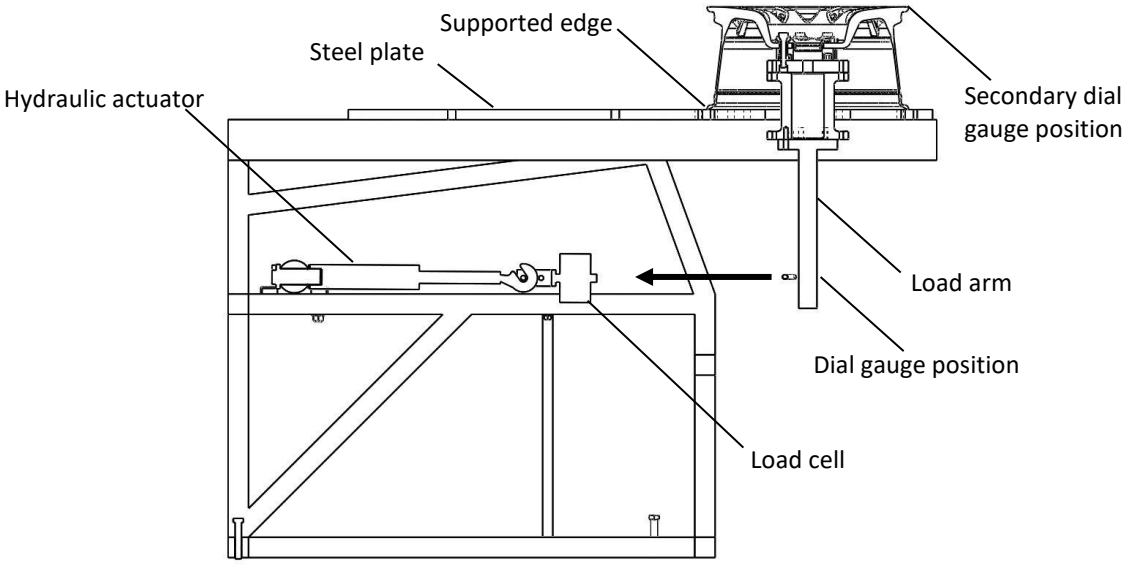


Figure 3-1 Cross-sectional schematic of the test apparatus used

3.2. Instrumentation

The experimental prototype was instrumented with 4 Kyowa KFRP-5-350-C1-1 strain gauges suitable for composites that were placed on the outer surface of the wheel on the spokes. Figure 3-2 shows the position of the strain gauges on the wheel. The surfaces selected for positioning strain gauges were flat and were simple to match with intersecting points on the FE model. Strain gauge 1 (G1) was positioned on a spoke in line with a bolthole, labelled spoke 1. Strain gauge 2 (G2) was placed on an adjacent spoke labelled spoke 2 which was anticlockwise to spoke 1. Strain gauge 3 (G3) was placed opposite of strain gauge 1, while strain gauge 4 (G4) was placed opposite of strain gauge 2.

The technical specifications of the gauges are listed in Table 3-1. The gauges were mounted on the surface of the wheel with Kyowa CC-33A adhesive. The surface was prepared before the gauges were applied. Lines were etched onto the surface of the wheel to aid with gauge placement. Acetone was used to remove residual oils on the surface of the spokes. The surface was roughened with 200 grit sandpaper. The adhesive was generously applied to the mounting area. The gauges were placed and held in position with gentle pressure for 1 minute each. The gauges were left for 24 hours to allow the adhesive to cure fully before testing.

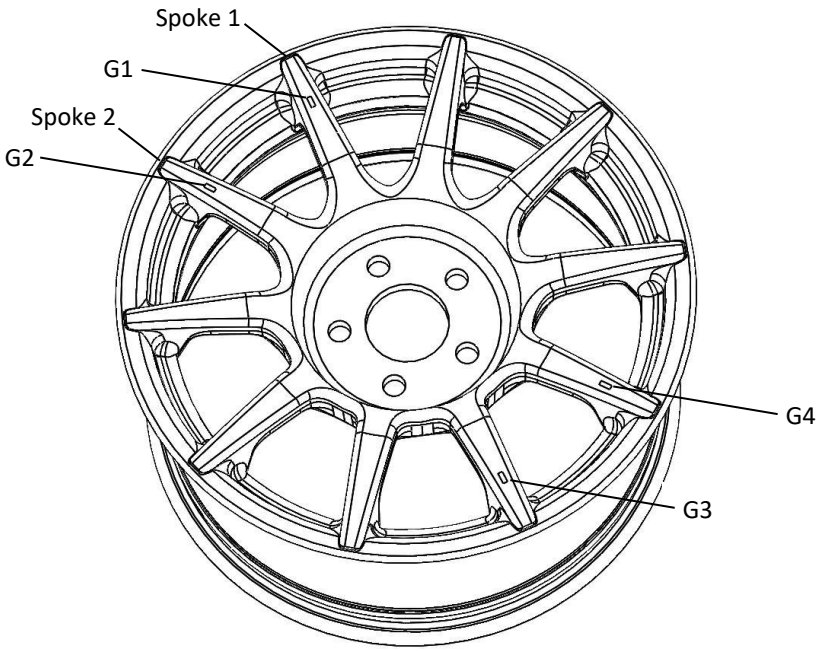


Figure 3-2 Placement of strain gauges on the experimental prototype

Table 3-1 Technical specifications of the strain gauges

Item	Details
Gauge factor	2.02 ± 1.5 %
Gauge resistance	350 Ω ± 1.2Ω

Table 3-2 Instrumentation used on the experimental prototype

Item	Name	Quantity
Strain gauge	Kyowa KFRP-5-350-C1-1	4
Cable	Twisted three core shield cable	4
Chassis	National Instruments SCXI-1000	1
Strain gauge card	National Instruments SCXI-1520	1
Terminal block	National Instruments SCXI-1314	1
Data acquisition controller	National Instruments SCXI-1600	1
Computer software	PC with LabView	1

The strain gauges were connected to a National Instruments data acquisition system. The details of the instrumentation used is detailed in Table 3-2. While precautions were taken to align the gauges along marked lines, misalignment of the gauges was observed after the adhesive had cured. The observed direction of the misalignment of the strain gauges (i.e.

angled away or from the centre or direction of loading) was noted. The gauge misalignment was estimated to be less than 5 degrees. Figure 3-3 shows one of the strain gauges that was found to be slightly misaligned.

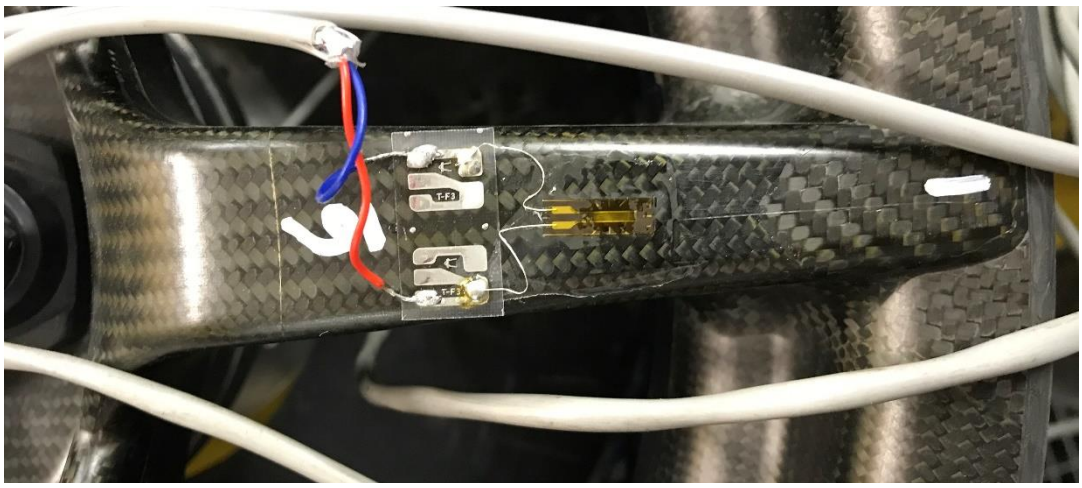


Figure 3-3 Photograph of the applied strain gauges

3.3. Methodology

3.3.1. Experimental procedure

The direction of load application was chosen to be between spoke 1 and spoke 2. This allowed the measurements of the gauges to be compared to one another. As the testing equipment used pre-existing load arms and spacers, the direction of possible load application was limited. The combination of bolt-hole configurations limited the load application on the wheel to positions that placed the load arm hook towards the hydraulic cylinder.

The wheel was bolted to the load arm using lug bolts that were tightened to 110 N.m. The wheel and load arm were positioned on the steel plate of the test rig. The load arm extended through a hole in the steel plate. The wheel was aligned to allow load application between the spokes. The wheel was clamped down using 8 CNC step clamps and hex socket bolts. The actuator and load cell were connected to the load arm by means of a chain. As the chain and load cell have a mass which must be accounted for, the actuator was retracted until the slack in the chain was removed. The load cell was set to zero from this point and all loads were measured from this datum.

A maximum applied load of 300 kg from the established datum was selected. It was observed that the actuator could not reliably maintain pressure above this load. The wheel was loaded in 30 kg increments to the maximum load. The applied load was reduced in the same increments to provide more data points and to investigate hysteresis. Before the data was recorded, the wheel was twice loaded to the maximum and subsequently unloaded to remove possible slack in the system.

The applied force was read from a digital display and recorded manually for each load step. The digital display had an uncertainty of ±0.5 kg. The load was constant while the strain gauge readings were recorded individually in LabView for each load step. The actuator maintained the load without losing pressure at low loads. Minimal loss of force was observed under the 300 kg maximum. The load arm deflection was read from the dial gauge for each load step and recorded manually. The sampling rate was set at 1000 Hz, the cut-off frequency of the low pass filter at 100 Hz, and the strains for a given applied load were recorded over a minimum period of 3 seconds to be averaged to reduce error caused by noise. The room temperature was measured at the start and finish of each experiment. In each experiment the room temperature remained constant for the duration of the test. To compensate for thermal changes in the strain gauges, the data acquisition controller was switched on and left for a duration of 30 minutes prior to the start of testing.

3.3.2. Data processing

As stated in Section 3.3.1, the strains were recorded for a minimum of 3 seconds for each load step. The LabView project used for the bending stiffness measurement was provided by the BST testing department. The gauge properties of the gauges used were entered in the LabView project for each gauge. The sampling rate was set at 1000 Hz. Each gauge was assigned an initial voltage. The measured strain was observed to be constant for each load step with some noise. The LabView project output one TDMS file per load step with *time* vs. *measured strain* values. Each TDMS data file was saved in an XLSX format to be processed in Excel. An average was taken of the values of measured strain from each gauge. The average value obtained from each load step was combined into a single document, and the manually recorded load and deflection values of each load step were appended.

The initial voltage given to each gauge resulted in an initial *measured strain.* The *measured strain* from the first load step (0 kg) was used to normalise the remaining *measured strains* to

reflect the overall change. The *measured strains* were plotted in micro strain ($\mu\varepsilon$) against the applied load on the shaft.

The strain gauges used have stated uncertainties as listed in Table 3-1. A calculation was performed to determine the propagation of error based on the manufacturer stated specified variance in gauge factor and gauge resistance. Equation 3 relates the measured change in resistance (ΔR) to the gauge resistance (R) and the strain on the surface (ε) with the gauge factor (GF):

$$\boldsymbol{GF = \frac{\Delta R}{R\varepsilon}} \tag{3}$$

Rearranged this gives:

$$\boldsymbol{\varepsilon = \frac{\Delta R}{R(GF)}}$$

Defining the uncertainty of the gauge resistance as $\underline{\Delta}R$ (±1.2 Ω), and the uncertainty of the gauge factor as $\underline{\Delta}GF$ (±0.0303), the uncertainty in the measured strain $\Delta\varepsilon$ is determined by:

$$\boldsymbol{\Delta\varepsilon = \sqrt{\left(\frac{\delta\varepsilon}{\delta R} * \underline{\Delta}R\right)^2 + \left(\frac{\delta\varepsilon}{\delta GF} * \underline{\Delta}GF\right)^2}} \tag{4}$$

where,

$$\boldsymbol{\frac{\delta\varepsilon}{\delta R} = \frac{\Delta R}{R^2(GF)}} \tag{5}$$

and,

$$\boldsymbol{\frac{\delta\varepsilon}{\delta GF} = \frac{\Delta R}{R(GF^2)}} \tag{6}$$

yielding,

$$\boldsymbol{\Delta\varepsilon = \sqrt{\left(\frac{\Delta R}{R^2(GF)} * \underline{\Delta}R\right)^2 + \left(\frac{\Delta R}{R(GF^2)} * \underline{\Delta}GF\right)^2}} \tag{7}$$

The uncertainty was calculated for each measured data point individually.

3.4. Results of the Bending Stiffness Test

This section presents the results of the physical testing. A mechanical test was performed on the experimental prototype wheel using a bending stiffness rig. The wheel was instrumented with strain gauges to record strains on the surface of the spokes for comparison to values obtained from a numerical simulation, detailed in Section 4. The deflection of the load arm, as well as the deflection of the edge of the rim were measured. After the wheel was tested on

the bending stiffness rig, it was removed, repositioned and retested to investigate the repeatability of the experiment.

3.4.1. Bending stiffness of the wheel

The test rig applied a static bending moment in one direction only which modelled an equivalent static load case of an instant in time of the DCF test. A schematic of the test rig is shown in Figure 3-1. The wheel movement in the DCF test is small and thus the corresponding inertial forces are insignificant (justifying the use of an equivalent static load approximation). This has been confirmed with FEA simulations comparing the static loading stresses to a full dynamic case. Previous research [7,8] has used FEA of the equivalent static loading case to model the DCF test.

The load was applied between the instrumented spokes such that the load arm hook was towards the hydraulic cylinder. Two experimental tests (test 1 and test 2) were run. Test 2 was a repeat of test 1, where the wheel was removed from the rig, repositioned, clamped and tested again. The test was repeated to measure test-retest variability. Figure 3-4 shows the deflection of the load arm during the experimental tests. The deflections are linearly related to the loading as expected. The measured values of deflection are in close agreement between test 1 and test 2, indicating the experiment is repeatable. The difference in measured deflection of approximately 0.3 mm between loading and unloading and the deflection not returning to zero at the end of the test, indicate a small amount of hysteresis present.

In addition to the measured deflection of the load arm, the deflection of the edge of the wheel rim was also measured. Table 3-3 lists the measured deflection of the edge of the wheel rim during the experiment. The difference in measured deflection of approximately 0.06 mm between loading and unloading and the deflection not returning to zero at the end of the test, indicates a small amount of hysteresis present. The deflection data presented would indicate that there was a small amount of sliding of the wheel on the surface of the steel plate. The wheel was clamped on the surface of the steel plate with a set of step clamps. The torque applied to the bolts of the step clamps did not completely eliminate the sliding of the wheel.

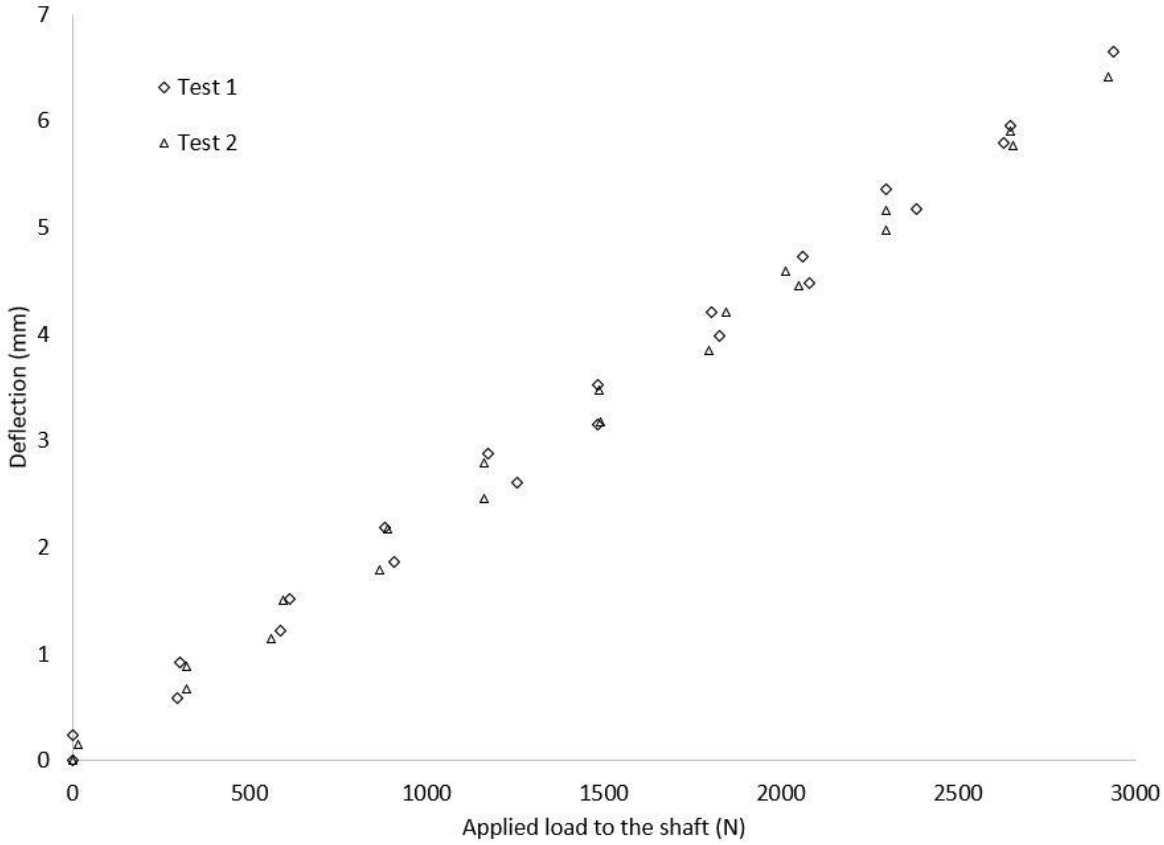


Figure 3-4 Deflection of the load arm for test 1 and test 2

Table 3-3 Measured displacement of the edge of the wheel rim

Load (kg)	Displacement of the lip (mm)
30	0.015
60	0.023
90	0.038
120	0.053
150	0.068
180	0.105
150	0.098
120	0.110
90	0.102
60	0.088
30	0.072
0	0.060

Figure 3-5 shows the measured strains of gauges G1 to G4 versus an increase in applied load on the bending stiffness apparatus. Uncertainty in the measurement was determined from the propagation of error considering the manufacturer specified variance in gauge factor and gauge resistance. The calculated error was insignificant and not included in the figure. The differences in measured strain of ±2 $\mu\varepsilon$ between incremental loading and unloading indicate a small amount of hysteresis present in all measurements. The experimentally measured strain values increase linearly as expected. It was expected to obtain similar readings between gauges G1 and G2; as well as G3 and G4. However, notably different strains in gauges between G1 and G2; as well G3 and G4 were observed. As stated in Section 3.2, the strain gauges were observed to have slight misalignment from the centreline of the spoke. It was noted that the gauges that were misaligned at an angle closer to that of the applied load had a higher measured strain. The opposite was observed when gauges were misaligned away from the applied load. Gauge G3 was observed to be well aligned.

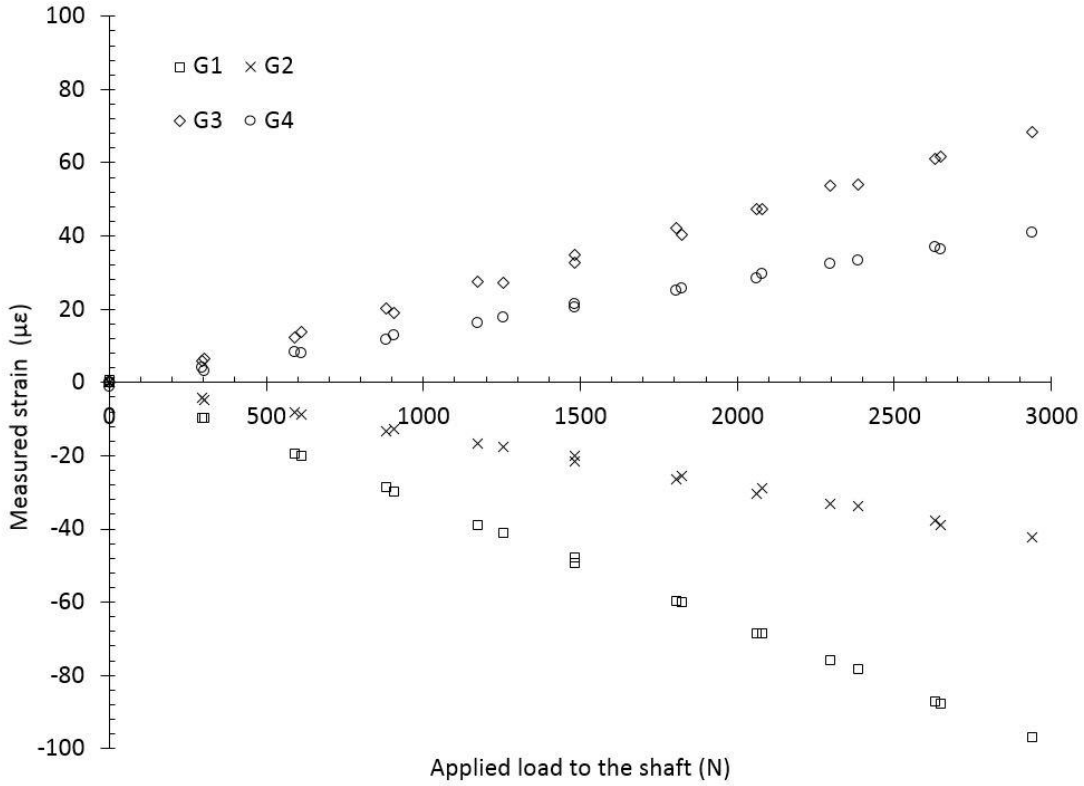


Figure 3-5 Measured strains on the surface of the wheel

Figure 3-6 shows the measured strains of gauges G3 and G4 versus an increase in applied load on the bending stiffness apparatus for two sets of experiments. The wheel was removed from the rig, repositioned, clamped and tested again for the second test. The second test was conducted to investigate test-retest variability. As with the first test, the experimentally

measured strain values increase linearly as expected. The differences in measured strain of ±2 $\mu\varepsilon$ between incremental loading and unloading indicate a small amount of hysteresis present in each of the tests. The maximum measured strain in each of the tests has a difference of approximately ±2 $\mu\varepsilon$. The difference equates to a variance of approximately 2.7 % between each of the tests. Analysis of the deflection of the load arm, as well as the measured strains of the second test would indicate that the experiment is repeatable.

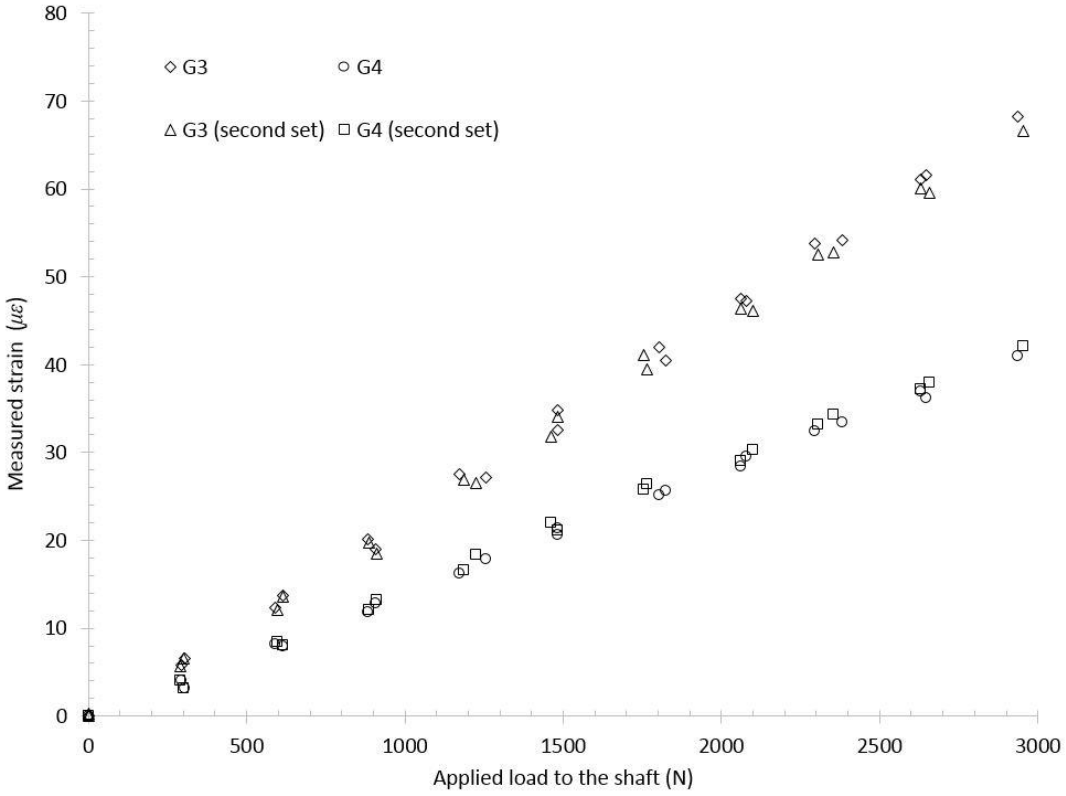


Figure 3-6 Measured strains of experiment 1 and 2

3.5. Cornering Fatigue Test

Among other tests required to fully certify the CFRP wheel used in this study for use on the market, a CFT test was conducted on the wheel. The wheel was tested to the required loads as specified by TÜV No. 287 30 StVZO following the methodology defined in ISO 3006:2015. The ISO standard defines how the wheel is to be tested, while the TÜV standard defines the minimum conditions required for the specimen to be certified. The TÜV standard specifies that a wheel is to be tested at 75 % of the calculated moment (M_{Bmax}) for 200 000 cycles, followed by 50 % of M_{Bmax} for 1.8 million cycles, where M_{Bmax} is defined in both standards by Equation 1 as stated in Section 2.1.4.

The test is conducted by clamping the wheel on the flange of the outer lip. An axle is fitted to the wheel. The wheel nuts are torqued as required by the manufacturer. The load arm is connected to the axle of the DCF rig with an eccentric mass. An electric motor spins the axle. This creates a force at a specified distance away from the hub face. Load cells, placed on the load arm, are used to calculate the bending moment on the wheel. The number of cycles were counted electronically. As the frequency of the motor increases, the applied force increases, and hence, a greater bending moment. The motor frequency (and the load), typically changes when the stiffness of the hubs or wheel changes. There are frequency variations in the motor frequency that are caused by the motor controller. Small changes, however, have negligible effect on the test parameters. The motor controller outputs the motor frequency against the number of cycles at the end of the test. A significant decrease in motor frequency is indicative of a loss in stiffness in the test rig.

The wheel design intended for use on the Donkervoort D8 GTO was tested using the DCF rig before and after the development of the improved hubs (Section 2.2). The wheel that was tested achieved the required number of cycles at the specified loads without reduction of the frequency of the motor. This would indicate that the methodology used to develop the laminate (detailed in Section 4.1) and the aluminium hubs was valid. At this stage of the study, however, it was not known if the laminate of the CFRP was over-designed. Further work is required to determine whether additional weight savings are possible.

3.6. Material Properties of the Carbon Fibre Fabrics

It was determined that the material properties of the fabrics used in the wheel had to be obtained by first principles. While a finite element model of the composite wheel was constructed prior to the testing of the fabrics, the material properties of the materials used were not available in literature or from the material supplier. Unlike isotropic materials, such as aluminium and steel, material properties cannot be found in standard tables. Suppliers of carbon fibre fabrics work closely with individuals or companies to create fabrics that are best suited for the final product. The tailored changes of fabric properties, varying resin contents (in the case of prepreg) and chemical composition of the resin influence the mechanical properties of the laminae.

To define a fabric in the FE software required the definition of the orthotropic elasticity, orthotropic stress limits and orthotropic strain limits of the *laminae* (individual sheets). The

stress and strain limits are important when attempting to predict failure using the model. The orthotropic elasticity is required to determine the mechanical response of the geometry to applied loading conditions. Orthotropic elasticity is defined by the Young's modulus in the axial directions (E_X, E_Y, E_Z), the Poisson's ratio in the directional planes (v_{xy}, v_{yz}, v_{xz}) and the shear modulus in the directional planes (G_{XY}, G_{YZ}, G_{xz}). First principles validation of the FE computation was conducted and is detailed in Appendix A.

Tensile testing was conducted to determine the material stiffness of the fabrics to be used in the FE model. The measured stiffness was compared to the materials in the FE database. The composite FE model had been set up prior to the material testing, as the values obtained could be included in the FE model at a later stage.

3.6.1. Material samples

The tensile testing test was conducted in accordance with ASTM 3039 [39]. Material samples were manufactured to test two material types. Material type A was a plain woven prepreg material. Five specimens of material type A were manufactured. The experimentally determined value of Young's modulus in the loaded direction (E_X) was determined to be valid for the secondary direction (E_Y). The out-of-plane stiffness (E_Z) was not measured. Material type B was a unidirectional (UD) prepreg material. Five specimens were manufactured with a fibre orientation of 0° to determine E_X. Additional specimens were manufactured with a fibre orientation of 90° to determine the value of E_Y.

An equal number of layers were cut using a CNC cutting table. The individual layers were stacked on a flat aluminium plate and enclosed in a vacuum bag. The plate was placed in an autoclave to cure. The finished material test plates were cut to the required sizes using a pneumatic rotary grinder. The ASTM standard recommended UD materials at 0° have the dimensions 15 x 250 mm, while UD materials cut at 90° were recommended to be 25 x 175 mm. Symmetric (woven) materials are suggested to be 25 x 250 mm in size.

The test specimens were numbered from 1 to 12 and were measured using a Vernier calliper to determine the average width and thickness. Table 3-4 lists the dimensions of the tested samples. Of the five UD (90°) specimens manufactured, three fractured during the cutting process. It was noted that the average thickness of the 90° UD plates was noticeably thinner than the 0° UD plates.

Table 3-4 Dimensions of the test specimens

	Specimen	Average width (mm)	Average thickness (mm)
Woven	1	25.88	3.35
	2	25.62	3.38
	3	25.82	3.40
	4	25.18	3.34
	5	25.53	3.30
UD (0^o)	6	15.49	3.10
	7	15.43	2.97
	8	16.36	2.96
	9	15.43	2.95
	10	15.78	3.01
UD (90^o)	11	25.76	2.84
	12	26.40	2.71

3.6.2. Apparatus and methodology

The test specimens were tested in the materials testing laboratory at the University of the Witwatersrand in Johannesburg. A Shimadzu tensile tester was used to load the specimens. A laser extensometer was used to measure the distance between two reflective tabs. The displacement of the tabs was recorded. The extensometer and the tensile tester both recorded a data file to a computer with LabView installed. A LabView project file was provided by the laboratory to save the measurements of the instrumentation.

Figure 3-7 shows the tensile testing machine used. Reflective tabs were applied to the test specimens approximately 45 mm apart before clamping in the tensile tester. Figure 3-8 shows the laser extensometer used for the experiment. The extensometer was positioned so that the laser was centred on the tested specimen. The maximum load of the Shimadzu was 20 kN. The crosshead stroke had an extension rate of 1 mm/min. The sampling rate of the laser extensometer was 100 Hz.

The UD (0^o) test specimens and the woven test specimens did not fracture. The displacement of the tabs was observed to be linear after approximately 1 minute. The initial displacement of the crosshead was large while the components of the gripping mechanism tightened up. UD (90^o) test specimens fractured at low load, as expected. Because of the fracture at low load, there was a significant amount of noise in the readings and the resolution of

measurement using the 20 kN load cell was poor, but acceptable. There was, however, still an observable linear trend in the data.



Figure 3-7 Shimadzu tensile testing machine used at the University of the Witwatersrand



Figure 3-8 Laser extensometer used for material testing

3.6.3. Data processing

The data from the LabView project consisted of approximately 30 000 individual data points. Data points were recorded 100 times per second. Each data point included the applied force (as output by the tensile testing machine) and the measurement of the distance between the centres of the reflective tabs. The initial reading of the distance between the reflective tabs was used as a reference datum. The displacement, and hence the extension of the specimen was calculated by determining the difference of the measurements with respect to the first point. Negative displacements as a result of noise were disregarded. The stresses and strains were calculated for each point based on physical dimensions of the individual specimens.

3.6.4. Fibre volume fractions

To enable a detailed analysis of the laminate, fibre volume fractions (F_F) were calculated. The mass of the specimens is tabulated in Table 3-4 was measured. The fibre volume fraction was calculated using the equation below.

The mass of an object in terms of volume fractions is given by:

$$\boldsymbol{m_e = V_{tot} * \rho_F * F_F + V_{tot} * \rho_R * F_R} \quad (8)$$

where,

V_{tot} – Total volume of the specimen [m^3]

ρ_F – Density of the fibres [kg/m^3]

ρ_F – Density of the resin [kg/m^3]

F_F – Fibre volume fraction

F_R – Resin volume fraction

and,

$$\boldsymbol{F_F + F_R = 1} \quad (9)$$

which yields,

$$\boldsymbol{m_e = V_{tot} * \rho_F * F_F + V_{tot} * \rho_R - V_{tot} * \rho_R * F_F} \quad (10)$$

and, finally,

$$\boldsymbol{F_F = \frac{m_e - V_{tot} * \rho_R}{V_{tot} * \rho_F - V_{tot} * \rho_R}} \quad (11)$$

Using the measurements and Equation 11, the fibre volume fractions of the test specimens were determined. In addition, a CFRP test wheel used in this study was cut into sections for analysis. A section of the spoke was cut to allow for the determination of the fibre volume

fraction. The mass of the specimen was measured. The volume of the specimen was determined by submerging it in water. The fibre volume fractions of the specimens are tabulated in Table 3-5. It is interesting to note that the fibre volume fraction of the UD specimens at 90 degrees is notably higher than that of the UD specimens at 0 degrees.

Table 3-5 Fibre Volume Fractions of the specimens

Specimen	Average Fibre Volume Fractions (F_F) (%)
Woven	55
UD (0^o)	65
UD (90^o)	72
Wheel Sample	68

In addition to the mechanical testing that was conducted during the timeframe of this study, the maximum allowable stresses in compression and tension were provided by the material supplier for woven and unidirectional materials. The provided values were stated to have been based on a fibre volume fraction of 60 %. The values provided by the material supplier are not published in this study for proprietary reasons.

3.6.5. Result of the material testing

Tensile testing was conducted to determine the material stiffness of the fabrics used in the FE model. The measured stiffness was compared to the materials in the FE software materials library. The tensile testing test was conducted in accordance with ASTM 3039 [39]. Five specimens of material type A (plain woven) were manufactured in an autoclave. The specimens were cut to size based on the recommendations of ASTM 3039 for "balanced and symmetric" specimens.

Figure 3-9 shows the test results of the plain-woven material (specimens 1-5). All the test specimens remained in the elastic region up to the maximum force of the tensile testing machine (20 kN). All the specimens exhibited a linear response to the tensile load and were of approximately the same gradient (E_1). The displacement of the reflective tabs was observed to be linear after approximately 1 minute. Prior to this, substantial movement was seen in the specimen grips. In this time there was an applied force measured. Once the movement of the grips had settled the displacement measured by the extensometer became linear. A value of Young's modulus (E1 and E2 respectively) was obtained for the plain-woven material based

on the gradient of the data. The calculated value of stiffness was within 10 % of the value in the FE material library.

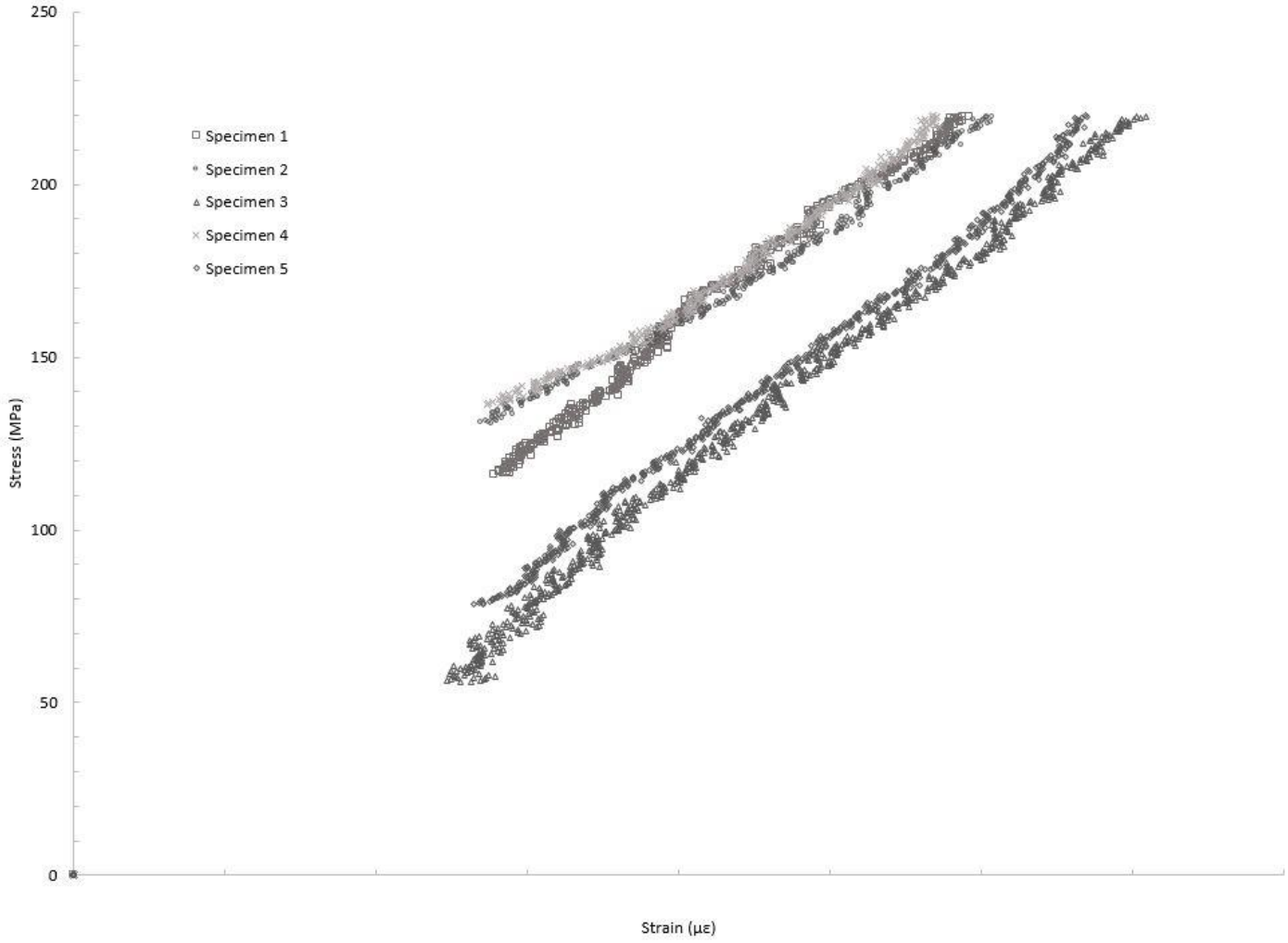


Figure 3-9 Tensile testing results of the woven material

Figure 3-10 shows the test results of the UD material at 0 degrees (specimens 6 and 8). The testing of specimens 7, 9 and 10 did not yield measurable results. It was determined during data processing that specimens 7, 9 and 10 had slipped in the grips of the tensile testing machine. The remaining specimens exhibited a linear response to the tensile load and had a gradient (E_1) that was approximately similar (97 % similarity). The obtained value was within 10% of the value in the FE material library.

Figure 3-11 shows the test results of the UD material at 90 degrees (specimens 12 and 13). The tested specimens failed at low load, as expected. The measurements of specimens 12 and

13 appear to contain more noise than the previous specimens. Despite the observed noise, the determined gradient (E_1) was found to be within 10 % of the value in the FE material library.

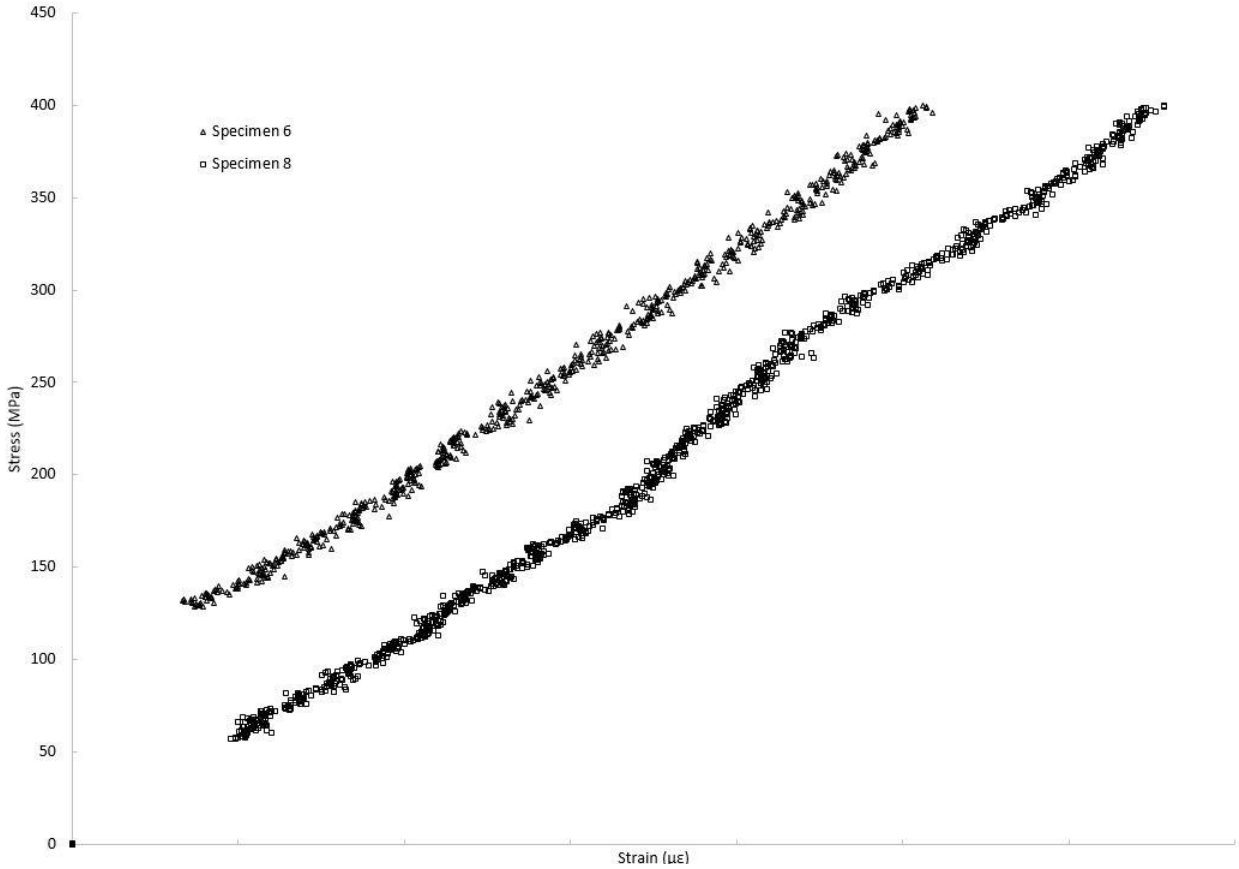


Figure 3-10 Tensile Testing results of the UD material at 0 degrees

The specimens were cut to the recommended widths obtained from the tensile testing standard. The UD (0^o) specimens had a width of 15 mm, while the remaining specimens had a width of 25 mm. This reduced width was thought to contribute to the slippage of specimens 7, 9 and 10. It must be noted that the tensile testing was conducted to broadly investigate the accuracy of the material properties in the FE material database. It was noted that future testing of the UD material should be conducted using a wider test specimen to avoid slippage.

The apparent stress at zero strain can be attributed to two factors. Firstly, the displacement of the specimen was small in relation to the displacement of the crosshead. This caused a substantial amount of noise in the measurement of the distance between tabs. Secondly, the laser extensometer was affected by a large amount of noise. While the time average of the displacement is deemed accurate, the composition of the test specimens was not ideal for use

of this method. Future material testing should be conducted by placing strain gauges on the material specimens. As the material testing was conducted to broadly determine the accuracy of the available material properties, and as this study aims to develop a methodology of developing a CFRP wheel, this method was deemed suitable for its purpose.

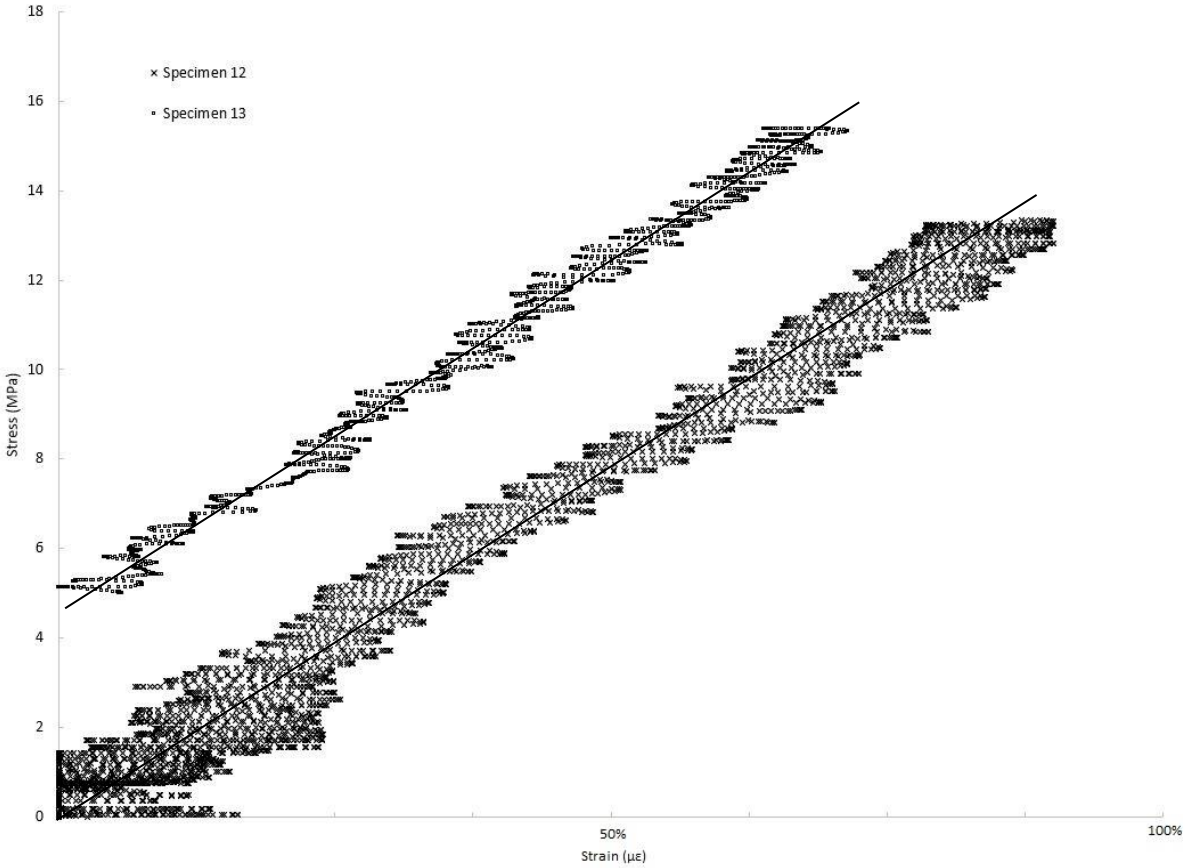


Figure 3-11 Tensile testing results of the UD material at 90 degrees

Table 3-4 contains the dimensions of the test specimens used for material testing. It was noted that the average thickness of the UD material with fibres orientated at 90° was noticeably lower than that of the UD material with fibres orientated at 0°. Both test plates used the same number of plies and were simultaneously manufactured. It was observed that the test plates with a 90° fibre orientation experienced more outward resin flow than the test plates with a 0° fibre orientation. It is known that resin flow in a UD prepreg is along the length of the fibres due to the tight packing of near identically oriented circular fibres. Figure 3-12 illustrates the cross-section of UD fibres orientated in the same direction subject to an external pressure and heat input (Q_{in}). Under the conditions shown, the resulting low viscosity of the resin (due to the temperature increase) and the pressure cause the resin to flow outward in the gaps between the fibres. As the rectangular test plates with a 90° fibre orientation have short fibres running along the width of the plate (as opposed to along the length), an equal pressure

resulted in more resin flow. It was thought that the same effect could be expected locally on the CFRP wheel in locations that have an increased internal pressure within the mould.

This assumption justified further investigation into the laminate. A calculation was performed to determine the estimated thickness of the wall of the spoke. The thicknesses were estimated using a per-layer thickness as determined from Table 3-4. This thickness estimate had proven to be accurate in some parts of the wheel, such as the central hub face of the wheel, where a known number of layers were at a pre-determined distance from one another. The estimated thickness of the spoke was compared to a digital measurement obtained from the wheel when scanned using a Vetorix Computed Tomography (CT) scanner in the testing facility at BST. The CT scanner allowed for a non-destructive inspection of a wheel taken from the production line. The measured wall thickness was found to be approximately 10 % thinner than the estimated value. The wall thicknesses and image of the spoke are not included in this study for proprietary reasons.

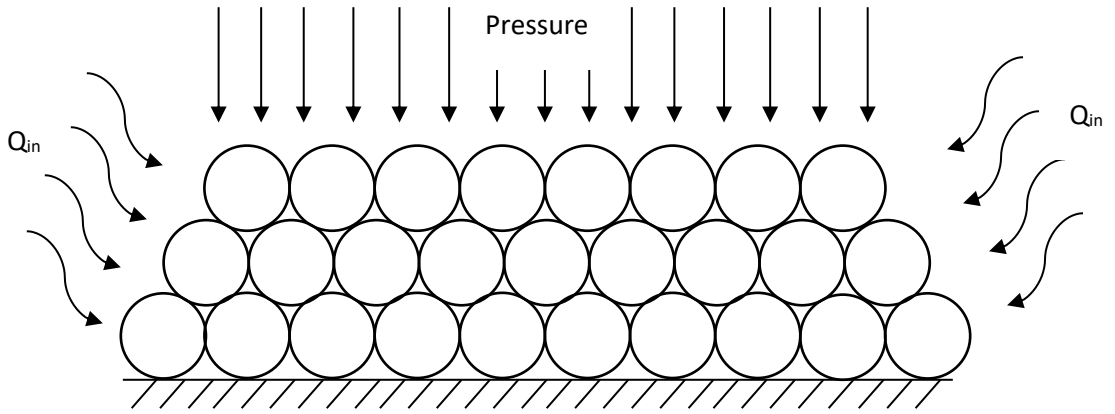


Figure 3-12 Cross-sectional illustration of UD fibres subject to external pressure during the manufacturing process

3.7. Summary

This chapter detailed the experimental work conducted on the CFRP wheel. A bending stiffness test was conducted on the prototype wheel. The prototype wheel was instrumented with Kyowa KFRP-5-350-C1-1 strain gauges that were placed on the outer surface of the wheel on the spokes. The strains were recorded during the bending stiffness test to allow for comparison to numerical values obtained from a composite FE model. The bending stiffness test was conducted before the wheel was tested on a dynamic cornering fatigue test rig. The prototype wheel achieved the required number of cycles in the DCF test as required by TÜV No. 287 30 StVZO without a substantial reduction in stiffness.

A bending stiffness test was chosen to validate a composite FE model by comparing simulated values to those obtained in the experiment. A bending stiffness test approximates an equivalent static load case of the DCF test. The wheel movement in the DCF test is small and thus the corresponding inertial forces are insignificant (justifying the use of an equivalent static load approximation).

In addition to the bending stiffness test, a tensile test was conducted on the carbon fabrics used in the wheel. The tensile tests were conducted to give an indication of the accuracy of the material database of the FE software. The stiffness of the fabrics used in the CFRP wheel were found to be within 10 % of the stated values in the FE materials database. The maximum allowable stresses in compression and tension were provided by the material supplier for woven and unidirectional materials. The provided values were stated to have been based on a fibre volume fraction of 60 %. The obtained stiffnesses were later used in the composite FE model.

The work in this chapter forms part of the requirement to achieve the first stated objective as set out in Section 1.3. As the wheel that was used for this study successfully completed the required number of cycles on the dynamic cornering fatigue test rig, the wheel can be used to further refine the design process of a CFRP wheel.

4. NUMERICAL MODEL OF THE CARBON LAMINATE

This chapter details the development of the composite FE model of the CFRP wheel used for this study. The development process of the laminate of the physical prototype wheel is also detailed. The composite FE model was used to simulate the response of the wheel to the loading conditions of the bending stiffness test. The bending stiffness test serves as a static approximation of the response during the dynamic cornering fatigue test. The numerical data obtained from the composite FE simulation was compared to the experimental data that was presented in Section 3.4 and was used to justify the validity of the composite FE model. The stresses experienced by the individual plies were analysed and are presented here.

4.1. Development of the Laminate

Using the improved wheel shape shown in Section 2.1.6, a mould was manufactured and used to create the first prototype laminate. This section describes how the laminate of the first prototype was developed.

It is important to note that the laminate of the 10-spoke car wheel used for this study was not the first CFRP wheel developed for the automotive industry, nor was it the first CFRP wheel made by BST. The laminate was developed with the experience gained over 15 years. The challenge when developing the laminate of this wheel, however, was that the required loads (as a function of the static load rating) were a step higher than those of the existing motorcycle wheels, as well as the wheel that was developed for the Vuhl 05RR[4] (see Figure 1-2).

Before the laminate of the wheel can be developed, the required vehicle specifications must be determined. The maximum static load rating of the wheel is determined from the gross vehicle mass (GVM) and the vehicle weight distribution. The vehicle loads for the wheel used in this study assumed that the vehicle would use semi-slick tyres, with a significantly higher coefficient of friction than the standard value prescribed by the TÜV standard.

Two material types were available for use in the wheel. Material type A was a plain woven prepreg material. Material type B was a unidirectional (UD) prepreg material. It is important to note that neither material can be used successfully to develop a laminate on their own.

[4] The style of the Vuhl wheel was prescribed by the client, and thus the wheel in this study was the first aftermarket automotive wheel developed by BST

While the unidirectional material has a significantly higher stiffness along the length of the fibres, it is not suitable for load in other directions. The woven material, on the other hand, has a lower stiffness along the primary axes, but it more suitable to resist torsional loads. In addition, the woven material is used to transfer the loads from the structure of the spokes to the rest of the wheel.

As the shape of the wheel had been fixed after the mould had been manufactured, a laminate had to be developed within the shape limitations of the mould. The wheel design chosen had a solid central hub face with a pre-determined spacing. The mould face could not be altered to accommodate alterations to the laminate, and thus the central face was required to be filled with material. Based on the required loads of the vehicle and the internal knowledge of the manufacturer (BST), a laminate was developed with the intention of achieving a specific wall thickness. It was crucial at this stage to balance the amount of UD layers to the number of layers of woven material. As the wheel successfully passed the DCF test as specified by TÜV, it was known that the laminate of this wheel was sufficiently capable. It is, however, not known if the laminate was over designed.

The first prototype CFRP wheel had a combined mass of 6.8 kg. The improved wheel that entered production (with the improved hubs) had a mass of 6.4 kg. Understanding the physical response of the wheel to applied loads is crucial to determine whether there are any further weight savings that can be achieved. The first prototype wheel had achieved a weight saving over the standard aluminium wheel on the Donkervoort. Both wheels have the same load rating. The standard wheel has a mass of 8.1 kg. This resulted in a 21 % weight saving on the wheel. The numerical model aims to investigate the possibility of further weight savings.

4.2. Composite Finite Element Model

This section details the development of a composite FE model to simulate the mechanical properties of the composite wheel.

4.2.1. Modelling process

When modelling a composite structure, a 3-dimensional surface body is required. Carbon materials are usually supplied in thin sheets that are rolled on tubes. In some cases, the material is pre-impregnated with an epoxy resin (prepreg). The prepreg material is cut in specific shapes (plies) to fit pre-defined surfaces of the mould. When building a composite

model in a FE software package, this process is replicated. To allow for the plies to vary in shape, a surface model with many lines must be created. This allows the user to select a combination of small surfaces to define an area for a ply. The surface model used for this composite model is shown in Figure 4-1.

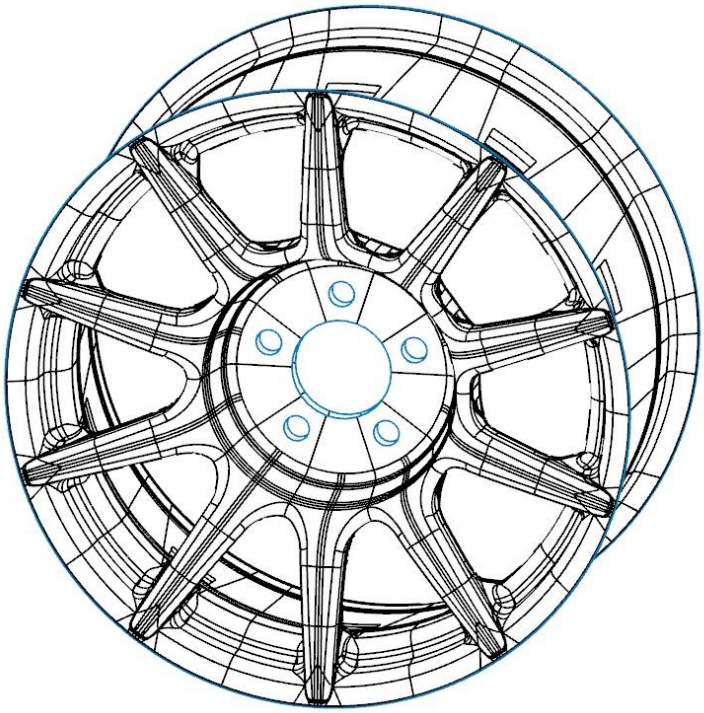


Figure 4-1 Surface model of the experimental prototype wheel

The surface model was saved as a Parasolid and imported into ANSYS using ACP(Pre) (block A). Figure 4-2 shows the workbench environment in ANSYS for composite modelling. In block A, the user defines the material properties of the fabrics that will be used. In line 4 of block A the user creates the mesh that will be used in the simulation. In line 5 of block A the user creates the fabrics that will be used, defines the layup areas, fibre direction and defines the layup sequence of the model. Only a single body can be created in block A. If the model requires multiple carbon pieces, additional ACP(Pre) blocks must be used. The bodies are then exported from block A to a liner static structural simulation (block B). The composite model can either be exported as shell elements or as a solid[5]. In block B the user defines the loads and constraints. Block B allows for some limited post processing to be performed on the

[5] Assemblies of multiple carbon pieces require the creation of solid models

model. Total deformation and strain values can be read in block B. ACP(Post) (block C) is used for detailed post processing of the laminate.

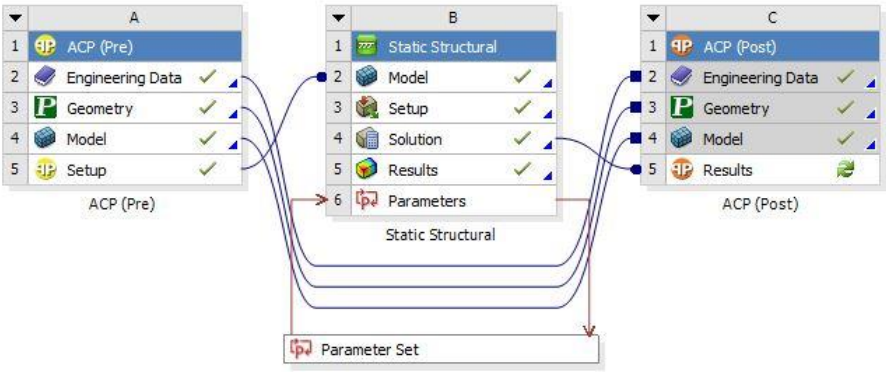


Figure 4-2 ANSYS workbench environment for composite modelling

4.2.2. Surface meshing and surface naming

The surface geometry of the wheel was discretised into a mesh as shown in Figure 4-3. As with the mesh generated for the isotropic model in Section 2.1.3, the standard element size selected for the wheel was 5 mm. As the composite model of the wheel requires boundary lines to define the edges of a ply in the laminate, surfaces could not be combined as effectively as with the isotropic model. An unforeseen consequence of this was that there were small surfaces present on the surface body. The mesh was generated using triangular element method. As with the isotropic model, it was discovered that the shape of the surface of the wheel was sufficiently complex, such that the FE software was unable to resolve a quadrilateral element mesh on all surfaces. A mesh was generated using triangular elements with mid-side nodes.

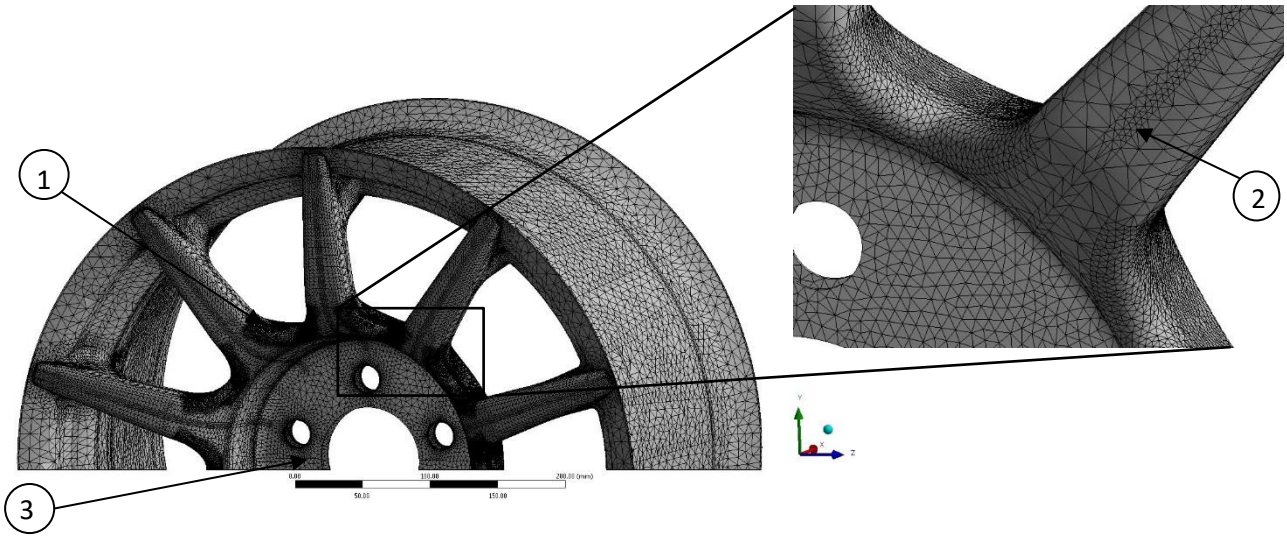


Figure 4-3 Mesh used in the composite model

The mesh used had 142 411 elements with 290 152 nodes. The mesh was generated using a six-node triangular element (TRI6). The mesh had an average quality of 0.88. The quality of an element is defined as the ratio of the volume to the edge length on a scale of 1 (perfect) to 0 (poor). Areas that were of interest are numbered in Figure 4-3. An element size of 1 mm was applied at points 1 and 2. An element size of 2 mm was applied on the hub surface at point 3. An element size of 4 mm was applied to the reverse side of the spokes.

To define the layup area of a ply, named selections were defined. Surfaces were selected in the required combinations to closely approximate the positioning of each ply type. Figure 4-4 shows an example of a named selection used to define a ply area. The selected surfaces were not able to perfectly replicate the shape of the plies used in the physical prototype but were found to be a close enough approximation. Alternate ply shapes were also included to allow for the possibility of modelling modified ply shapes.

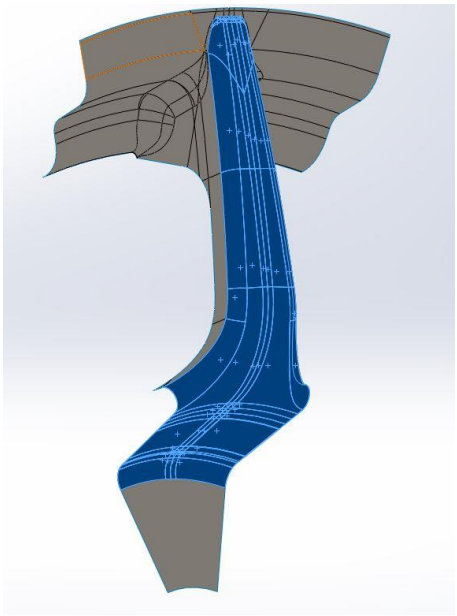


Figure 4-4 Example of a ply area to define the layup of a spoke ply

4.2.3. Laminate generation

The laminate was replicated in the composite modeller of the FE software. The process of generating a laminate in the FE software is a multi-step process. The steps required are:

1. Define fabrics to be used
2. Define fibre reference directions
3. Define layup directions
4. Create individual plies in sequence to define layup of the laminate

Unlike isotropic materials such as aluminium and steel, it is not easy to determine the material properties of a prepreg carbon fibre fabric by referring to a material data sheet. Carbon fibre component manufacturers work closely with material suppliers to create tailor made materials for a specific purpose. There are many variables when defining a CFRP fabric, including orthotropic elasticity, ply type, orthotropic stress limits and orthotropic strain limits. The most significant variable is the fibre stiffness, which determines the maximum stiffness of the fabric in the axial direction. There are, however, less obvious variables that have an impact on the material properties, such as the type of weave, resin quantity and the chemical composition of the resin. These properties cause a reduction in overall stiffness of the laminae. The magnitude of the reduction cannot be calculated easily and is preferably measured experimentally (See Section 3.6).

Due to this complexity, the pre-defined materials in the ANSYS Engineering Data section were selected and modified to use the directional stiffnesses determined during from the material testing. An Epoxy Carbon UD Prepreg and Epoxy Carbon Woven Prepreg were selected to define fabrics designated. When defining a fabric in the FE software, a thickness and material type were combined. An estimate of the fabric thickness was obtained experimentally as described in Section 3.6.

Fibre reference directions were defined using local coordinate systems positioned on the surface of the geometrical model in the FE software. The x-axis of the coordinate system is used to define the fibre reference direction. The x-axis is orientated using edges of the surface body to ensure that the rosette is consistent when modelling surface bodies with repeating patterns. Figure 4-5 shows a local coordinate system used to define the fibre reference direction on the side of a spoke. Coordinate systems were placed on all sides of each spoke, between each spoke on the rim contour, on the central hub face and on the rim contour itself.

The named surfaces and local coordinate systems were combined in the FE software in an oriented selection set (OSS). The OSS combines the named surfaces for each ply, local coordinate systems and an individually selected surface normal to generate each placement type. Care was taken to define the fibre reference direction of each laminae accounting for the draping of material over complex geometry. Figure 4-6 (a) shows the default fibre reference direction generated by the FE software; which does not represent the true fibre

direction. Figure 4-6 (b) shows the fibre reference direction after the draping function of the OSS within the FE software was utilised. While this is not a true representation of the fibre direction, it serves as a close approximation. The OSSs were used with an individual fibre

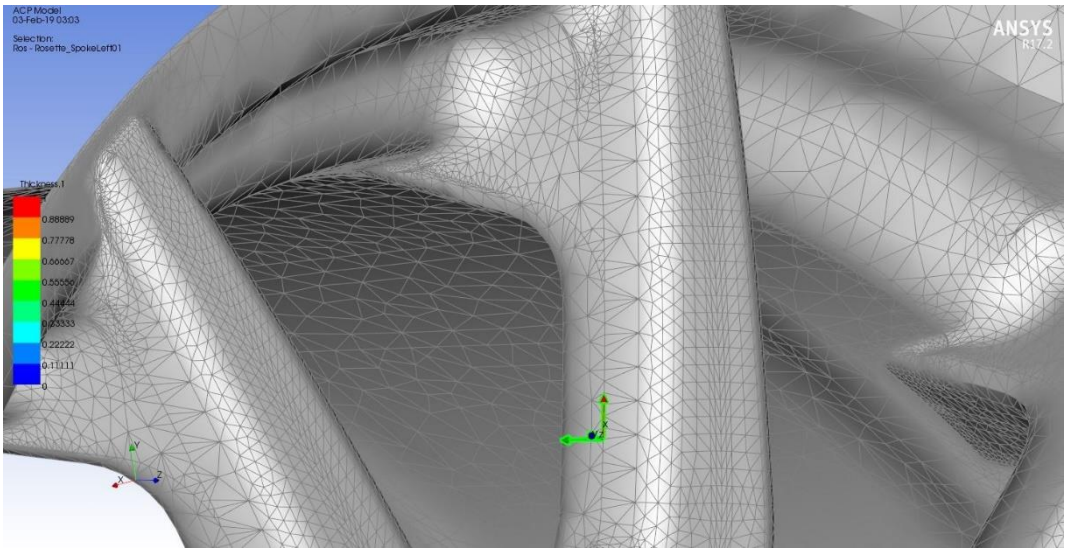


Figure 4-5 Rosette used for definition of fibre reference direction

orientation to specify the layup of each ply in the laminate of the experimental wheel.

The laminate was constructed using a twill weave prepreg fabric (cosmetic), a plain weave prepreg fabric and a UD prepreg fabric. The first woven material on the wheel was purely a cosmetic layer. The cosmetic material is lighter but significantly more expensive than the other woven or UD fabrics. Thereafter the non-cosmetic woven and UD fabrics were alternated. The UD material was oriented with fibres in line with the spoke, and the woven material was oriented with fibres at 45^{o} to the spoke. Each additional layer improves the strength and stiffness of the spoke at the expense of additional mass.

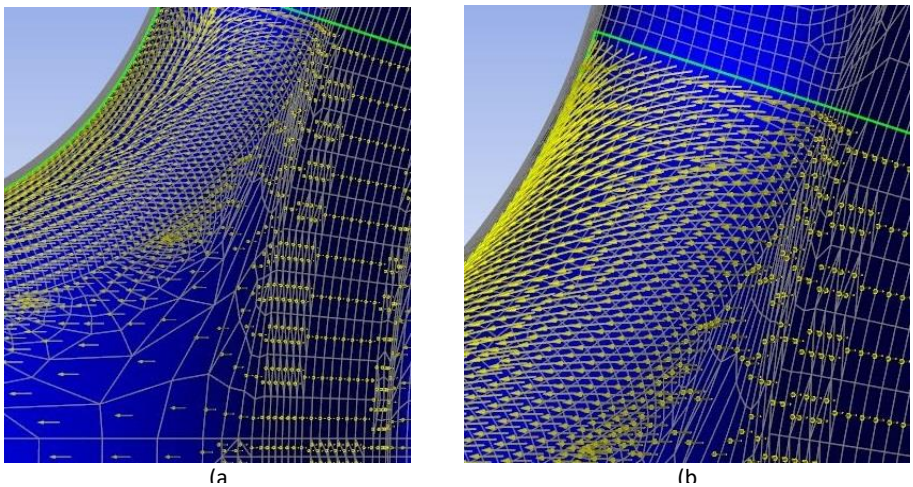


Figure 4-6 (a) Fibre reference direction of a ply before draping; (b) fibre reference direction after draping

4.2.4. Test setup

The ACP(Pre) model was exported as a shell body to the linear static structural environment. Generating a solid model was unsuccessful due to the large number of elements and the complex geometry of the surface body. Generating a software model of a composite wheel is sufficiently complex, that limitations in the use case of the composite FE software may exist. The decision was made to investigate the validity of a simulated DCF test using a surface body. Appendix A investigates the validity of FE calculations and compares the results of solid and surface bodies.

The applied loads and constraints were modelled to replicate the experimental conditions described in Section 3.1. The load was simulated using a remote force that was applied to the central face of the surface model with an effective distance matching the load arm used in the physical tests. The wheel was constrained using a fixed support on the edge of the inner rim lip illustrated in Figure 2-4. The applied loads in the simulated model were chosen to match the applied loads in the physical tests.

Surface probes were placed on the surface body of the modelled wheel to match the location of strain gauges that were used in the physical experiments, as detailed in Section 3.2. A surface probe is an output of the calculated solution that is programmed within the FE software to display solution information of a desired type. The probes that were placed on the surface of the spokes were programmed to output the simulated strain at that specific point on the surface at the end of the simulation. The value of strain was output for comparison to the experimentally obtained strains as detailed in Section 3.4. In addition to the probes on the surface of the spokes, a probe was placed on the rim lip to match the position of the secondary dial gauge used in the experiment. The position of the dial gauge is shown in Figure 3-1.

As stated in Section 3.2, the strain gauges were observed to have slight misalignment from the centreline of the spoke. Gauge G3 was observed to be well aligned. The orientation of the gauges G1, G2, and G4 in the FE model were adjusted to compensate for the misalignment when gluing the gauges on the complex geometry of the wheel. Figure 4-7 shows the corrected orientation of the gauges in the FE model.

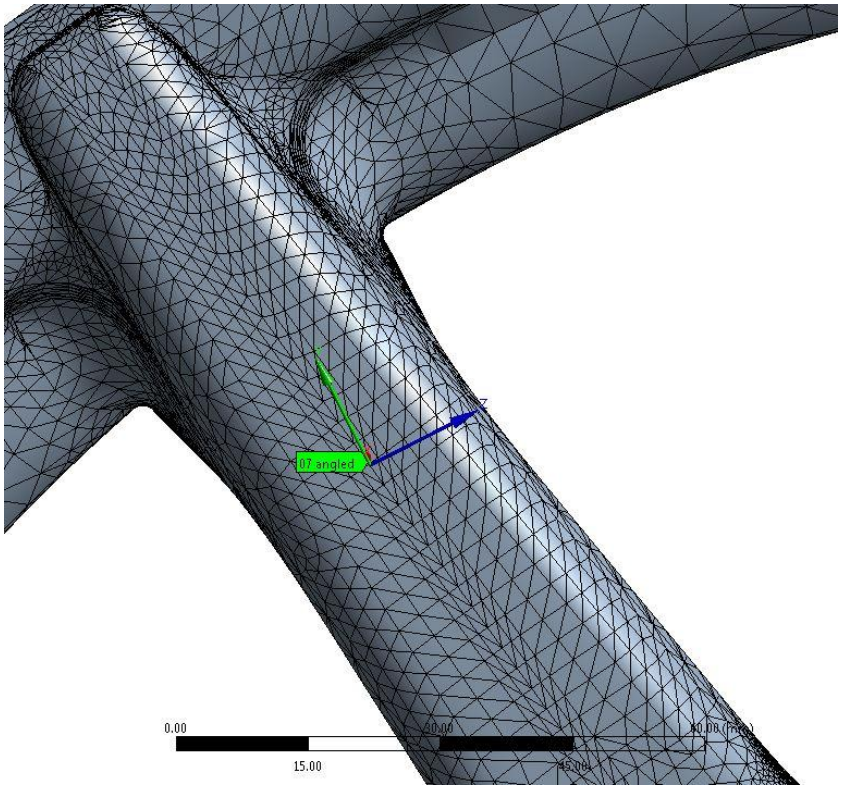


Figure 4-7 Angled gauge used for the strain probe in the composite FE model

4.3. Comparison to the Physical Wheel

Figure 4-8 shows the measured strains of gauges G1 to G4 versus an increase in applied load on the bending stiffness apparatus, as well as the corresponding FE results for the gauge positions. The differences in measured strain of ±2 $\mu\varepsilon$ between incremental loading and unloading indicate a small amount of hysteresis present in all measurements. The experimentally measured strain values and those determined from the FE model increase linearly as expected. It was expected to obtain similar readings between gauges G1 and G2; as well as G3 and G4. However, notably different strains in gauges between G1 and G2; as well G3 and G4 were observed. As stated in Section 3.2, the strain gauges were observed to have slight misalignment from the centreline of the spoke. It was noted that the gauges that were misaligned at an angle closer to that of the applied load had a higher measured strain. The opposite was observed when gauges were misaligned away from the applied load. Gauge G3 was observed to be well aligned and in good agreement with the FE model. The orientation of the gauges G1, G2, and G4 in the FE model were adjusted 5^{o} to compensate for the misalignment when attaching the gauges on the complex geometry of the wheel. The gauge

G3 was well-aligned. The simulated strains show acceptable agreement with the measured values.

To achieve the simulated strains presented, the axial stiffness of the UD fabric was slightly increased. The stiffness of the fabric that was originally used in the simulation predicted a larger deflection, and thus larger strains than were measured experimentally. This action was seemingly justified, given the observation of the decreased thickness due to increased resin flow from the UD test specimens, and the measured thickness of the spoke of the wheel. The stiffness of the laminae required to achieve the simulated response was well below the maximum stiffness of the fibres in the resin. The simulated strains prior to the correction of the orientation of the gauges show good agreement the gauge G3. The theoretically simulated strain of the gauges G1 and G2 was also seen to lie central to the values obtained for the gauges G1 and G2.

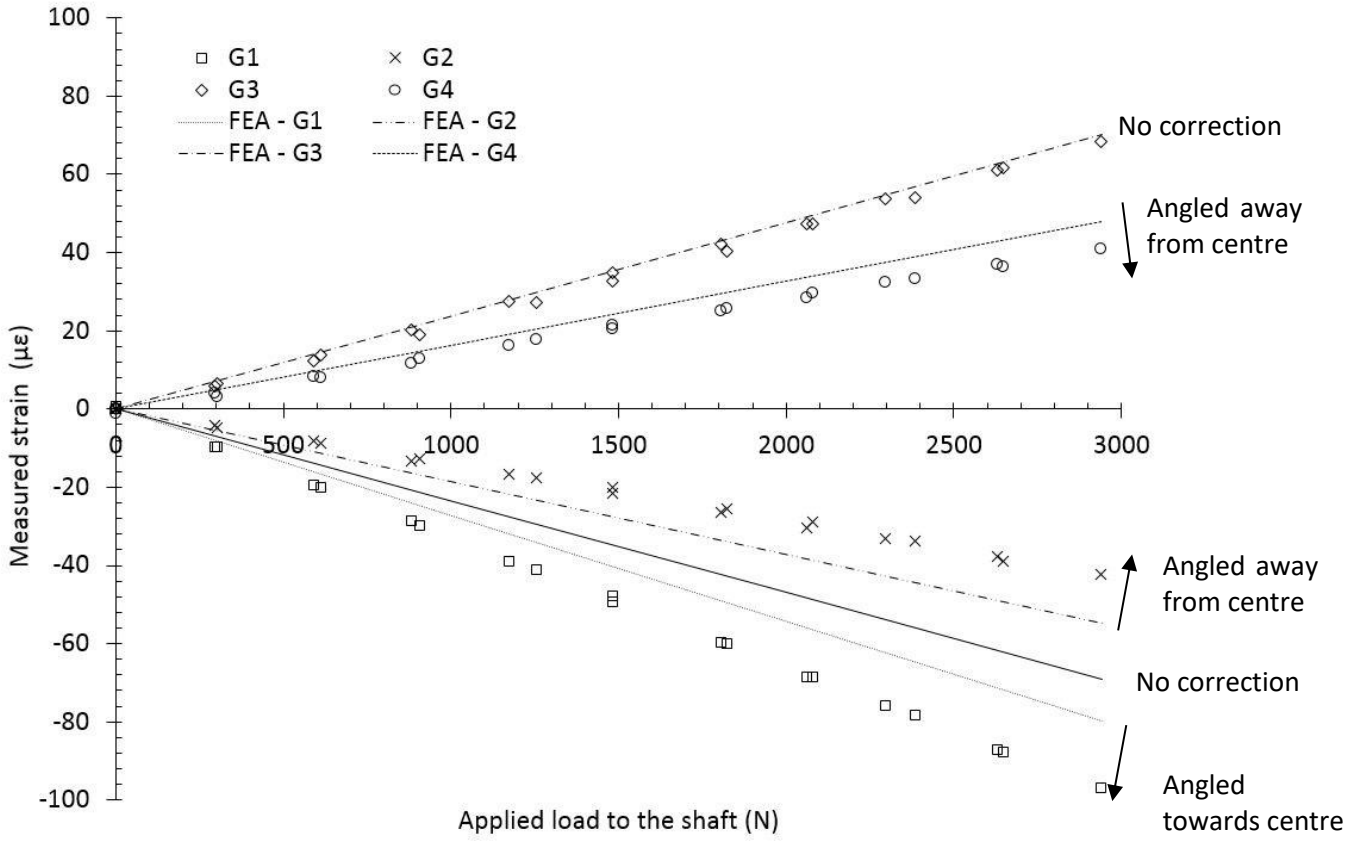


Figure 4-8 Measured strains on the spokes compared to the FE results

A further point of comparison was added to the numerical model to investigate agreement. In addition to the measured values obtained from the strain gauges, the deflection of the edge of the rim of the wheel was measured. This deflection was also simulated in the composite FE model. Figure 4-9 shows the comparison of the simulated and measured deflection of the rim edge. The simulated deflection increases linearly as expected. The experimental deflection shows good agreement with the simulated values for most of the applied load. The difference in deflection of approximately 0.03 mm can be attributed to the sliding of the wheel during the bending stiffness test.

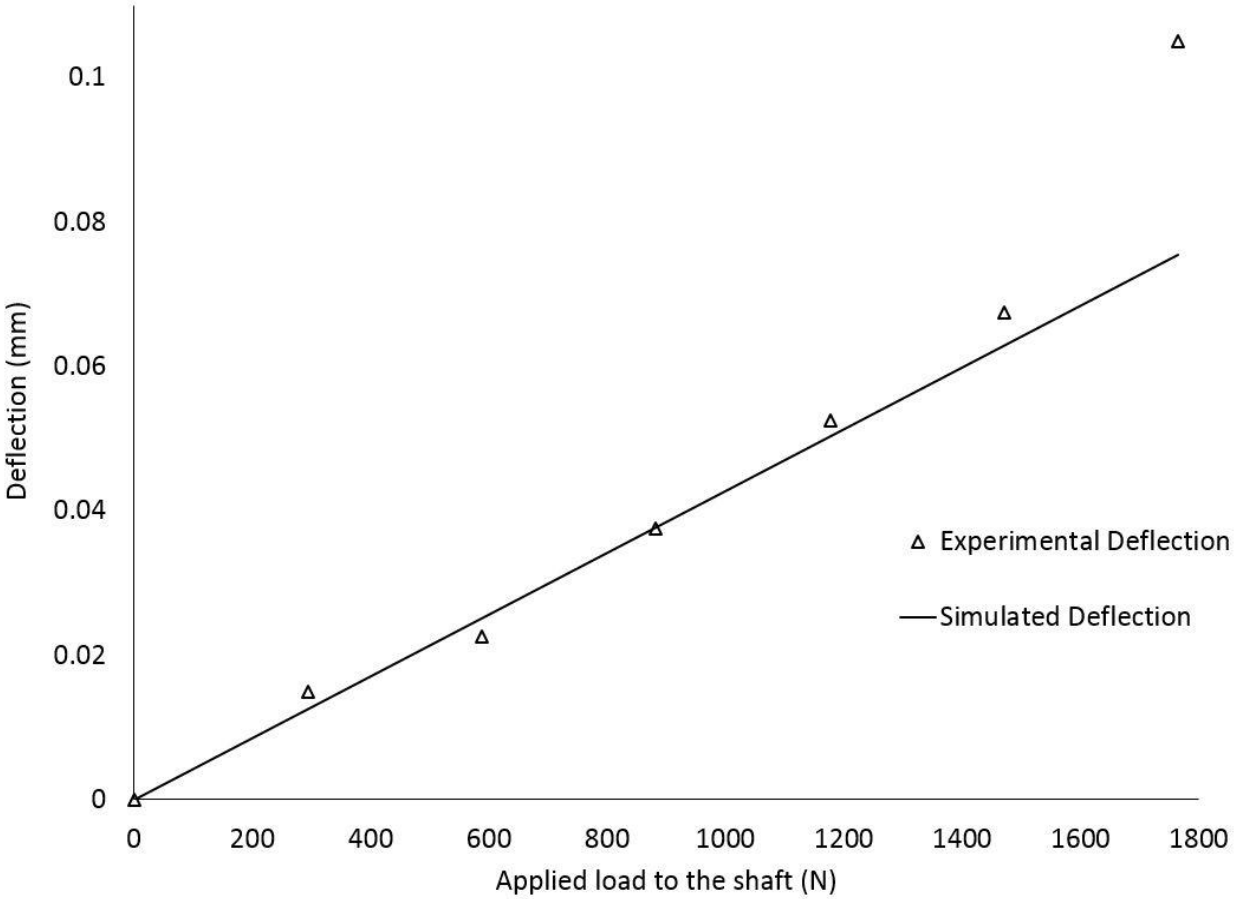


Figure 4-9 Comparison of the simulated deflection to the deflection of the edge of the rim

As the wheel was simulated as a surface model the measured deflection of the load arm deflection could not be compared. It was assumed that the load arm was sufficiently stiff to be considered rigid in the FE simulation.

4.4. Stress Analysis of the Wheel

On the basis of the experimental validation of the composite FE model, the simulation was analysed in detail to determine whether any further weight saving was possible from the laminate. The composite FE simulation had been set up after the wheel had passed the required number of loads on the DCF test rig and the wheel had entered production.

The laminate of the simulated wheel was analysed after the experimental data had shown good agreement with the values obtained from the simulation. The maximum DCF test load as specified by TÜV was simulated. The stresses of the wheel were analysed for the simulated load case. The maximum allowable stress values that were obtained from the carbon material supplier were used for the stress analysis. In the absence of fabric specific fatigue curves (S-N curves), an approximate stress limit was used to analyse the laminate. The fatigue stress limit of the material was assumed to be one third of the static (unfatigued) stress limit. This value was based on S-N curves of curves found for CFRP materials in literature [40]. This value was intended to serve as a variable in the analysis until such time that an appropriate S-N curve can be generated, or a fatigue stress limit is obtained for the fabrics used. Table 4-1 shows the stresses that were obtained from the FE simulation during post processing. The locations that were investigated are shown in Figure 4-10. As with the Isotropic simulation, the DCF load was applied at 20 discrete points on the wheel. The stresses of the individual plies were recorded and the highest recorded load on each is displayed in terms of the static stress limit of the wheel.

Table 4-1 Post-processed stresses on the wheel (as percentage of static stress limit)

Location	Number	Stress
Outer hub (woven)	1	33 %
Spoke centre (woven)	2	15 %
Spoke centre (UD)	2	10 %
Spoke side (woven)	3	37 %
Inner hub (woven)	4	21 %
Inner spoke (woven)	5	17 %
Inner spoke (UD)	5	16 %

From the table it can be seen that some of the plies experience loads that are equal to or greater than the assumed fatigue limit (i.e. equal to or greater than 33 % of the static stress limit. It is known that the presented laminate passed the required DCF loads, and thus a fatigue stress limit of the wheel of approximately 40 % the static stress limit seems possible.

As the stiffness of the prototype wheel was desired by the client for the enhanced dynamic characteristics, it can be stated that material cannot easily be removed.

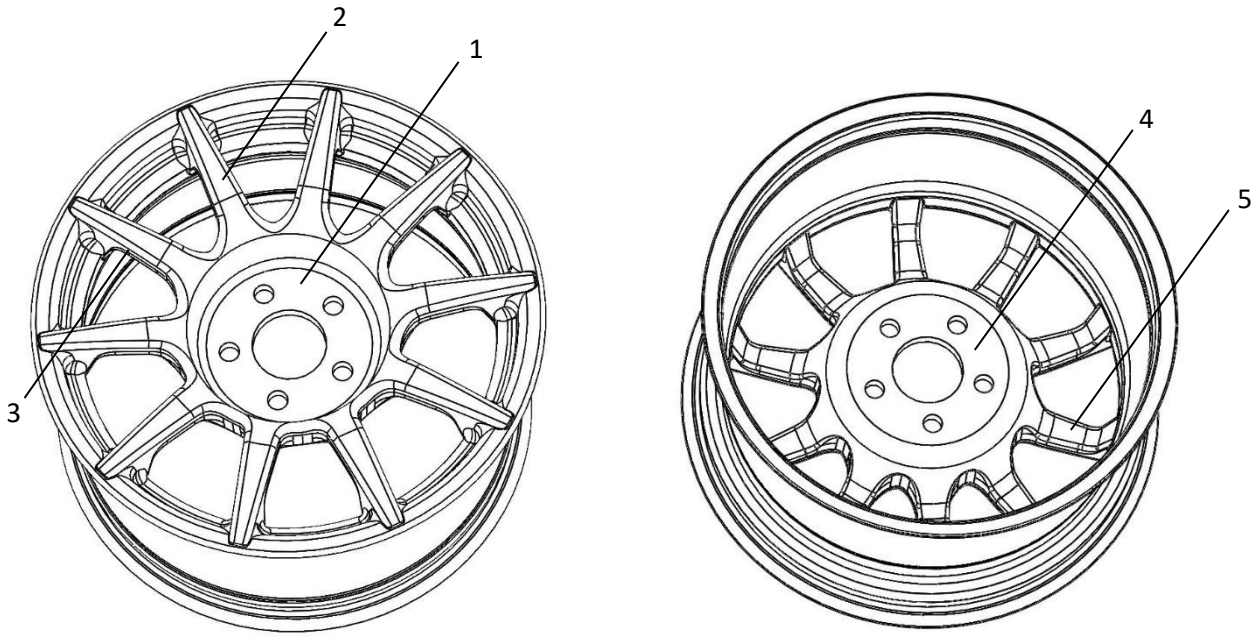


Figure 4-10 Locations probed for maximum stresses during post processing

As the stiffness of the wheel is heavily dependent on the stiffness of the spokes, these are the centre of focus. It would appear that the potential for weight reduction of this wheel is limited by the physical geometry of the spokes. Figure 4-11 shows the cross section of the spoke of the prototype wheel. The weight saving potential of future CFRP wheels would benefit greatly from the use of larger spoke sections, as the resistance to bending of tubular sections increases with greater distance from the neutral axis.

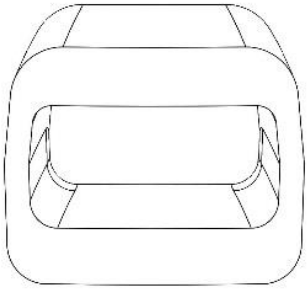


Figure 4-11 Cross-section of a spoke of the prototype wheel

The complex setup of the composite FE model developed for this study limits the number of configurations that can be investigated without having to rebuild the laminate. The accuracy

of a composite FE model is limited as the physical definition of the laminate is an approximation. The following approximations and potential sources of error were identified:

- The exact shape of an individual ply is an approximation. The complex shape of a 2-dimensional ply draped on a 3-dimensional surface can only be estimated.
- The amount of overlap can only be estimated.
- A draping function must be used to approximate the fibre reference direction on complex geometry (see Figure 4-6).
- Some of the aspects of the manufacturing process cannot be replicated in the construction of the composite FE model. The ETRTO regulated profile of the pressurised side of the wheel rim cannot be precisely modelled.
- The FE model assumes that the manufacturing process is free of defects, such as the presence of voids or variability of the intended fibre direction.
- The thickness of the same number of layers of prepreg material can vary.
- Pockets of resin that are not reinforced cannot be modelled using a surface body.
- The definition of the material properties of each fabric used is critical.

Further investigation is required to determine the impact of environmental conditions on the material properties of the fabrics used. Despite the above potential sources of error and approximations, the model developed in this study can be a powerful tool in the development process of a composite component. The manufacturing of prototype laminates remains expensive, even for prototypes manufactured from an identical tool. Multiple laminate configurations could be investigated without the need for the manufacture of physical prototypes. When combined with the experience gained from existing projects of a composite component manufacturer, a composite FE model can be invaluable. The composite FE model presented can be used to estimate the mechanical properties of a laminate before a prototype is manufactured. The internal structure of the laminate can be visualised.

The prototype wheel that was manufactured for the client had a reduction in mass of 21 % over the original aluminium wheels. This was achieved despite the lack of insight into the behaviour of the laminate and the wheel prior to the manufacture of the prototype wheel.

4.5. Summary

This chapter detailed the work conducted to develop a numerical model of the composite wheel. The development of the laminate used in the production wheel was explained. The laminate was developed using the experience that had been gained over many years of production. The challenge faced when developing this laminate was the higher loads that were expected on the intended vehicle. As it was known that the CFRP wheel had passed the required loads as set out by TÜV No. 287 30 StVZO, the laminate could be used to understand how a composite FE model could be used to further improve the process.

The laminate of the production wheel was replicated in a composite FE software package. A surface body of the wheel was generated in a CAD software package. The surface body is required to have sufficient edges (curves, lines, arcs or splines) as to define the edges of all of the plies that could be used in a simulated laminate. The applied loads and constraints were modelled to replicate the experimental conditions described in Section 3.1. The software was programmed to output the strains on the surface of the spokes to match the locations of the strain gauges used in the experiment. The simulated strains were compared to the strains obtained during the experiment and showed good agreement. Further, the displacement of the edge of the rim was output from the simulation and compared to the values obtained during the experiment. The displacement of the rim also showed good agreement.

The composite FE model that was developed in this study is not intended to fully replace the testing process to certify a wheel. The composite model was developed with the intention of having a tool that could indicate whether one laminate has superior properties over another. The analysis of the developed wheel will help aid in understanding the usefulness of this composite model.

The work in this chapter was conducted to fulfil the requirement of the second stated objective as set out in Section 1.3. This chapter showed that the mechanical response of a composite FE wheel to applied loads can be replicated in software. The numerical model of the composite wheel was seen to be validated at the conclusion of this chapter.

On the basis of the experimental validation of the composite FE model, the simulation was analysed in detail to determine whether any further weight saving was possible from the laminate. A stress analysis of the plies showed that further weight reduction by means of

removing a layer of material was not easily achievable. The physical geometry of the wheel is limited by the shape of the mould that was manufactured. Future wheels that are developed would benefit greatly from larger spoke sections that can more efficiently use the higher stiffness and fatigue stress limit of the material.

5. THERMAL TESTING OF THE CFRP WHEEL

This chapter details the experiment to determine the effect of temperature on the bending stiffness of a CFRP wheel. Section 1.2.4 details the build-up of heat in during braking under different braking modes. It is known that brake temperatures can rise to elevated levels (approximately 700 ^{o}C [29]) during use. The effect of heat on CFRP wheels is not well documented.

5.1. Wheel Specimen

A separate wheel specimen was manufactured for thermal testing. The wheel manufactured for thermal testing was a 17-inch wheel, with a 10-spoke configuration, and an identical laminate to the wheel used for the first part of this study. Figure 5-1 shows the wheel that was used for thermal testing. While there are some differences between the wheel developed in the first part of this study and the wheel in this chapter (the wheel has a four-bolt configuration and a different hub design), the mechanical response of the wheel under thermal loading was taken to be representative of CFRP wheels in general.



Figure 5-1 CAD model of the wheel used for thermal testing

5.2. Test Equipment

Figure 3-1 illustrates the bending stiffness rig. A force was applied to a load arm, which transferred a bending moment to the mounting face of the wheel. The deflection of the load arm was measured with a dial gauge at a measured distance. The dial gauge was mounted to the steel frame by means of a magnetic foot. The dial gauge had an uncertainty of ±0.005 mm. The applied force from the hydraulic actuator was measured in kgf using a load cell. The wheel was clamped down using 8 CNC step clamps and hex socket bolts. The actuator and load cell were connected to the load arm by means of a chain. The load arm remained attached to the wheel for the duration of the experiment. The wheel and load arm assembly were heated in an electric oven before each test. A white paint marker was used to draw an outline around the wheel. Lines were drawn on the wheel and plate surface to ensure accurate repositioning after the wheel assembly had been heated.

Four thermocouples were taped to the surface of the wheel during the experiment. Figure 5-2 shows the placement of the thermocouples on the wheel. The first thermocouple was placed on the outer surface of the hub area of the wheel between two of the wheel nuts. The probe was placed in line with a spoke. The second thermocouple was positioned on the outer surface in the centre of the spoke. The third thermocouple was placed on the centre of the barrel of the rim. The fourth thermocouple was used to record the ambient temperature. Table 5-1 lists the equipment used in the thermal experiment.

Table 5-1 List of equipment used for thermal testing

Item	Name	Quantity
Thermocouple	RS PRO Type K Thermocouple	4
Thermometer	RS PRO Digital Thermometer 2	2
Oven	Minimatic Specialised Bakery Oven	
Bending stiffness rig	BST Bending stiffness apparatus	

5.3. Test Procedure

Bending stiffness tests were conducted at room temperature and at the following nominal hub temperatures: 50 ^{o}C, 70 ^{o}C, 90 ^{o}C, 100 ^{o}C and 140 ^{o}C. Each successive increase in temperature was achieved by heating the wheel in an oven for 1-2 hours. The wheel was repositioned on the test rig after heating using the positioning markers. After completion of

the thermal testing the wheel was left to cool for 48 hours. A second bending stiffness test at ambient temperature was conducted on the wheel to determine whether the wheel experienced a permanent reduction in stiffness due to the elevated temperatures.

The wheel was loaded in 40 kg increments to a maximum load of 200 kg. The applied load was reduced in the same increments to provide more data points and to investigate hysteresis. Before the data was recorded, the wheel was twice loaded to the maximum and subsequently unloaded to remove possible slack in the system.

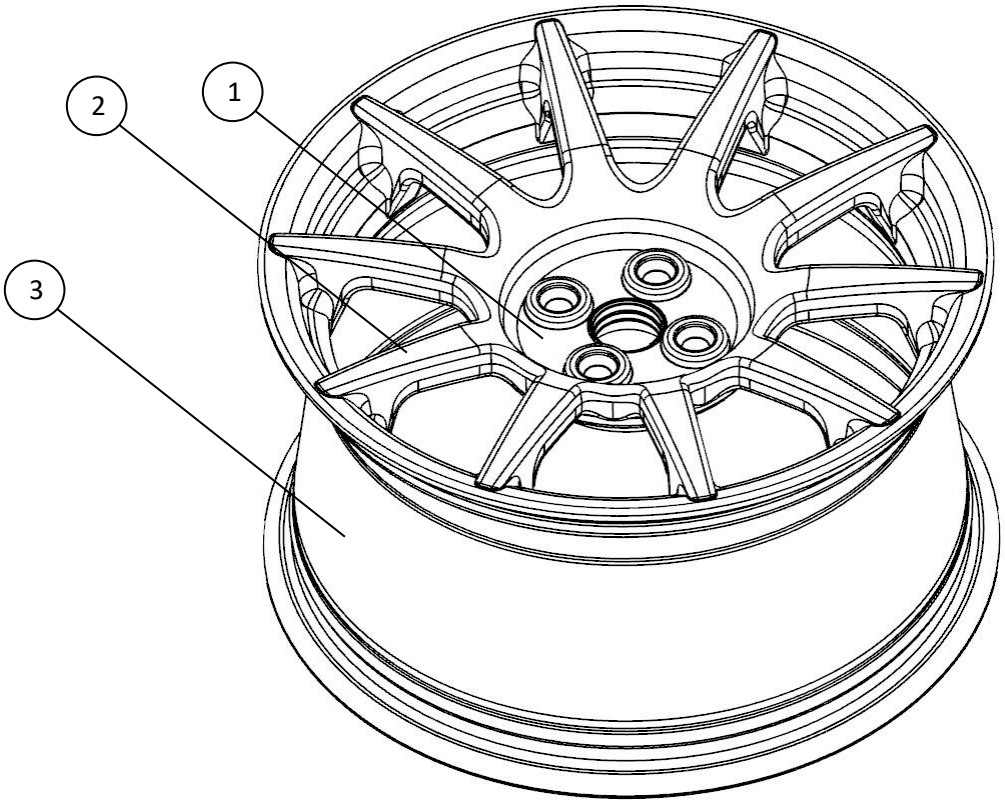


Figure 5-2 Thermocouple placement on the wheel

The bending stiffness (k_b) of the wheel was calculated by measuring the deflection of the load arm at the dial gauge position. The force applied to the load arm transferred a bending moment to the wheel. The angular deflection (θ) was calculated using the dial gauge distance and the deflection measured using the dial gauge. Figure 5-3 illustrates the determination of the bending stiffness. The bending stiffness of the wheel was determined using the formula:

$$\boldsymbol{k_b = \frac{F \times L}{\theta}} \qquad (\mathbf{12})$$

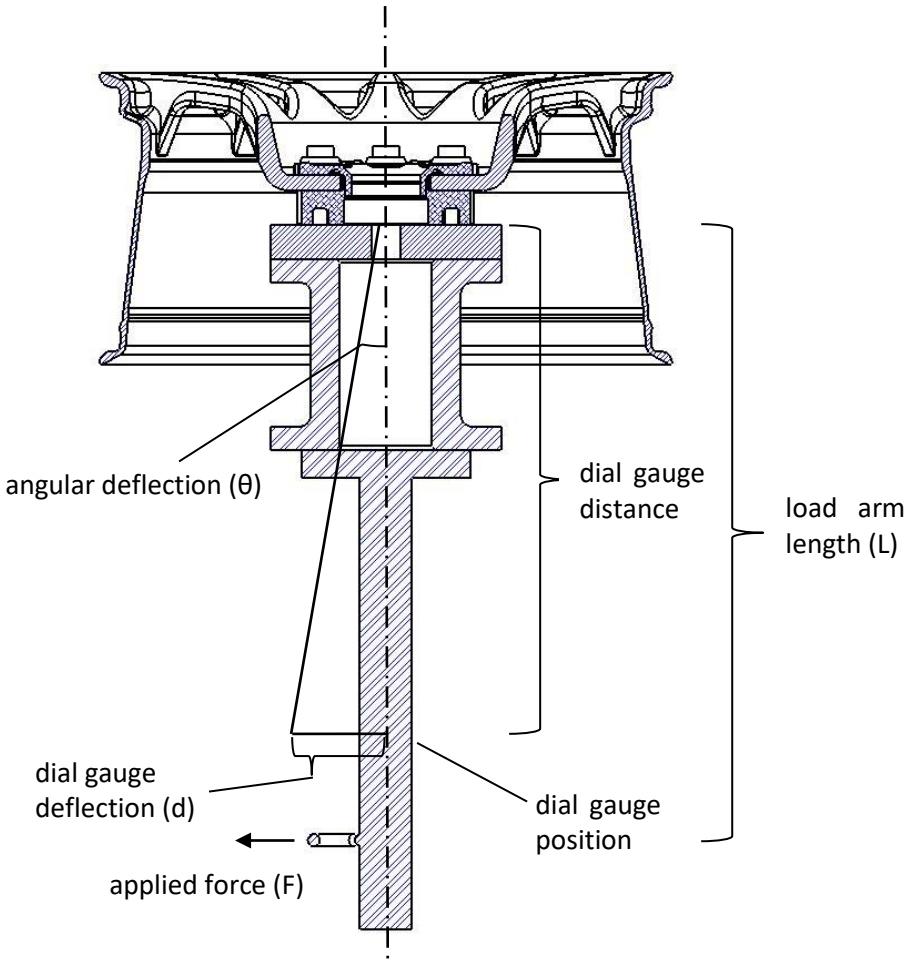


Figure 5-3 Illustration of a bending stiffness test

5.4. Results and Discussion of the Thermal Testing

5.4.1. Heat transfer to the wheel and temperatures

Brake rotors can reach bulk temperatures of approximately 700 °C [29]. The temperature distribution in wheels under these conditions is not known. The mechanisms of heat transfer from brake assemblies into CFRP wheels is the subject of a separate study under investigation at the University of the Witwatersrand at the time of this experiment. Figure 5-4 illustrates the methods of heat transfer from the brake assembly to a wheel. Heat is conducted from the brake assembly to the hub, the spokes and the rim barrel. The load arm was left attached to the wheel during heating and acted like a virtual hub assembly.

The temperatures of positions 1 and 2 were consistently higher than the temperature of position 3 at the start of each test. The temperature of position 3 decreased faster during each test than positions 1 and 2.

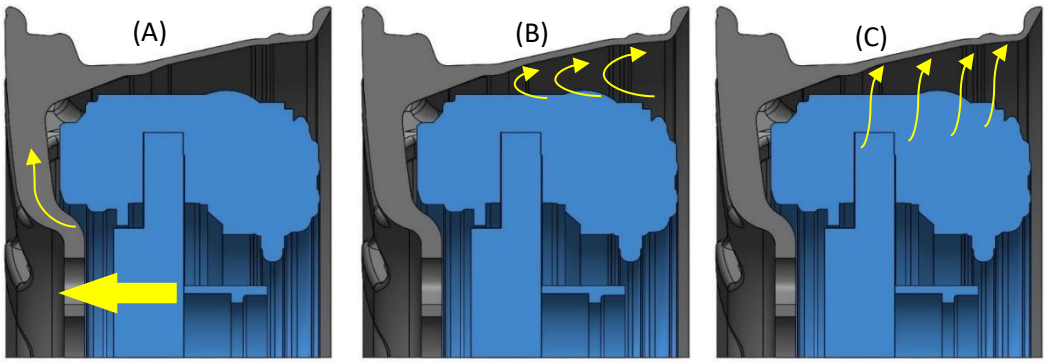


Figure 5-4 Heat transfer methods from a brake assembly to the wheel: (A) conduction, (B) convection and (C) radiation

Table 5-2 lists the temperatures that were recorded on the surface of the hub area, the centre of the spoke and on the rim. The temperatures decreased over time as the wheel cooled in the testing area. The temperatures measured on the hub area were consistently higher than the temperatures measured on the spoke and rim.

Table 5-2 Surface temperatures recorded during testing

Load setpoint (kg)	Hub temperature ≈ 50 °C			Hub temperature ≈ 70 °C			Hub temperature ≈ 90 °C		
	Hub (°C)	Spoke (°C)	Rim (°C)	Hub (°C)	Spoke (°C)	Rim (°C)	Hub (°C)	Spoke (°C)	Rim (°C)
40	50.2	49.1	35.7	69.0	63.5	53.2	86.6	75.2	48.6
80	49.5	48.2	36.8	68.6	62.6	52.0	86.5	73.0	46.6
120	49.7	47.4	37.7	70.0	61.3	51.0	86.3	71.3	45.5
160	49.0	46.6	36.4	69.6	61.8	49.7	85.4	70.1	45.2
200	49.2	46.0	35.3	69.3	61.1	48.8	84.4	67.7	45.8
160	48.6	44.9	35.7	68.4	60.0	47.7	82.4	65.8	46.3
120	49.0	44.8	35.2	69.0	59.3	46.6	84.2	66.3	47.1
80	49.0	43.7	33.3	68.8	58.3	45.7	83.4	65.1	49.1
40	48.6	43.3	32.5	68.5	56.7	45.0	83.9	63.9	48.0
0	48.4	42.8	31.9	68.0	56.6	44.5	82.3	62.1	47.3

Load setpoint (kg)	Hub temperature ≈ 100 °C			Hub temperature ≈ 140 °C		
	Hub (°C)	Spoke (°C)	Rim (°C)	Hub (°C)	Spoke (°C)	Rim (°C)
40	99.2	85.6	65.5	138.7	114.5	81.1
80	99.3	82.3	64.1	139.6	113.2	78.7
120	99.1	81.7	62.6	138.5	109.4	76.9
160	98.2	81.4	61.3	136.2	107.4	75.0
200	99.1	79.3	60.1	136.3	103.8	73.5
160	98.5	78.4	58.4	137.2	104.1	71.4
120	97.5	76.2	56.5	134.8	100.9	68.5
80	97.0	75.0	55.8	135.5	99.6	67.0
40	97.0	74.7	54.7	135.7	97.6	65.5
0	96.9	73.9	53.8	132.7	96.0	64.1

5.4.2. Bending stiffness versus load

Table 5-3 shows the recorded displacement of the load arm during testing. An increase in the deflection at the same load corresponds to a decrease in the bending stiffness of the wheel. There is an increase in the measured deflection at 200 kg with increasing temperature. The measured deflection at 0 kg load did not return to zero in any of the tests. The non-zero value of deflection indicates a small amount of sliding of the wheel. The same phenomenon was observed during the bending stiffness test to validate the composite FE model. The tests at temperatures of 50°C, 70°C and 140°C exhibited more sliding than the other tests. The variation in the amount of sliding was attributed to the tightening of the clamps while the wheel was at elevated temperatures. It proved challenging to sufficiently tighten the clamps on the wheel while simultaneously avoiding injury.

Table 5-3 Load arm displacement (mm)

Load (kg)	Ambient	50 °C	70 °C	90 °C	100 °C	140 °C	Ambient
40	0.74	0.74	0.75	0.82	0.84	0.95	0.86
80	1.51	1.62	1.60	1.67	1.72	1.88	1.76
120	2.30	2.45	2.47	2.51	2.59	2.82	2.63
160	3.09	3.28	3.35	3.38	3.47	3.80	3.50
200	3.89	4.17	4.26	4.21	4.34	4.73	4.35
160	3.20	3.44	3.42	3.42	3.54	3.73	3.55
120	2.44	2.67	2.72	2.62	2.73	3.04	2.74
80	1.68	1.90	1.91	1.82	1.87	2.15	1.89
40	0.85	1.10	1.09	0.95	0.99	1.23	0.99
0	0.08	0.23	0.21	0.09	0.08	0.25	0.05

The effect of sliding of the wheel on the surface of the test apparatus can be seen in Table 5-4. The bending stiffness of the wheel is shown in terms of the first calculated value at ambient temperature. In each test there is an apparent reduction in stiffness with increasing load. The calculated stiffness of the wheel decreased linearly while applying the load (see Figure 5-5) until the maximum load was reached. The decrease is less than a few percent. The calculated stiffness of the wheel decreased even further and at an increased gradient when unloading. This observation was found to be related to the sliding of the wheel. It took an elevated load to overcome the static friction of the wheel on the surface of the rig. The reduced kinetic friction, however, in combination with an elevated load, led to a higher cumulative value of displacement. The bending stiffness of the wheel was determined by averaging the calculated value for the load setpoints up to 200 kg i.e. by averaging the loading values.

Table 5-4 Bending stiffness of the wheel during experimentation in terms of the maximum calculated value (% of maximum)

Load (kg)	Ambient	50°C	70°C	90°C	100°C	140°C	Ambient
40	100.00	100.00	98.67	90.24	88.02	77.89	85.80
80	98.01	91.36	92.50	88.62	85.98	78.72	84.09
120	96.52	90.61	89.88	88.45	85.64	78.72	84.41
160	95.79	90.25	88.36	87.58	85.23	77.90	84.69
200	95.12	88.73	86.86	87.89	85.19	78.23	85.16
160	91.92	86.05	83.85	86.55	83.55	77.37	82.46
120	90.23	83.15	81.62	83.32	81.25	73.03	80.49
80	88.10	77.90	77.49	81.32	79.08	68.84	77.33
40	82.71	67.27	67.89	77.89	74.69	60.16	73.06

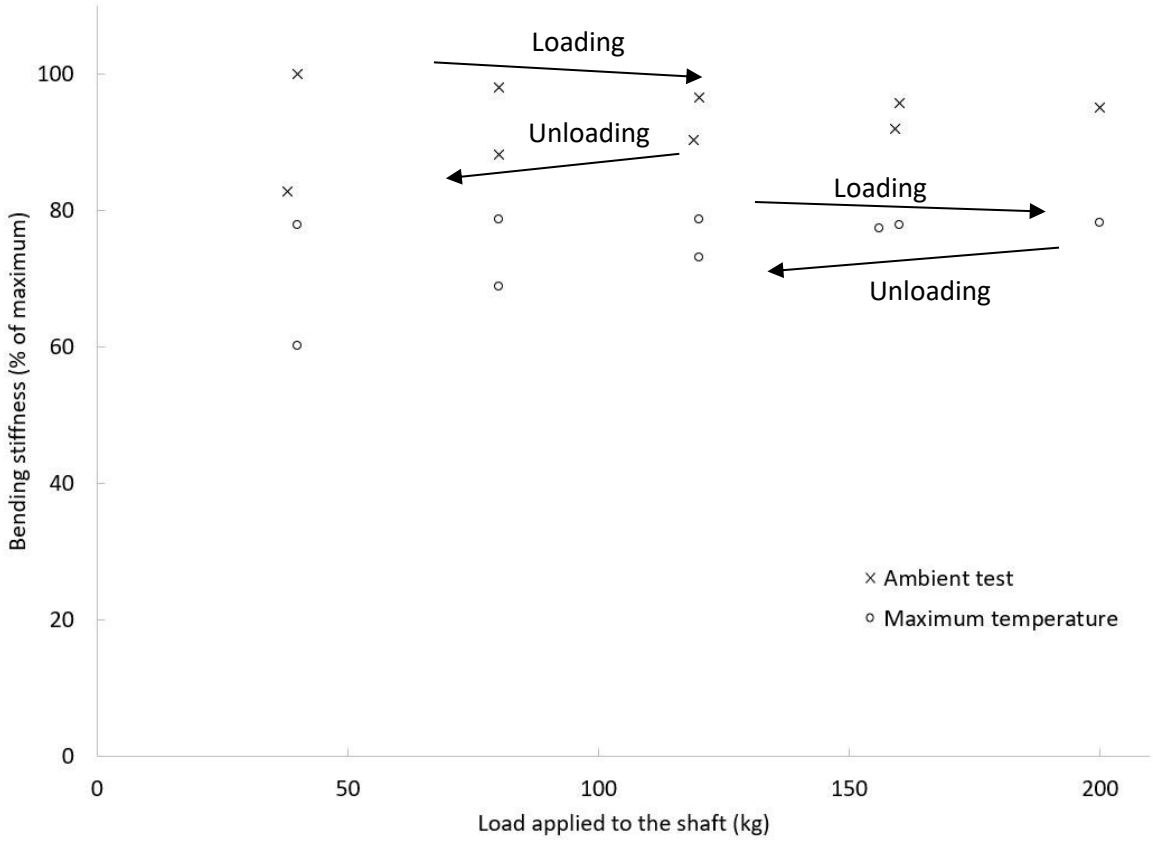


Figure 5-5 Bending stiffness of the wheel at ambient temperature and 140°C

5.4.3. Bending stiffness versus temperature

Figure 5-6 shows the calculated average bending stiffness of the wheel versus hub surface temperatures. The uncertainty bars indicate standard deviation. The bending stiffness test was repeated on the wheel at ambient temperatures after the assembly had cooled.

The bending stiffness decreases linearly with increasing temperature. An 18 % reduction in stiffness occurs at the maximum surface temperature of 140 °C. A 13 % reduction in stiffness was calculated when the wheel was retested at ambient temperatures. This would indicate that the wheel suffered permanent damage during the thermal experiment.

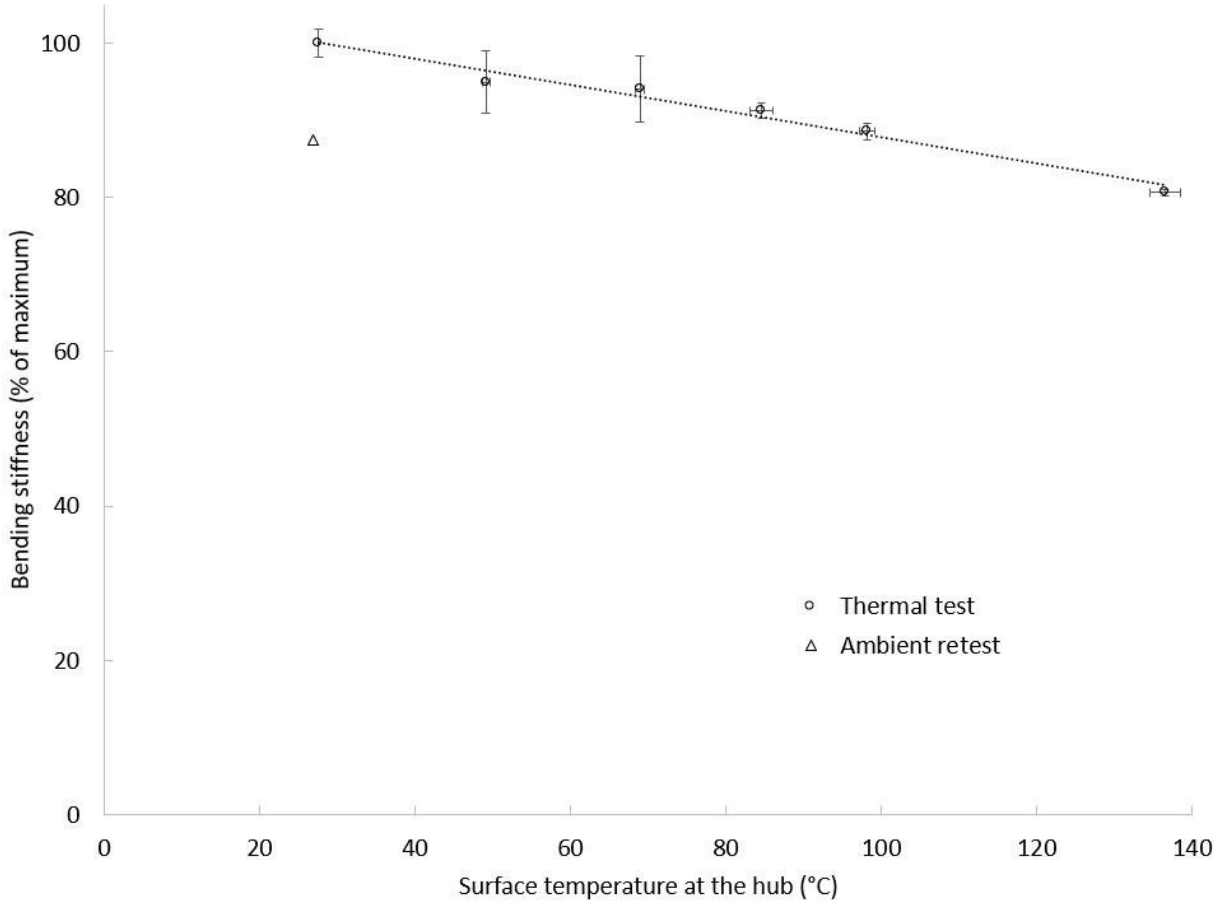


Figure 5-6 Average bending stiffness of the experimental prototype with increasing temperature

It is not known whether the temperatures measured on the wheel are representative on a road-going vehicle. The duration of the experiment (the time the wheel was at elevated temperatures) also influenced the mechanical properties of the CFRP. The cumulative time that this wheel was at elevated temperatures was thought to be substantially higher than that of a wheel on a road going vehicle. The real-world effect of temperature on the mechanical properties of a wheel cannot by fully quantified until such time that the temperature distribution across a wheel caused by a brake assembly is fully understood and characterised.

Further temperature testing is required to fully understand the effect of temperature on the mechanical properties of a CFRP wheel. The experimental data would indicate that the wheel

suffered a permanent reduction in stiffness due to the elevated temperatures experienced. The linear reduction in stiffness with increasing temperature that was determined is nevertheless useful to note. Despite the apparent damage that the wheel sustained, real world use of the wheels has not resulted in a reduction in mechanical properties after 18 months of use[6].

5.5. Summary

This chapter described an experiment to investigate the effect of temperature on the bending stiffness of a CFRP wheel. A bending stiffness test was conducted on a second CFRP wheel manufactured with an identical laminate to the previously tested wheel. The bending stiffness test was conducted on the specimen while the specimen and load arm were heated. The target temperatures were 50 °C, 70 °C, 90 °C, 100 °C and 140 °C. The surface temperatures of the wheel were recorded in the hub area, on the centre of a spoke and on the rim of the wheel.

The deflection of the load arm was recorded using a dial gauge. The position of the dial gauge was measured and controlled. The bending stiffness of the wheel was estimated for each load point using the measured deflection on the dial gauge. The stiffness of the wheel was observed to decrease as the load was increased and subsequently decreased. In each test, a non-zero value of deflection was recorded at zero load after unloading. This was attributed to sliding of the specimen on the plate surface. The non-zero deflection at zero load was found to be proportional to the apparent loss in stiffness throughout each test. The bending stiffness values were averaged from increasing load test points. The bending stiffness of the wheel was observed to decrease linearly with average surface temperature. The data obtained from this experiment indicated a decrease in bending stiffness of 18 %. A permanent 13 % reduction in bending stiffness was calculated when the wheel was retested at ambient temperatures. It is not known if the temperatures measured on the surface of the wheel in this experiment are representative of a wheel on a production car. Further temperature testing is required to fully understand the effect of temperature on the mechanical properties of a CFRP wheel.

[6] The wheels are regularly used by Donkervoort on the racetrack, where maximum temperatures are expected on the brakes.

The work in this chapter was conducted to fulfil the requirement of the third stated objective as set out in Section 1.3. It was determined that the CFRP wheel had a linear reduction in stiffness with increasing temperature. Despite the apparent permanent damage, 18 months of real-world use has not resulted in an apparent reduction in mechanical properties of the wheel.

6. CONCLUSIONS AND RECOMMENDATIONS

The aim of this study was to develop of a method to design a CFRP wheel. The development process of the wheels intended for a lightweight production sports car was used to define this method. This aim was distilled into the first objective which was to develop a process to design a CFRP wheel to withstand dynamic cornering fatigue loads as specified by certified testing standards. The work that was conducted to determine the appropriate method is as follows. An initial CAD geometry was created using Solidworks. The initial geometry was designed to customer specific standards. An isotropic simulation of a static DCF test was conducted on the geometry to eliminate stress concentrations. A refined geometry was used to design a mould and manufacture a prototype wheel. The prototype wheel was tested in a DCF rig to the required loads.[7] The wheel entered production after the required tests had been passed and was delivered to the customer for performance evaluation. The mass of the wheel was first reduced by conducting FE simulations on the aluminium hubs. The mass of the hubs was reduced by 18 %. The improved hubs were tested on a further prototype wheel on the DCF rig to certified loads.

The improved wheel used to define this methodology is now available as a performance upgrade as OE in the European market. Figure 6-1 shows the CFRP wheel developed in this study equipped on the Donkervoort D8 GTO-40. The Donkervoort D8 GTO-40 is stated to have an acceleration (0-100 km/h) of 2.7 seconds from a standstill [19]. The improved acceleration of this vehicle when compared to previous models has been attributed to reduced vehicle weight.



Figure 6-1 Donkervoort D8 GTO-40 with CFRP wheels developed in this study [19]

[7] Additional testing was also performed on the wheel for certification

This tangible improvement in performance served as the motivation for the second objective of this study. The second objective of this study was to reduce the mass of the developed passenger vehicle wheel. The work conducted to reduce the mass of the wheel also forms part of the work to define the development process, as required by the first objective. A bending stiffness test was performed on an experimental wheel. The bending stiffness test was conducted as part of the characterisation process of the wheel. The wheel was instrumented with strain gauges that recorded data to be compared to a composite FE simulation at a later stage. Tensile tests were performed on the material types used in the prototype wheel. The observation of the difference in thickness of the tensile specimens under the same manufacturing conditions warranted an investigation of the fibre volume fraction of the specimens and the wheel. The fibre volume fraction of a section of a spoke was found to be meaningfully higher than that of the test specimens. In addition, a CT scan of the wheel revealed that the prototype wheel had a thinner spoke than analytical calculations suggested. This further suggested that the stiffness of the materials in the wheel was higher than those in the material database.

A composite FE model was created using ANSYS ACP. The laminate of the prototype wheel was recreated ply by ply in the computer software. A bending stiffness test was recreated in the FE simulation. The strains were output by the software at the locations that corresponded to the placement of the strain gauges. The data from the strain gauges in the bending stiffness test were used to validate the composite FE model. The simulated strains showed acceptable agreement with the measured values. In addition to the measured and simulated strains, the deflection of the edge of the rim was recorded in the experiment. The simulated deflection was output by the computer simulation and showed acceptable agreement to measured values.

The validated composite FE model was used to analyse the stresses of the individual plies in the wheel. The stresses were compared to the allowable values provided by the material supplier. An assumption of the reduction in allowable stress due to fatigue strength was made based on reductions seen in literature. The assumed fatigue stress limit will serve as a variable in the method until such time as the exact value is determined. The stress analysis of the wheel showed that the further weight reduction of the wheel was not possible without compromising the mechanical properties of the wheel. It was thought that future wheel

designs would benefit greatly from the use of larger spoke sections, where the significant advantage of UD materials in terms of stiffness and stress limit could be better utilised.

The third objective of this study was to understand the mechanical strength degradation of carbon fibre reinforced plastic wheels with respect to temperature. A bending stiffness test was conducted on a wheel with surface temperatures ranging from ambient (25 ^{o}C) to 140 ^{o}C. The data obtained from this experiment indicated an 18 % reduction in stiffness at the 140 ^{o}C surface temperature. A 13 % reduction in stiffness was calculated when the wheel was retested at ambient temperatures. The use of a CFRP wheel remains feasible despite the calculated reduction in stiffness. The real-world effect of temperature on the mechanical properties of a wheel cannot by fully quantified until such time that the temperature distribution across a wheel caused by a brake assembly is understood.

More thermal testing is needed to understand the effect of temperature on CFRP wheels. The time effect of elevated temperatures should also be investigated. The thermal testing conducted for this study involved maintaining elevated temperatures of the wheel for a duration in excess of eight hours. It is therefore possible that the calculated reduction in stiffness is not representative of thermal effects experienced under real world conditions. In addition, the wheel used to develop this methodology has been used for 18 months under racing conditions, without any apparent reduction in mechanical properties.

In summary:

- A wheel was designed and developed for a production sports car. The wheel is available as a performance upgrade as OE.
- The development process of this wheel was used to shape the design process of future wheels.
- Finite element models developed during this study reduced the probability of laminate failure in the prototyping phase by eliminating stress concentrations on the surface of the geometry.
- Finite element models developed during this study resulted in a 20 % reduction in mass of the wheel hubs. This method was used to design hubs for other vehicles.
- This study shows that an aluminium wheel for a high-performance roadster can be redesigned using CFRP to be 21 % lighter. The wheel used to determine this methodology had a mass of 6.4 kg. The standard wheel for the intended vehicle had

a mass of 8.1 kg. While this reduction in mass is seemingly lower than expected, it is important to note that the wheel was developed for the gross vehicle mass in combination with semi slick tyres.

- The vehicle manufacturer claimed a reduction in 0-100 km/h time of 0.1 seconds (3.5 %) [19]. This was mainly attributed to weight reduction.
- The wheel that was improved by this study is now being produced at a rate in excess of 1000 sets per year.
- The method outlined in this document for development of a composite FE wheel was used for the development of three additional wheel designs.
- This method will be implemented in the development process of wheels for a new aftermarket design, as well as OEM wheels for European and American supercars manufacturers.
- A bending stiffness test was conducted on a prototype wheel with elevated surface temperatures. A linear relationship was determined between the reduction in stiffness and the surface temperature.
- A reduction in stiffness of 18 % at 140 ^{o}C surface temperature was calculated.
- A permanent reduction in stiffness of 13% after the wheel was measured when the wheel was retested at ambient temperature.
- Temperature testing was conducted over an eight-hour period. The effect of temperature over time must be considered. The temperature experienced by the wheel during this period is not necessarily representative of real-world conditions.
- The temperature distribution on a wheel/brake assembly is not well known and requires further investigation.

Based on these conclusions, the following recommendations are made:

- Thorough material testing should be conducted on the fabrics available for use before the composite model developed in this study can be implemented for future projects. Material testing should also be considered on alternate material types that may be used in the wheel. The accuracy of the mechanical response is dependent on the accuracy of the material definition.
- Fatigue failure predictions require the determination of the S-N curve of the material type.
- The method used to generate the composite FE laminate did not allow for multiple material iterations to be tested. Manual input was required to investigate the change

in mechanical response of alternate laminate configurations. This limited the number of configurations that could be investigated. A method of parameterising the laminate should be investigated. This could allow for the use of evolutionary algorithms.

- A further study should be conducted to determine the temperature distribution of CFRP wheels for performance cars under real world conditions. This study could provide CFRP wheel manufacturers with a better understanding of how heat is transferred into the wheels.
- A study should be conducted to determine the effect of heat over time on the mechanical properties of a CFRP wheel.
- A wheel intended for racing use only should be developed with a lower static load rating to fully utilise the weight saving potential of the carbon fabrics.

7. REFERENCES

[1] Fitz F, Gadd C. Development of a Light Weight Passenger Car Wheel Using Conventional Steels and Fabrication Techniques. SAE Tech Pap Ser 1999;01. https://doi.org/10.4271/1999-01-0782.

[2] Gonzalez Palencia JC, Furubayashi T, Nakata T. Energy use and CO2 emissions reduction potential in passenger car fleet using zero emission vehicles and lightweight materials. Energy 2012;48:548–65. https://doi.org/10.1016/j.energy.2012.09.041.

[3] Mohapatra S, Das S. Introduction of High Strength Steel for Commercial Vehicles - Light Weighting of Vehicles 2015. https://doi.org/10.4271/2014-28-0002.Copyright.

[4] Olatunbosun O a., Gauchia a., Boada MJL, Diaz V. Dynamic Performance Analysis of a Light Van Body-In-White Structure. Proc Inst Mech Eng Part D J Automob Eng 2011;225:167–77. https://doi.org/10.1243/09544070JAUTO1556.

[5] Easton M, Beer A, Barnett M, Davies C, Dunlop G, Durandet Y, et al. Magnesium alloy applications in automotive structures. Jom 2008;60:57–62. https://doi.org/10.1007/s11837-008-0150-8.

[6] Joost WJ, Krajewski PE. Towards magnesium alloys for high-volume automotive applications. Scr Mater 2017;128:107–12. https://doi.org/10.1016/j.scriptamat.2016.07.035.

[7] Wang X, Zhang X. Simulation of dynamic cornering fatigue test of a steel passenger car wheel. Int J Fatigue 2010;32:434–42. https://doi.org/10.1016/j.ijfatigue.2009.09.006.

[8] Zheng ZG, Sun T, Xu XY, Pan SQ, Yuan S. Numerical simulation of steel wheel dynamic cornering fatigue test. Eng Fail Anal 2014;39:124–34. https://doi.org/10.1016/j.engfailanal.2014.01.021.

[9] Kocabicak U, Firat M. Numerical analysis of wheel cornering fatigue tests. Eng Fail Anal 2001;8:339–54. https://doi.org/10.1016/S1350-6307(00)00031-5.

[10] Muthuraj R, Badrinarayanan R, Sundararajan T. Improvement In The Wheel Design Using Realistic Loading Conditions – FEA and Experimental Stress Comparison. SAE Int 2011;28. https://doi.org/10.4271/2011-28-0106.

[11] Hsu Y-L, Hsu M-S. Weight reduction of aluminum disc wheels under fatigue constraints using a sequential neural network approximation method. Comput Ind 2001;46:167–79. https://doi.org/10.1016/S0166-3615(01)00125-7.

[12] Raju PR, Satyanarayana B, Ramji K, Babu KS. Evaluation of fatigue life of aluminum alloy wheels under radial loads. Eng Fail Anal 2007;14:791–800. https://doi.org/10.1016/j.engfailanal.2006.11.028.

[13] Stearns J, Srivatsan TS, Prakash A, Lam PC. Modeling the mechanical response of an aluminum alloy automotive rim. Mater Sci Eng A 2004;366:262–8. https://doi.org/10.1016/j.msea.2003.08.017.

[14] Firat M, Kozan R, Ozsoy M, Mete OH. Numerical modeling and simulation of wheel radial fatigue tests. Eng Fail Anal 2009;16:1533–41. https://doi.org/10.1016/j.engfailanal.2008.10.005.

[15] Li P, Maijer DM, Lindley TC, Lee PD. A through process model of the impact of in-service loading, residual stress, and microstructure on the final fatigue life of an A356 automotive wheel. Mater Sci Eng A 2007;460–461:20–30. https://doi.org/10.1016/j.msea.2007.01.076.

[16] Giger M, Ermanni P. Development of CFRP racing motorcycle rims using a heuristic evolutionary algorithm approach. Struct Multidiscip Optim 2005;30:54–65. https://doi.org/10.1007/s00158-004-0471-3.

[17] Rondina F, Taddia S, Mazzocchetti L, Donati L, Minak G, Rosenberg P, et al. Development of full carbon wheels for sport cars with high-volume technology. Compos Struct 2018;192:368–78. https://doi.org/10.1016/j.compstruct.2018.02.083.

[18] Blackstone TEK. BST Carbon Fiber Car Wheels 2017. http://blackstonetek.com/bst-best-carbon-fiber-wheels-home/bst-carbon-fiber-car-wheels/.

[19] Donkervoort. Donkervoort D8 GTO-40 n.d. https://www.donkervoort.com/en/cars/donkervoort-d8-gto-40/.

[20] Hrovat D. Influence of unsprung weight on vehicle ride quality. J Sound Vib 1988;124:497–516. https://doi.org/10.1016/S0022-460X(88)81391-9.

[21] Ressa A. Development of a carbon fiber wheel rim. The Ohio State University, 2013.

[22] Walther H. Development of a Lightweight Laminated Composite Wheel for Formula Sae Race Vehicles. University of Kansas, 2016.

[23] Kinstler J. The Science and Methodology of SAE Wheel Fatigue Test Specifications. SAE Tech Pap Ser 2005;01. https://doi.org/10.4271/2005-01-1826.

[24] Baltruschat K, Dittmar S, Tallafuß T. Guidelines for the testing and inspection of plastic wheels for passenger cars and motorcycles 2018:769–83. https://doi.org/10.1007/978-3-658-22050-1_51.

[25] Carvalho CP De, Jacobus H, Voorwald C, Lopes CE. Automotive Wheels – An Approach for Structural Analysis and Fatigue Life Prediction. Sae Pap 2001-01-4053 2001:237–43. https://doi.org/10.4271/2001-01-4053.

[26] K MB, Vinothkumar S, Srinivasan S, Nesarikar A. Simulation and Test Correlation of

Wheel Impact Test. SAE Tech Pap Ser 2011;28. https://doi.org/10.4271/2011-28-0129.

[27] Adamowicz A, Grzes P. Analysis of disc brake temperature distribution during single braking under non-axisymmetric load. Appl Therm Eng 2011;31:1003–12. https://doi.org/10.1016/j.applthermaleng.2010.12.016.

[28] Kim MR, Ahn BJ, Lee JM, Jung YK. Numerical Investigation of Thermal Behavior in Brake Assembly During the ALPINE Braking Mode 2007;2007. https://doi.org/10.4271/2007-01-1021.

[29] Nisonger RL, Yen C, Antanaitis D. High Temperature Brake Cooling - Characterization for Brake System Modeling in Race Track and High Energy Driving Conditions. SAE Int J Passeng Cars - Mech Syst 2011;4:2011-01–0566. https://doi.org/10.4271/2011-01-0566.

[30] Feih S, Boiocchi E, Kandare E. Strength Degradation of Glass and Carbon Fibres at High Temperature. 19th Int Conf Compos Mater 2009:2–11.

[31] Hancox NL. Thermal effects on polymer matrix composites : Part 2 . Thermal degradation. Mater Des 1998;19:93–7. https://doi.org/10.1016/S0261-3069(98)00019-3.

[32] Chung DD. Thermal analysis of carbon fiber polymer-matrix composites by electrical resistance measurement. Thermochim Acta 2000;364:121–32. https://doi.org/10.1016/S0040-6031(00)00631-6.

[33] Wolfrum J, Eibl S, Lietch L. Rapid evaluation of long-term thermal degradation of carbon fibre epoxy composites. Compos Sci Technol 2009;69:523–30. https://doi.org/10.1016/j.compscitech.2008.11.018.

[34] Askeland DR. Essentials of Materials Science and Second Edition , SI. n.d.

[35] Wang E, Nelson T, Rauch R. Back to Elements - Tetrahedra vs . Hexahedra. CAD-FEM GmbH, Munich, Ger 2004:16.

[36] Properties and Selection: Nonferrous Alloys and Special-Purpose Materials. ASM Handb 1990;2.

[37] Muraca RF, Whittick JS. Aluminum Alloy 7075. Western Applied Research & Development, Inc.; 1972.

[38] MakeItFrom.com. 6082-T6 Aluminum n.d. https://www.makeitfrom.com/material-properties/6082-T6-Aluminum (accessed November 9, 2019).

[39] ASTM International. Standard Test Method for Tensile Properties of Polymer Matrix Composite Materials 2017. https://doi.org/10.1520/D3039_D3039M-17.

[40] Kawai M, Koizumi M. Nonlinear constant fatigue life diagrams for carbon/epoxy

laminates at room temperature. Compos Part A Appl Sci Manuf 2007;38:2342–53. https://doi.org/10.1016/j.compositesa.2007.01.016.

[41] Stein WA. A summary of Classical Lamination Theory 2010. https://wstein.org/edu/2010/480b/projects/05-lamination_theory/A summary of Classical Lamination Theory.pdf.

APPENDIX A: FE VALIDATION USING FIRST PRINCIPLES

To validate that the FE software was being used correctly, a first principles calculation was performed. The FE outputs of isotropic and composite models of a simple plate or beam were compared to theoretical calculations.

Geometry and Free Body Diagram

A simple rectangular plate was created using Solidworks and imported into ANSYS. The dimensions of the rectangular plate were 165 x 19 x 3.2 mm (L x w x t). Figure A-1 shows the loading applied to the plate. The plate was modelled as a cantilever beam with an applied axial force (F_a) and a lateral force (F_b). The axial displacement (ΔL) and the lateral beam deflection (v_b) were calculated analytically and compared with the output of the FE model.

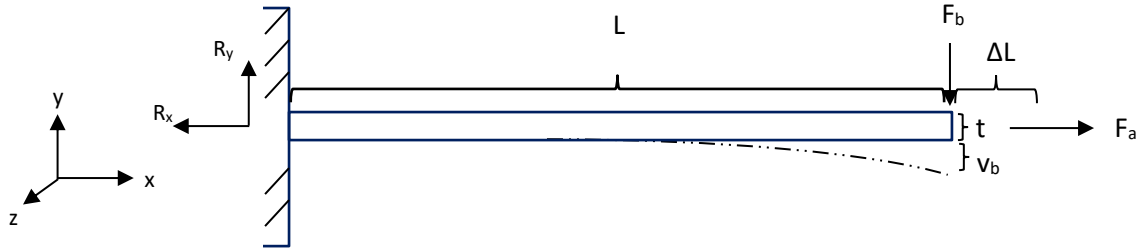


Figure A-0-1 Free body diagram of the plate used for validation

Isotropic Validation

For the isotropic validation, structural steel (E=200 GPa) and aluminium alloy (E=71 GPa) were used as materials in the static structural model. The axial displacement per unit width was determined by:

$$\frac{\boldsymbol{\Delta L}}{\boldsymbol{w}} = \frac{\boldsymbol{F_a * L}}{\boldsymbol{E * t}} \tag{13}$$

The beam deflection was determined by:

$$\boldsymbol{v_b} = \frac{\boldsymbol{F_b * L^3}}{\boldsymbol{3E * I}} \tag{14}$$

Table A-1 compares the analytically calculated axial displacements (ΔL) to the FEA results (FEA ΔL). The aluminium alloy and structural steel had a 99.7 % and 99.8 % accuracy respectively. Table A-2 compares the analytically calculated beam deflections (*v*) to the FEA results (FEA *v*). The aluminium alloy and structural steel had a 98.8 % and 99.0 % accuracy respectively.

Table A-0-1 Response of the plate under axial loading

F_a (N)	Aluminium alloy		Structural steel	
	ΔL (mm)	FEA ΔL (mm)	ΔL (mm)	FEA ΔL (mm)
100	3.822E-03	3.814E-03	1.357E-03	1.355E-03

Table A-0-2 Response of the plate under the lateral load

Force (N)	Aluminium alloy		Structural steel	
	v (mm)	FEA v (mm)	v (mm)	FEA v (mm)
100	40.649	40.179	14.430	14.293

Classic Laminate Theory Validation

For the validation of the composite FE software, a surface body was created in Solidworks. The dimensions of the rectangular surface body were 165 x 19 x 0 mm (L x w x t). Classic Laminate Theory (CLT) was used to determine the analytical response of the plate under an axial load. A rectangular carbon fibre laminate was created using *Epoxy Carbon UD (230GPa) Prepreg* and *Epoxy Carbon Woven (230GPa) Prepreg* from the FE material database. The first test laminate was made up of five layers of UD prepreg at a 0^o fibre orientation. The second laminate was made up of two layers of UD prepreg at a 0^o fibre orientation between two woven prepreg layers at a 0^o fibre orientation. Table A-3 shows the material properties of the fabrics used.

Table A-0-3 Material properties obtained from the ANSYS material database

Property	UD	Woven
E_1	121.00 GPa	61.34 GPa
E_2	8.60 GPa	61.34 GPa
G_{12}	4.70 GPa	19.50 GPa
v_{12}	0.27	0.04

The first test laminate was modelled in the composite FE software and compared to the analytical value obtained using Equation 13. This was possible, as the laminate was made of a single material with all fibres oriented at 0^o with respect to axis 1. Analytical calculations were performed using CLT [41] to determine the response of laminate 2.

The first step in a CLT calculation is the determination of the reduced stiffness matrix Q_{ij} of each material used in the laminate. The reduced stiffness matrix is:

$$\boldsymbol{Q_{ij}} = \begin{bmatrix} \boldsymbol{Q_{11}} & \boldsymbol{Q_{12}} & \boldsymbol{0} \\ \boldsymbol{Q_{12}} & \boldsymbol{Q_{22}} & \boldsymbol{0} \\ \boldsymbol{0} & \boldsymbol{0} & \boldsymbol{Q_{66}} \end{bmatrix} \tag{15}$$

where,

$$\boldsymbol{Q_{11}} = \frac{\boldsymbol{{E_1}^2}}{(\boldsymbol{E_1 - \nu_{12} * E_2})} \tag{16}$$

$$\boldsymbol{Q_{12}} = \frac{\boldsymbol{\nu_{12} * E_1 * E_2}}{(\boldsymbol{E_1 - {\nu_{12}}^2 * E_2})} \tag{17}$$

$$\boldsymbol{Q_{22}} = \frac{\boldsymbol{E_1 * E_2}}{(\boldsymbol{E_1 - {\nu_{12}}^2 * E_2})} \tag{18}$$

and,

$$\boldsymbol{Q_{66}} = \boldsymbol{G_{12}} \tag{19}$$

Next, the [ABD] matrix is assembled:

$$[\boldsymbol{ABD}] = \begin{bmatrix} \boldsymbol{A} & \boldsymbol{B} \\ \boldsymbol{B} & \boldsymbol{D} \end{bmatrix}$$

The components of the matrix are calculated by:

$$\boldsymbol{A_{ij}} = \sum_{\boldsymbol{k=1}}^{\boldsymbol{n}} \{\boldsymbol{Q_{ij}}\}_{\boldsymbol{n}} (\boldsymbol{z_k - z_{k-1}}) \tag{20}$$

$$\boldsymbol{B_{ij}} = \frac{\boldsymbol{1}}{\boldsymbol{2}} \sum_{\boldsymbol{k=1}}^{\boldsymbol{n}} \{\boldsymbol{Q_{ij}}\}_{\boldsymbol{n}} (\boldsymbol{{z_k}^2 - {z_{k-1}}^2}) \tag{21}$$

$$\boldsymbol{D_{ij}} = \frac{\boldsymbol{1}}{\boldsymbol{3}} \sum_{\boldsymbol{k=1}}^{\boldsymbol{n}} \{\boldsymbol{Q_{ij}}\}_{\boldsymbol{n}} (\boldsymbol{{z_k}^3 - {z_{k-1}}^3}) \tag{22}$$

where z represents the position of the ply in the overall laminate. The [A] matrix is the extension stiffness matrix, the [B] matrix is the coupling stiffness matrix (strain-curvature) and the [D] matrix is the bending stiffness matrix.

The ABD matrix is used to relate the midplane strains and curvatures to the applied loads in the laminate. The loads are related by:

$$\begin{bmatrix} N_{xx} \\ N_{yy} \\ N_{xy} \\ M_{xx} \\ M_{yy} \\ M_{xy} \end{bmatrix} = \begin{bmatrix} A_{11} & A_{12} & A_{16} & B_{11} & B_{12} & B_{16} \\ A_{12} & A_{22} & A_{26} & B_{12} & B_{22} & B_{26} \\ A_{16} & A_{26} & A_{66} & B_{16} & B_{26} & B_{66} \\ B_{11} & B_{12} & B_{16} & D_{11} & D_{12} & D_{16} \\ B_{12} & B_{22} & B_{26} & D_{12} & D_{22} & D_{26} \\ B_{16} & B_{26} & B_{66} & D_{16} & D_{26} & D_{66} \end{bmatrix} * \begin{bmatrix} \varepsilon_{xx} \\ \varepsilon_{yy} \\ \varepsilon_{xy} \\ \kappa_{xx} \\ \kappa_{yy} \\ \kappa_{xy} \end{bmatrix} \quad (23)$$

As there were no bending loads modelled, and the B matrix is zero for a symmetrical laminate, this reduces to:

$$\begin{bmatrix} N_{xx} \\ N_{yy} \\ N_{xy} \end{bmatrix} = \begin{bmatrix} A_{11} & A_{12} & A_{16} \\ A_{12} & A_{22} & A_{26} \\ A_{16} & A_{26} & A_{66} \end{bmatrix} * \begin{bmatrix} \varepsilon_{xx} \\ \varepsilon_{yy} \\ \varepsilon_{xy} \end{bmatrix} \quad (24)$$

To verify the calculations within the composite FE software, a set of loads was applied to the modelled plate. The deformation in the linear static structural environment was used to determine the average strain of the body along the x-axis. The effect of the strain on the y-axis due to the Poisson's Ratio was determined to have a negligible effect. The strain values were used to determine the theoretical force required to achieve the strains using the [ABD] matrix. The analytically determined theoretical force was compared to the applied load. The resultant value of N_{xx} represents an applied force per unit width. Table A-4 shows a comparison of forces from the FE model. The first column lists the forces that were applied to the FE model. The second and third column list the required forces to achieve the same deformation, based on CLT, using a surface and solid geometry respectively. The solid model showed the best agreement. The surface model was accurate to within 5 %.

Table A-0-4 Comparison of forces required for solid and surface models

FE applied Force (N)	Analytical Force (N) (surface geometry)	Analytical Force (N) (solid geometry)
100	104.16	100.63